A Radio View of the Bullet Cluster from 100 MHz to 9 GHz

MSc Thesis

Raghav Srinivasan

Supervisor:
A/Prof. Melanie Johnston-Hollitt

A thesis submitted to the Victoria University of Wellington in fulfillment of the requirements for the degree of Master of Science in Physics. Victoria University of Wellington 2015

Acknowledgements

First and foremost, I thank my supervisor A/Prof. Melanie Johnston-Hollitt for her guidance, patience, flexibility, knowledge and encouragement throughout my thesis. I would have not completed this thesis without her support and motivation. I would like to thank my team members from the radio astronomy group at VUW for their support during my tenure. A special thanks to Dr Dehghan and Luke Pratley for providing valuable inputs and suggestions during the course of my work. Also, I would like to thank Tim Shimwell for providing his previously unpublished data at 1.1 GHz - 3.1 GHz on sources in the Bullet cluster. I thank the SKA organisation for funding our travel to the NZ-China SKA summer school. Finally, I would like to express my deepest gratitude to my wife Archana Anand and my parents for their support during my most challenging moments.

Statement of Originality

I certify that this work contains no material which has been accepted for the award of any other degree or diploma in any university or other tertiary institution and, to the best of my knowledge and belief, contains no material previously published or written by another person, except where due reference has been made in the text. All the spectral index plots and the fits in this thesis was provided by Dr. Dehghan. In addition, I certify that no part of this work will, in the future, be used in submission for any other degree or diploma in any university or other tertiary institution without the prior approval of the Victoria University of Wellington and where applicable, any partner institution responsible for the joint-award of this degree. I give consent to this copy of my thesis, when deposited in the University Library, being made available for loan and photocopying, subject to the provisions of the Copyright Act 1994. I also give permission for the digital version of my thesis to be made available on the web, via the University's digital research repository, the library catalogue and also through web search engines, unless permission has been granted by University to restrict access for a period of time.

I contributed to the following publication based on the work from this thesis:

- Timothy W. Shimwell, Maxim Markevitch, Shea Brown, Luigina Feretti, B. M. Gaensler, M. Johnston-Hollitt, Craig Lage, Raghav Srinivasan (2015). Another shock for the Bullet cluster, and the source of seed electrons for radio relics. *Monthly Notices of the Royal Astronomical Society*, arXiv:1502.01064. (Submitted)

Raghav Srinivasan

Date

Abstract

We investigate a sample of 10 massive galaxy clusters for diffuse synchrotron emission. The shortlisted clusters are drawn from a sample of clusters observed with the South Pole Telescope (SPT) shown to have high Sunyaev-Zeldovich (SZ) signals.They are analysed for diffuse emission from the results of the Australia Telescope Compact Array (ATCA) archival data reduction. The focus then is on the cluster with the most prominent diffuse emission - the Bullet cluster. We used the Murchison Widefield Array Commissioning Survey (MWACS) data in conjunction with the ATCA images to derive the spectral behaviour of the Bullet cluster from 0.118 GHz to 8.896 GHz. In particular, we study the spectral properties of the known radio halo and radio relic. We search for spectral bending of this diffuse emission as seen in other clusters like the Coma cluster, A2256, A521 and A3256.

We detect the radio relic at all frequencies in the cluster periphery. Polarised flux is detected for the relic at all frequencies except at 1.344 GHz and as expected the percentage polarisation increases with frequency. Our spectral index values of -1.08 $\pm$ 0.02 and -1.74 $\pm$ 0.22 for 2 regions of the radio relic agreed with the literature. We detect spectral flattening for a region in the radio relic at 4.532 GHz. This is a common spectral characteristic for a radio galaxy. This suggests that the source could be a recently dead radio galaxy. We discuss a scenario in which a dead radio galaxy supplying seed electrons for reacceleration and a merger process providing the required energy for the diffuse radio relic. We detect the radio halo at all frequencies and we derive a spectral index of -2.11$\pm$0.03 using our ATCA flux measurements. Our individual flux measurements at 1.344 and 2.1 GHz agree with the literature. However, we get a steeper ATCA spectral index value for the radio halo as compared to the existing value in the literature. We observe spectral flattening of the radio halo in the Bullet cluster at low frequencies between 0.180 GHz and 1.3 GHz. This is similar to the spectral property of the halo in clusters like the Coma cluster, A521 and A3256.

Contents

§1. Introduction

§1.1. Structure of the Universe and galaxy clusters

The organization of the Universe begins at the stellar level which is in turn organized into galaxies, which form galaxy groups and galaxy clusters. Galaxy groups are collections of a small number of galaxies, approximately 50 in number, whereas galaxy clusters are structures that consists of hundreds to thousands of galaxies, and are systems of gas and dust bound together by gravity forming the largest gravitationally bound structures in the Universe. Galaxy clusters also consist of hot X-ray emitting gas and massive amounts of dark matter (Kravtsov and Borgani, 2012). A great number of groups, clusters and individual galaxies form the largest structure in the Universe called a supercluster. These superclusters are distributed as sheets, walls and filaments in a web like structure thus forming the matter in the observable Universe (see Fig 1.1).

Most galaxy clusters contain massive elliptical 'Central Dominant' cD galaxies and member galaxies with similar ages, recessional velocities and metallicities (for example see inset in Fig 1.1). The cD galaxy model suggests that the large central ellipitical galaxies are formed by the accretion of smaller spiral galaxies thereby forming a 'Central Dominant' cD galaxy. Galaxy clusters have a diameter of 2 to 10 Mpc and they have total masses of 10^{14} to 10^{15} solar masses. They are classified as rich and poor clusters based on the number of galaxies in the cluster. Galaxy clusters were extensively catalogued through optical observations by Abell (1958). Notable galaxy clusters in the relatively nearby Universe include the Virgo Cluster, Fornax Cluster, Hercules Cluster, and the Coma Cluster.

§1.2. Emission mechanism in galaxy clusters

§1.2.1. Thermal emission

One of the key features of galaxy clusters is the intracluster medium (ICM). The ICM consists of heated plasma composed of mainly ionized hydrogen and helium

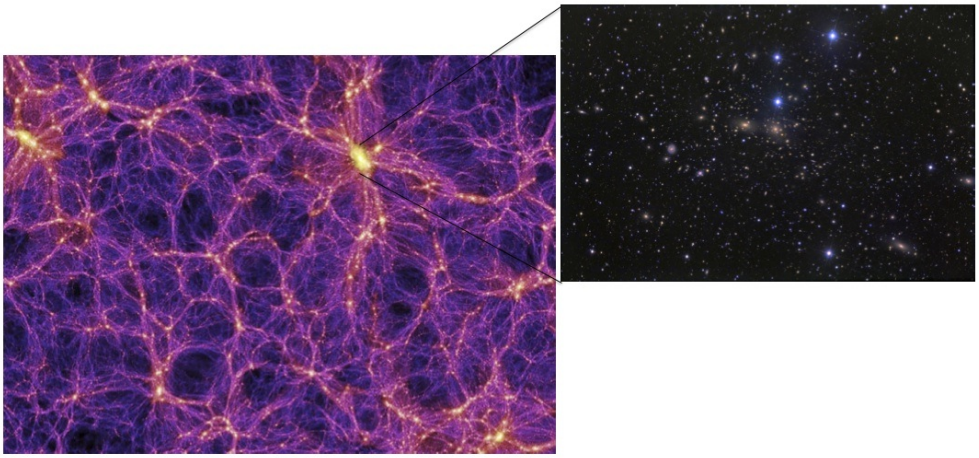

Figure 1.1: The cosmic web-like structure as simulated by Springel et al. (2005). The inset shows the Coma Cluster (Abell 1656) of galaxies, one of the densest clusters known which contains thousands of galaxies. Most of the galaxies located in the center of the cluster are elliptical galaxies. Please note that the coma cluster is shown as an example and the cluster is not actually located in the region of the cosmic web. Credit and Copyright: Dean Rowe. Downloaded from apod[1]. The inset highlights that the galaxy clusters similar to Coma can be observed in the brighter part of the cosmic web.

thereby containing most of the baryonic matter in the cluster. Electrons in the ICM interact with nuclei and emit in the X-ray region of the spectrum through a process called Bremsstrahlung, or 'braking radiation'. In the plasma of the ICM, free electrons constantly produce electromagnetic radiation in collisions with ions. The electromagnetic radiation is then produced by the deceleration of a charged particle as it loses its kinetic energy, which is converted into a photon. This deceleration happens when a charged particle is deflected by another charged particle. This radiation is in the energy range of X-ray and can be observed using X-ray telescopes. Figure 1.2 illustrates the mechanism of the emission through Bremsstrahlung

.

§1.2.2. Non-thermal emission in galaxy clusters

Non-thermal emission in galaxy clusters can be from individual radio or spiral galaxies or diffuse emission in the ICM that cannot be associated with any single galaxy. Non-thermal emission in galaxy clusters can be attributed to two main emission mechanisms - inverse Compton emission and synchrotron emission.

[1]URL - http://apod.nasa.gov/apod/ap100502.html

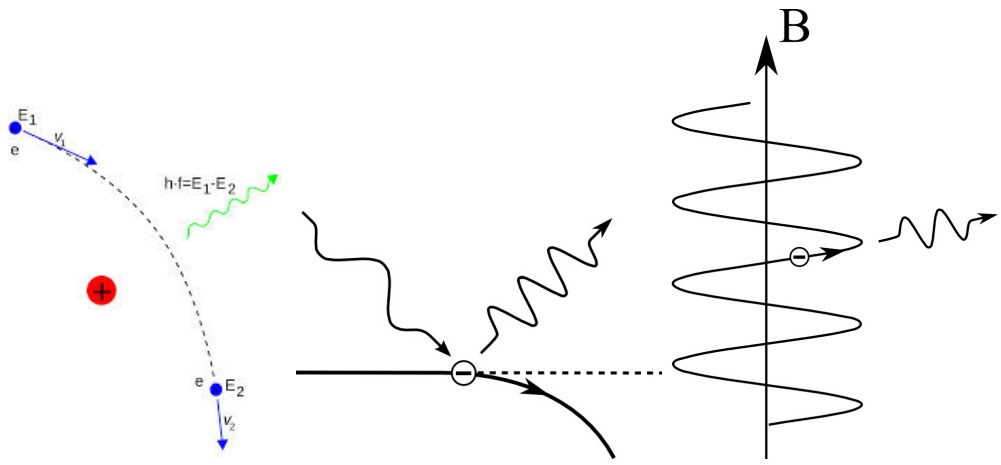

Figure 1.2: The image on the left depicts the change in direction of an electron when it interacts with an ion thereby resulting in thermal Bremsstrahlung emission. Source: Wikipedia. The image in the middle depicts the Inverse Comption mechanism where the photon gains energy when it is incident upon an electron and the electron loses energy in the process. The image on the right depicts synchrotron emission where an electron spirals around in a magnetic field thereby emitting photons in the process.

The mechanisms that produce a population of relativistic, non-thermal particles that give rise to synchrotron and inverse Compton radiation are collectively known as particle acceleration. Fermi acceleration is believed to be the mechanism behind non-thermal emission in which the charged particles undergo acceleration in a media of astrophysical shock waves (Rieger et al., 2007).

Inverse Compton emission

Inverse Compton (IC) scattering involves the scattering of low energy photons to high energies by ultrarelativistic electrons so that the photons gain and the electrons lose energy. The process is called inverse because the electrons lose energy rather than the photons, the opposite of the standard Compton effect (see Fig 1.2). The kinetic energy is transferred from the moving electron to the photon on collision satisfying the law of conservation of energy and momentum. When an external flux of soft photons is incident upon a hot plasma with a large scattering depth and a small absorption depth, the emergent spectrum would have a universal, quasi-power-law slope that is insensitive to plasma parameters (Rybicki and Lightman, 1986). Inverse Compton scattering also acts as a strong energy amplifier, converting low energy photons into X-rays. Non-thermal inverse Compton phenomena is observed in the ICM of galaxy clusters and can be studied in X-ray band through X-ray inverse

Compton emission due to the scattering between radio-emitting electrons and the Cosmic Microwave Background (CMB) photons.

Synchrotron emission

Synchrotron emission is a non-thermal emission generated when charged particles are accelerated through a magnetic field. When charged particles (electrons) spiral under the influence of a magnetic field at relativistic speeds, photons are emitted with frequencies dependent on the speed of the electron at that given point of time(see Fig 1.2). The radiation emitted is confined to a narrow cone pointing in the direction of the motion of the particle, through a process called beaming. It is also polarized in the plane perpendicular to the magnetic field, with the degree and orientation of the polarization providing information on the magnetic field responsible for the acceleration. As the electron spirals around the magnetic field, it emits radiation over a range of frequencies. The longer the electron travels around the magnetic field, the more energy it loses, the narrower the spiral it makes, and the longer the wavelength of the critical frequency. The emissivity is broadband and extends all the way from radiofrequencies to X-ray and γ-ray energies. Many real high-energy sources in astrophysics are also sources of strong radio emission due to synchrotron radiation. The spectral index of the diffuse source is represented by $S \propto \nu^{-\alpha}$ where S is the flux density of the radio source, ν is the frequency of observation and α is the spectral index. Synchrotron radiation follows a power law spectrum and is given by $\alpha = 1/2(p-1)$, where p is the particle distribution index. Since X-ray and radio emissions are produced by the same population of electrons undergoing inverse Compton and synchrotron energy losses, the ratio between X-ray and radio luminosities is proportional to the ratio of CMB and the magnetic field energy densities. This enables determination of the electron density and mean magnetic field of the ICM by comparing radio and hard X-ray emission (Feretti, 2008).

§1.3. Cluster magnetic fields

Measurements reveal the existence of magnetic fields everywhere in the cluster atmosphere (Feretti and Johnston-Hollitt, 2004). They play a significant role in cluster formation and evolution,and in determining the energy balance in the cluster gas through their effect on heat conduction. Magnetic fields in clusters are generally investigated in the radio band by studying the Rotation Measure (RM) and syn-

chrotron emission of individual radio galaxies, radio halos and relics. Other methods include X-ray studies of Inverse Compton emission, cold fronts and hydrodynamic simulations.

§1.3.1. Rotation Measure

Radio waves traversing the magnetized ICM show depolarization and rotation of the polarization position angle as a function of wavelength. This rotation as a function of frequency is the rotation measure. Rotation Measure (RM) values derived from multifrequency polarimetric observations combined with measurements of the thermal gas density (n_e) give an estimate of the magnetic field strength along the line of sight. The rotation measure is given by the equation below

$$RM = e^3/(8\pi^2\epsilon_0 m^2 c^3) \int_0^d n_e(s) B_{ll}(s) ds \tag{1.1}$$

where $n_e(s)$ is the density of electrons at each point s along the path, $B_{ll}(s)$ is the component of the interstellar magnetic field in the direction of propagation at each point s along the path, e is the charge of an electron, c is the speed of light in vacuum, m is the mass of an electron and ϵ_0 is the vacuum permittivity.

Magnetic field intensity measurements in galaxy clusters can be made by obtaining an average value of the RM from sources located at different impact parameters (distance from the cluster center) and by deriving maps of RM of the extended radio sources to evaluate the standard deviation of the RM distribution (Clarke et al., 2001) (Johnston-Hollitt and Ekers, 2004) (Johnston-Hollitt, 2003) (Vogt and Enßlin, 2003) (Pratley et al., 2013) (Pizzo et al., 2011) (Bonafede et al., 2014). One of the challenges of this approach at present is that the Faraday rotation study may only be undertaken statistically over a large number of clusters. Also since every measured RM is the vector addition of all contributing Faraday screens, it is not possible to disentangle the cluster RM from the internal RM of the source without a sufficient number of RM measures. There is also a possibility of overestimation of magnetic field strength due to the possible existence of local RM enhancements in the ICM. Currently RM measures are not available for a large number of clusters due to the limitations in sensitivity of the current instruments. This challenge will be overcome using the SKA which is currently under development and will have a factor of several thousand increase in the detectable RM values for extragalactic sources.

§1.3.2. Diffuse synchrotron emission

The presence of magnetic fields can be directly detected by the existence of diffuse cluster-wide radio emission like radio halos and relics(see next section for a discussion). Assuming a equipartition condition in radio sources, magnetic field values in the range of 0.1 - 2 μG can be derived in the radio emitting regions of clusters. These calculations generally assume equal energy in relativistic protons and electrons, magnetic fields entirely filling the radio volume and a low and high frequency cutoff of 10 MHz to 10 GHz respectively. Values derived using this method are consistent with recent detection of inverse Compton X-ray emission in clusters with halos and relics.

Some of the challenges of this approach are that the low surface brightness of cluster radio halos and their steep spectra make it difficult to image them accurately with the current resources. Also, at low resolution, true diffuse emission is sometimes difficult to distinguish from a blend of weak discrete radio sources.
Feretti and Johnston-Hollitt (2004) discuss cluster-wide magnetic fields and their detection methods using radio in more detail. Most of the information discussed above was sourced from Feretti and Johnston-Hollitt (2004).

§1.4. Radio emission in galaxy clusters

Diffuse radio emission that is found in the ICM of galaxy clusters is not associated with individual galaxies. Rather this emission is non-thermal synchrotron emission caused by the presence of magnetic fields and relativistic electrons within the ICM. Large et al. (1959) first detected the presence of diffuse and extended radio emission in the Coma cluster. Willson (1970) later confirmed the results using interferometric observations. Since then, diffuse non thermal emission has been detected in many other clusters. The steep spectral index (α>1) of these diffuse sources indicate the ageing of the emitting particles and the steepening is due to Compton-Synchrotron losses. As a result, the highest energy particles lose their energy more quickly and consequently the spectral index follows a steep power law fit. As a reference, the spectral index of the relic in cluster A521 is shown in Fig 1.3 (Giacintucci et al., 2008). The radio emission in the ICM can be classified into radio halos, relics and mini halos. The details of these emissions are discussed in the following sub-sections.

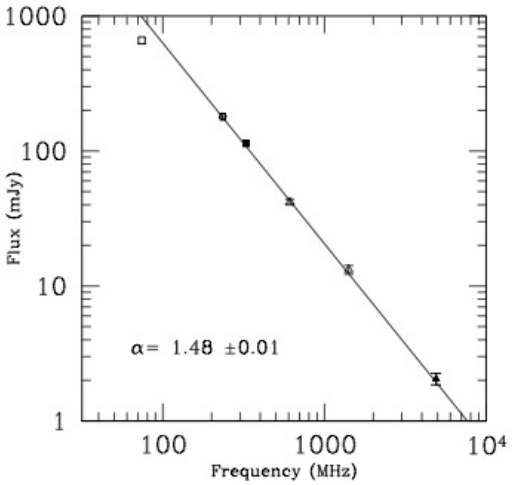

Figure 1.3: Spectral index of the radio relic in the cluster A521 between 74 MHz and 4.9 GHz. Source: Giacintucci et al. (2008).

.

§1.4.1. Radio Halos

Radio halos are faint, steep spectrum extended sources. Radio halos are generally unpolarised except in A2255 and MACS J0717.5+3745, where polarized filaments have been observed so far (Govoni et al., 2005), (Bonafede et al., 2009). The typical size of radio halos is roughly ∼1Mpc and radio halos indicate the presence of non-thermal components in ICM. The energy required to generate the non-thermal components is most likely provided by the gravitational processes of the merging cluster via shocks and turbulence (eg: Cassano and Others (2010) and references therein). There are 2 main hypotheses proposed to model the formation of radio halos which are still under investigation:

1. One model predicts that the electrons in ICM are reaccelerated during cluster mergers by mechanisms such as merger shocks, compression of fossil [2] electrons in ICM and magnetohydrodynamic perturbations (Ensslin et al., 1998),

2.Another model suggests that the relativistic protons generated in radio galaxies undergo inelastic collisions with thermal protrons in the intracluster medium and thereby produce radio emitting secondary particles which are observed as radio halos (Dennison, 1980). This model also predicts the spectral indices of cluster halos as $\alpha \approx -1.3 \pm 0.3$.

Currently available observational evidence indicates the radio halos are detected only in merging rich clusters thus supporting the first model mentioned above (Ferrari

[2]Fossil in this case refers to the old electrons present in the ICM of the galaxy cluster.

et al., 2008). However, sensitivity limits for current radio telescopes are insufficient to detect the hadronic halos predicted by the second model and thus the origin of radio halos remains an open question. There are several correlations between radio halos and the corresponding X-ray parameters as listed below ((Feretti, 2008) and references therein):
1. The power of the radio halo correlates directly with the cluster X-ray luminosity and in turn with gas temperature and total mass.
2. There is a point-to-point spatial correlation observed between the radio brightness of halo and X-ray brightness. This correlation was also observed using Chandra high resolution data. This confirms the connection between the Bremsstralung emitting hot plasma and relativistic plasma in the ICM.
3. The integrated radio halo spectra is generally steep and in the clusters where the spectral index maps are available, the radio spectrum steepens radially with distance from the cluster center. Also in region of highest temperature the spectral index was flat for the radio halo in A2744 and in general the steep spectral index correlates with low gas temperature.

These correlations strongly suggest that the reacceleration of relativistic particles and magnetic field amplication caused by the turbulence of the merging clusters supply the energy to the radio halo, but the theory will be fully tested by the SKA. Figure 1.4 is an example of a radio halo presented in correlation with the X-ray emission in MACSJ0417.5-1154 (Dwarakanath et al., 2011).

§1.4.2. Radio Relics

Radio relics are similar to radio halos in that, they are large diffuse low surface brightness sources (roughly $>$ 1 Mpc) with steep spectrum (α>1), but unlike halos, relics are detected in the peripheral regions of the cluster. Relics are strongly polarised (20 to 30%) radio sources with their major axis roughly perpendicular to the radius of the cluster. They typically range in size from roughly 100 kpc to $\sim$ 2 Mpc prompting the subdivision of the popultion into 'Relics' and 'Mpc scale Relics'. The acceleration mechanisms for these two classes are both believed to be Fermi I but differ in the details with small relics ($\sim$ 100 kpc) able to be reaccelerated by the fossil plasma of 'dead'[3] radio galaxies whereas 'Mpc-scale Relics' can be reaccelerated only through large-scale processes occuring across the cluster. Current models of

[3]Dead in this case refer to galaxies that stopped emitting radio waves from its Active Galactic Nucleus

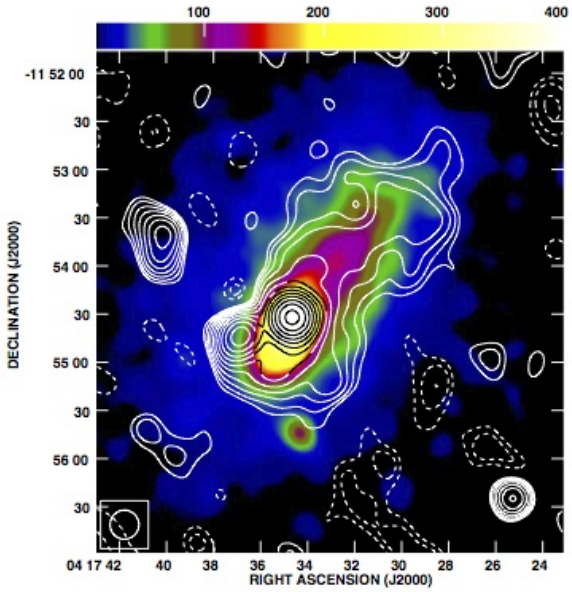

Figure 1.4: GMRT radio image overlaid (contours) on Chandra X-ray image (colours). The first contour is at 0.4 mJy/beam and increases in steps of $\sqrt{2}$. This image is an example of a radio halo detected in MACSJ0417.5-1154 and its corresponding correlation with the X-ray emission, source: Dwarakanath et al. (2011).

.

Mpc-scale radio relics suggest that the relativistic particles radiating in radio relics are powered by merger events in the clusters through the energy dissipated in shock waves. This is consistent with the elongated structure of the relics perpendicular to the merger axis (Feretti, 2008). In addition, numerical simulations show that cluster mergers generate shocks which can propogate to the cluster periphery (Ricker and Sarazin, 2001; Ryu et al., 2003). These accretion shocks reaccelerate the electron population by compressing the medium or fossil plasma and strengthening in-situ magnetic fields. Relics are found in clusters both with and without a cooling core, suggesting that they may be related to minor or off-axis mergers, as well as to major mergers. The radio power of the relic correlates with X-ray luminosity similar to halos indicating the link between thermal and relativistic plasma in the peripheral regions of the clusters ((Feretti, 2008) and references therein).

The source of the accelerating electrons required for halo generation is still unknown, however Wide Angle Tailed (WAT) radio galaxies may provide fossil reservoir of electrons for reacceleration through sub cluster mergers (Burns et al., 1994).

The Figure1.5 is an example of a radio relic shown with X-ray emission in A521. The radio contours were generated using GMRT 610 MHz observations and they are

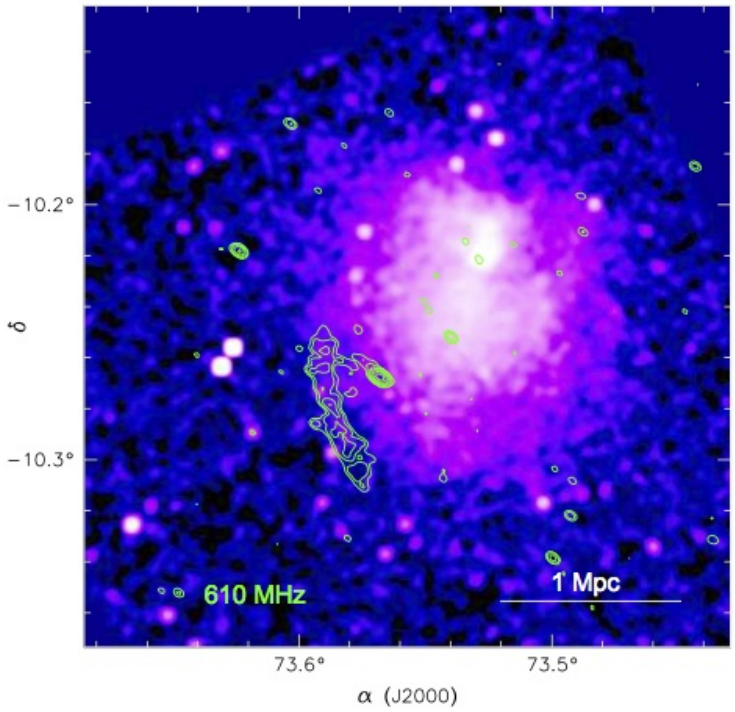

Figure 1.5: An example of radio relic at the edge of Abell 521. GMRT radio image overlaid (contours) on the Chandra X-ray image (colours). The resolution of the above image is 13.1 arcsec x 8.1 arcsec. Contour levels were spaced by a factor of 2 starting from 0.2 mJy/b. Source: Giacintucci et al. (2008).

overlaid on the Chandra X-ray image (Giacintucci et al., 2008).

§1.4.3. Mini-halos

Mini-halos are diffuse radio emitting sources that are found in some relaxed, cool-core clusters. The size of mini-halos generally range from roughly 100 kpc to 500 kpc. Radio emitting particles in mini-halos are likely associated with the ICM in the cooling flow region. The correlation observed between mini-halo radio power and the cooling flow power supports the idea that mini-halos are powered by the energy of the cooling flow ((Gitti et al., 2007) and references therein). The ICM in the centres of galaxy clusters should be rapidly cooling at the rate of tens to thousands of solar masses per year and this occurs as the ICM (a plasma) is quickly losing its energy by the emission of X-rays. The typical timescale for the ICM to cool is relatively short, less than a billion years. As material in the centre of the

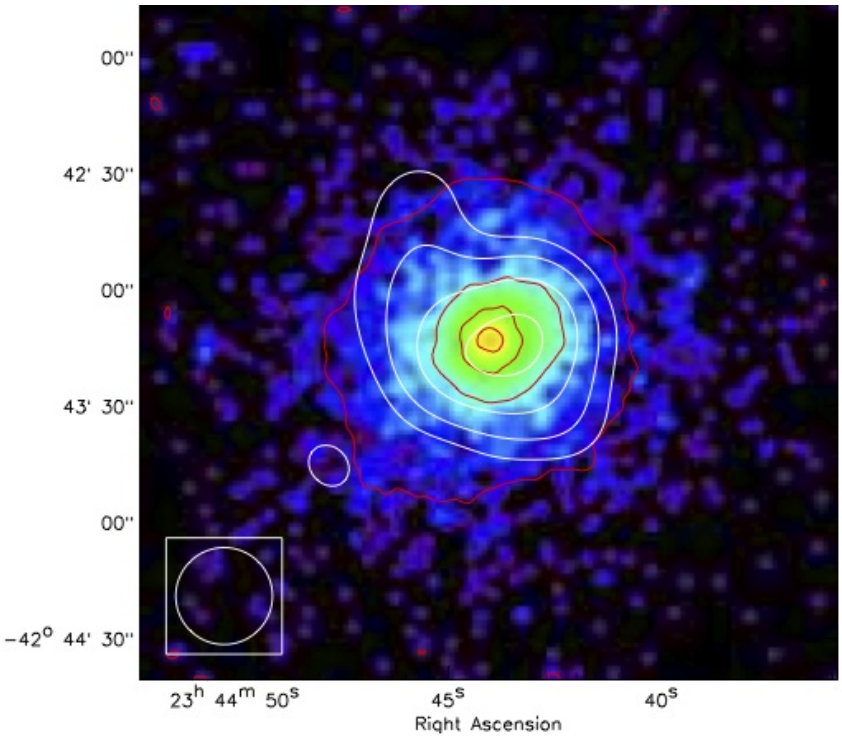

Figure 1.6: An example of a mini halo in the Phoenix cluster. GMRT radio image overlaid (contours) on the Chandra X-ray image (colours). Red contours are X-ray isophotes drawn at levels of [1, 10, 50, 200] x $10^{-5} ctss^{-1} pixel^{-1}$. GMRT 610 MHz low-resolution radio contours are overlaid in white. Contour levels are drawn at $\sqrt{1, 2, 4, 8, ...} \times 0.6 mJybeam^{-1}$. Source: van Weeren et al. (2014)

cluster cools out, the pressure of the overlying ICM should cause more material to flow inwards (the so-called 'cooling flow') (Fabian, 1994). Recently an idea has been put forward by Mazzotta and Giacintucci (2008) and ZuHone et al. (2013) which states that sloshing motions induced by minor mergers and the resulting turbulence is capable of re-accelerating electrons and these electrons could form a mini-halo in the presence of magnetic field. The Figure 1.6 below is an example of mini-halo present in the Phoenix cluster. The radio contours were generated using GMRT 610 MHz observations and they are overlaid on the Chandra X-ray image (van Weeren et al., 2014).

Table 1.1 summarises the characteristics of the different extended diffuse radio sources in clusters (Kempner et al., 2004).

Table 1.1: Properties of Radio halos, Relics and Mini-halos

Source type	Size	Morphology	α	Polarization (%)
Radio halo	$\gtrsim$ 1 Mpc	Centrally peaked diffuse source with possible sub-structure and it could be asymmetric	$\lesssim$ -1.1	None
Radio relics	few 100 kpc to 1 Mpc	Mostly diffuse, two symmetric sources with possible filaments	$\lesssim$ -1.2	10-30
Mini-halos	few 100 kpc	Diffuse and centrally peaked with possible substructure and it could be asymmetric	$\lesssim$ -1.5	few

§1.5. Thesis Summary

The original purpose of this thesis was to investigate suitable clusters detected in two samples (REXCESS Southern Sample) and the massive SPT cluster sample in order to assess likely diffuse emission for follow up with the Murchison Widefield Array (MWA) observations. In the course of this work our thesis has evolved to focus on the cluster with the most prominent diffuse radio emission. Thus, in this thesis, we focus on the diffuse radio emission in the Bullet cluster (1E 0657 -5558) from 118 MHz to 8.896 GHz. The Bullet cluster hosts a prominent X-ray bow shock, as well as (Liang et al., 2000) (Shimwell et al., 2014)(Shimwell et al., 2015) one of the largest linear size halo ever detected at 1.4 GHz (Giovannini et al., 2009) and a radio relic which is thought to be accelerated from seed electrons of a radio galaxy. In this thesis we present an investigation of the Bullet cluster from 1.4 GHz to 8.896 GHz using archival data from the Australia Telescope Compact Array (ATCA), which is supplemented with new low frequency 100-200 MHz data from the Murchison Wide Array (MWA).

This thesis is laid out as follows:

Chapter 2: An introduction to radio telescopes and radio data reduction.

Chapter 3: Initial shortlisting of target clusters with potential diffuse emission.

Chapter 4: Results of data detection for the Bullet cluster and analysis of radio relic in the cluster.

Chapter 5: Analysis of the known radio halo in the Bullet cluster from 118 MHz to 8.896 GHz.

Chapter 6: Conclusion.

We assume a concordance ΛCDM cosmology, with $\Omega m = 0.286$, $\Omega\Lambda = 0.714$ and $h = H0/(100\ kms^{-}1Mpc^{-}1) = 0.696$. At $z = 0.296$, the luminosity distance of 1E 0657 -55.8 is 1542.3 Mpc and 1 arcsec corresponds to 4.452 kpc. All coordinates are given in J2000.

§2. Radio telescopes

This chapter provides a brief introduction to radio antennas and their application as radio telescopes. This chapter also briefly discusses radio interferometry and its relation to Young's slits. We also discuss about the ATCA and the MWA telescopes as data from these were used for the purposes of this thesis. ATCA data reduction techniques are discussed in this chapter along with an introduction to the data reduction tool - MIRIAD (Mutichannel Image Reconstruction, Image Analysis and Display).

§2.1. Radio antennas

This section provides a brief outline of radio antennas and their application as radio telescopes. An antenna is a device that can be used for converting electromagnetic radiation into electrical currents in its conductors or vice-versa depending on whether it is used for receiving or transmitting. Radio telescopes are radio antennas that are used to observe astronomical objects in the radio frequency band of the electromagnetic spectrum (3 MHz to 30 GHz). Radio telescopes are receiving antennas and only half wave dipole antennas and their relatives or quarter wave ground plane verticals are mostly used. A dipole antenna consists of bilaterally symmetrical conductive elements such as metal wires or rods. The length of the dipole elements is determined by the wavelength of the radio waves that needs to be received. The most common form is the half wave dipole which consists of two dipole elements approximately a quarter wavelength long thereby making the whole antenna half a wavelength long. Quarter wave ground plane verticals are monopole antennas which consist of a straight rod shaped conductor typically mounted perpendicular to a ground plane, usually the Earth. The antenna is approximately 1/4 of a wavelength of the radio waves that needs to be received. Half wave dipoles are normally used as feeds at low frequencies ($\nu < 1GHz$). For higher frequencies, quarter wave ground plane verticals are used inside the waveguide horns.

The typical elements of a standard radio telescope are the feed, reflector, transmission line and the receiver (see Fig 2.1). The reflector of a radio telescope is used to focus the plane radio waves into the feed. The reflector also provides directionality.

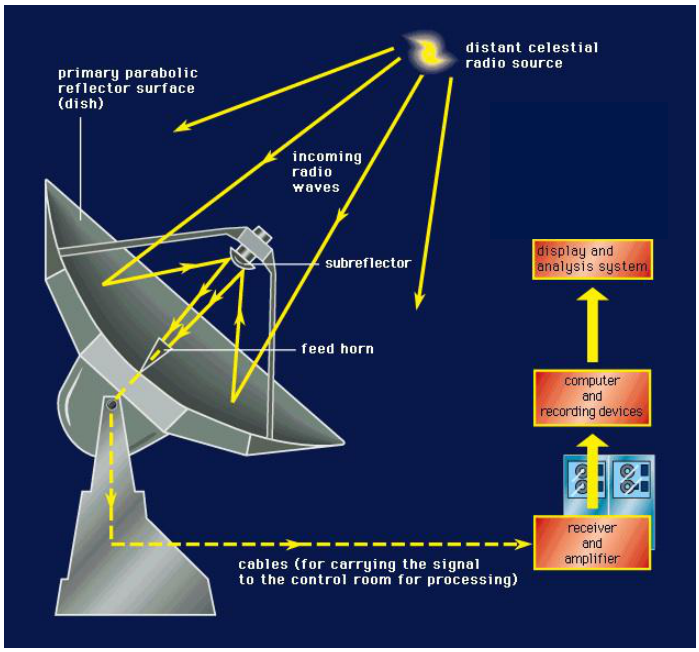

Figure 2.1: The above image shows the basic components of a standard dish type radio telescope. Image reference: Encyclopaedia Britannica.

The feed of a radio telescope collects radiation from the reflector and converts it to a tiny radio frequency voltage which is then amplified by the receiver. The processed signal from the receiver is then transmitted to computing devices for storage, imaging and analysis. When a radiation of wavelength λ passes through an antenna aperture of diameter D, the radiation diffracts into a beam with angular size $\theta = \lambda/D$.
The power collected by an antenna is given by

$$P = S_\nu A \delta\nu \tag{2.1}$$

where, S_ν is the flux density of the astronomical source, A is the area of the antenna and $\delta\nu$ is the frequency interval or bandwidth of the measured radio wave. This implies that the area of the antenna is directly proportional to its power and larger the area of the reflector, the greater the power that is collected. The gain of a receiving antenna indicates how effectively the antenna converts the incoming radio waves from a specific direction into electrical power. The gain is derived by comparing the actual power received by the antenna to the power received by a hypothetical lossless half-wave dipole antenna. The gain is related to the effective collecting area of the antenna A and is given by $G = 4\pi A/\lambda^2$.
A plot of the gain as a function of direction gives the radiation pattern of the antenna

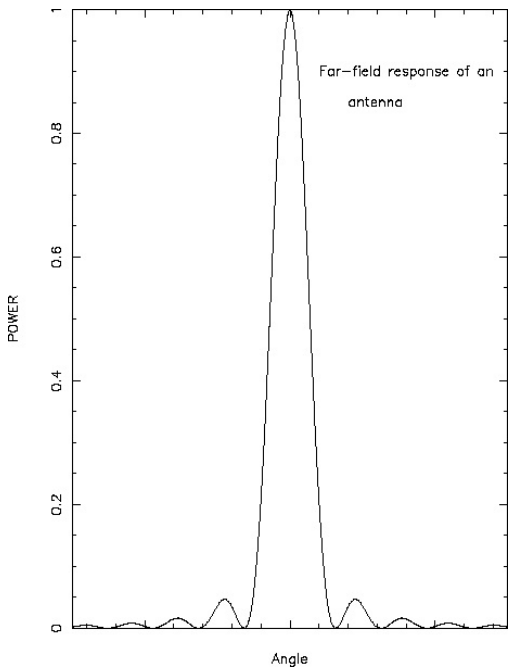

Figure 2.2: The above image depicts the plot of the gain of an antenna as a function of direction.

(see Fig 2.2). The response pattern of a directive antenna shows a pattern of a main lobe and side lobes. The main lobe (called as 'Primary Beam' in radio astronomy) represents the direction of the receiving antenna where the maximum power is received and the side lobes represent the radiation from unwanted directions around the telescope. The side lobes may pick up interfering signals that could add to the noise in the receiver. In an antenna response pattern, there will be a front main lobe in the direction in which the antenna is oriented and there will be side lobes pointing to other directions (see Fig 2.3). The back lobe is a side lobe which is 180° opposite to the main lobe and this is effectively blocked by the structure of the dish in radio telescope arrays.

Parabolic antennas are commonly used in radio astronomy and the parabolic reflector focusses the plane radio waves to a single point and is coupled to a transmission line using a feed horn. The feed horn can be placed at the prime focus or at secondary focus. A major problem with prime focus arrangements for large aperture antennas is that the equipment required at the prime focus is heavy and the supporting structure tends to sag under the weight of the equipment which would affect calibration. Cassegrain antennas are the solution to the problem which consist of a secondary reflecting surface to redirect the electromagnetic waves back to the prime focus near the primary reflector (see Fig 2.4).

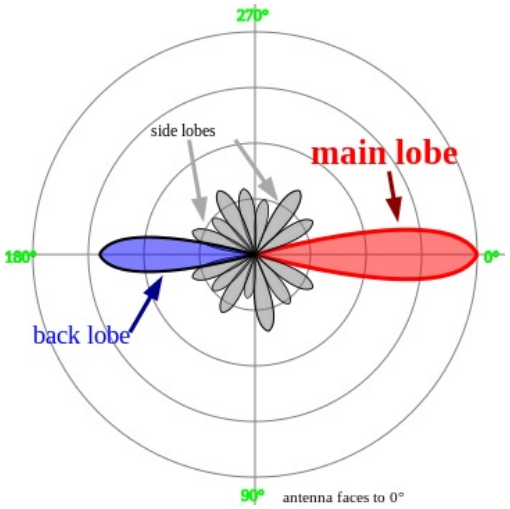

Figure 2.3: The above image depicts a schematic of a response pattern of an antenna with main lobes and side lobes.

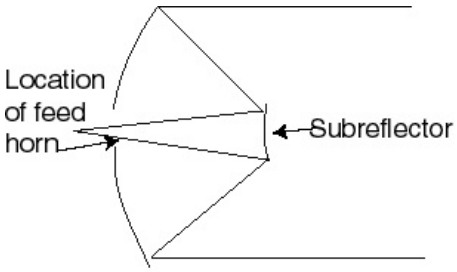

Schematic of a Cassegrain System

Figure 2.4: The above image depicts a schematic of Cassegrain system.

§2.2. Interferometry using radio telescopes

Radio telescope observations can be made using a single dish telescope or an array of dishes/antennas. The technique combining an array of dishes/antennas to probe structures with higher resolution is called Radio Interferometry. This section provides a brief introduction to Young's slit experiment and its application in Interferometry. This section is largely based on the review article written by Neal Jackson on Principles of interferometry (Jackson, 2008).

§2.2.1. Young's slits

Young's slit fringe patterns forms the basis for Radio interferometry. Interference fringes are observed when a source emitting coherent radiation passes through the slit separation. Constructive and destructive inferences are observed when the relative delay of two interfering rays change due to phase difference between the waves. The angular separation of the fringe caused by this path difference of waves can be given by λ/d, where d is the slit separation distance and λ is the wavelength of light. Fringe visibility is defined as the ratio of the difference between maximum and minimum intensities and the sum of maximum and minimum intensities $((I_{max} - I_{min})/(I_{max} + I_{min})$. If the radiation emitting source is wider than the angular separation of the fringe λ/d, the fringe visibility drops because the angular displacement of the source produces an equal angular displacement in the fringe pattern and integration of this incoherent fringe patterns resulting in reduced visibility. If the source size approaches λ/d, the fringe patterns will add to give a constant illumination thereby reducing the visibility to zero (see Fig 2.5). Conversely, when the angular size of the source is much smaller than λ/d, the fringe visibility reaches its maximum. Similarly assuming the source size as constant, if the slit spacing d is decreased, the displacement of the fringe patterns reduce and thereby increasing the visibility of the source. In short, the smaller the slit separation, the larger the source size that can be probed and vice versa (see Fig 2.6). This relationship is applied in radio interferometers for probing structures in the universe where the slit separation is nothing but the baseline distance between two telescopes and the source would be any target source in the universe which needs to be observed. The resultant interference pattern response can be obtained by electronically multiplying the signal from the first telescope with the signal from the second. The distance between the telescopes can be varied similar to varying the slit separation distance depending on structure of the source.

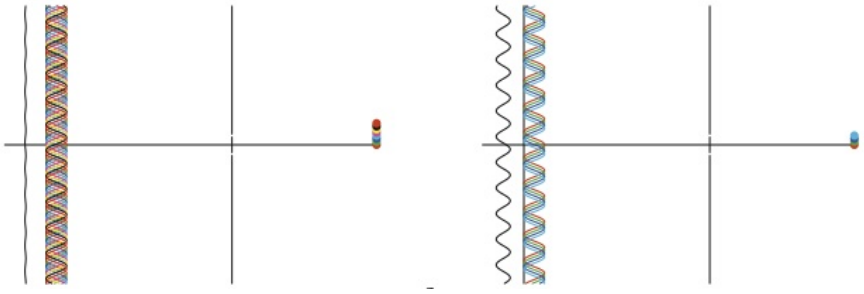

Figure 2.5: In this Figure, the source is represented by a sequence of point sources in different colours representing different points in the source. The image on the left indicates that the angular displacement in each point of the source produces an equal angular displacement in the fringe pattern produced by the source and when the source size reaches λ/d, the fringes add to give zero visibility. The image on the right indicates that the fringe visibility pattern increases towards maximum when the source size gets smaller than λ/d and when the angular size of the source is $\ll \lambda/d$, the fringe visibility is maximum.

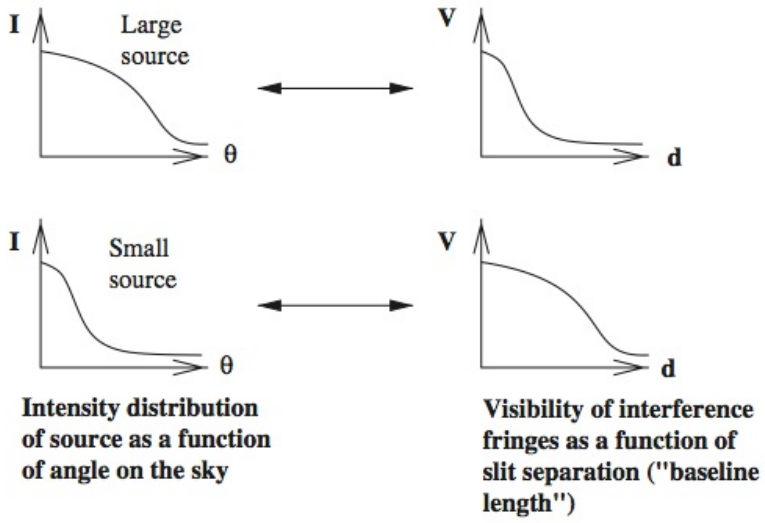

Figure 2.6: The above plots shows the relation between source intensity as a function of angular distance and its corresponding relation between visibility of interference fringes with respect to slit separation length.

§2.2.2. Radio Interferometry and uv plane

In Young's slit experiment, an interference pattern as a function of delay can be generated by applying a delay to one wave with respect to the other. The same could be applied in many situations in real interferometers. Consider a plane wave from a source σ at infinity is sampled by two radio telescopes separated by a vector distance $\vec{B}$ (see Fig 2.7). The path difference of two waves arriving at the telescopes is given by $\vec{B} \cdot \vec{s}$ where $\vec{s}$ is the unit vector towards the direction of the source. The phase delay between the waves can be given by $k\vec{B} \cdot \vec{s}$, where k is the wave number which is equivalent to $2\pi/\lambda$. Assuming the electric field received by the first telescope is E, the electric field by the second can be represented as $Ee^{ik\vec{B}\cdot\vec{s}}$ by considering the phase delay. These signals can be combined electronically by multiplying them together. We can derive the response of the interferometer R by integrating the fringe patterns over different parts of the source. Response of the interferometer R can be represented as

$$R = \int I(\sigma) e^{ik\vec{B}.(\vec{s}+\vec{\sigma})} d\sigma \tag{2.2}$$

where $\vec{s} + \vec{\sigma}$ is the vector in the direction of the small part of the source (dσ) and intensity is I(dσ). Since $\vec{\sigma}$ is parallel to the projected baseline $\vec{b}$ and since the distance to the source is very large, $\vec{B}.\vec{\sigma}$=$\vec{b}.\vec{\sigma}$ and therefore the above equation can be rearranged as

$$R = e^{ik\vec{B}\cdot\vec{s}} \int I(\sigma) e^{ik\vec{b}\cdot\vec{\sigma}} d\sigma \tag{2.3}$$

where $e^{ik\vec{B}\cdot\vec{s}}$ is determined by the array geometry and hence it is removed out of the integral. The resultant part of the integral represents the series of fringes whose amplitude is the Fourier transform of the source intensity distribution. The fringes can be removed by applying the necessary electronic delays. After the fringes are removed the resultant response just represents the information of the source with an amplitude and a phase.

The decomposition of source $\vec{\sigma}$ is a vector in the sky plane which can be represented in Cartesian coordinates as $\vec{\sigma} = \sigma_x \hat{i} + \sigma_y \hat{j}$. Similarly the projected baseline vector $\vec{b}$ can be represented as $u\hat{i}$+$v\hat{j}$. The scalar product of $\vec{b}\cdot\vec{\sigma}$ becomes ux+vy. Substituting this scalar product in the above response equation, the value of R can be derived as

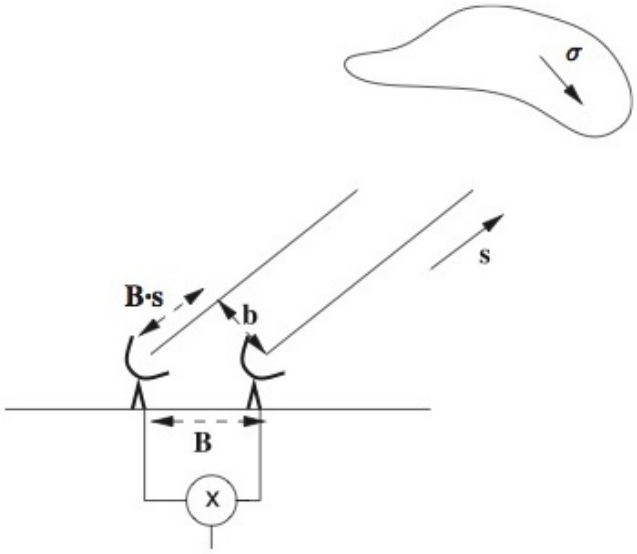

Figure 2.7: The above image depicts a two element basic interferometer observing a source in a direction with unit vector $\vec{s}$.

follows, which would be a 2-D Fourier transform

$$R(u,v) = \int\int I(x,y)e^{2\pi i(ux+vy)}dxdy \tag{2.4}$$

As the earth rotates, the projected baseline length b changes along with the rotation and the corresponding change in amplitude and phase are captured in the Fourier plane as Fourier transformed intensity distribution. This plane which captures the change in response of the interferometer when the earth rotates is called the uv plane and generally it follows an elliptical path depending on the declination of the source. This Fourier plane is inverse Fourier transformed to generate an image depending on the point spread function of the source on the uv plane. If many baselines are present, many more measurements can be made in the uv plane. And the more completely the Fourier plane is filled, a more precise interferometric image can be reproduced. The array configuration of the telescope determines the type of source that can be observed based on its baseline length. Longer baselines are used to measure point sources as the point source image resolve better and shorter baselines are used to detect and measure extended sources. The ideal baseline length is inversely proportional to the size of the source ($\theta = \lambda/D$).

In this thesis, we are using data from ATCA (Australia Telescope Compact Array) and MWA (Murchison Widefield Array) telescopes. The following sections gives a

brief introduction on both these telescopes.

§2.3. Australia Telescope Compact Array

The ATCA is an array of six 22-m antennas located near the town of Narrabri in New South Wales. Five of the antennas are located on a 3 km track and the 6^{th} antenna is fixed 3 km west of the western end of the primary track making the maximum baseline length as 6 km. The array has a 214m spur in its east west track. The array can be used for observations in five wavelength bands between frequencies ranging approximately between 1.1 GHz and 105 GHz. The array configuration is determined by the location of six antennas and with one antenna fixed, the remaining five antennas can be positioned in any of the 44 fixed stations. The stations provide main power and network connections to the antennas. A standard set of 17 configurations can be defined in ATCA and these configurations are chosen depending on the extent, brightness and complexity of the source.
The ATCA is an earth-rotation aperture synthesis radio interferometer and array of antennas in the ATCA comprises a number of two element interferometers (eg: baseline 1-2, baseline 1-3, baseline 1-4 etc.) and the visibilities are derived by multiplying the signals from each pair. After combining the correlated signals over a period of time and with sufficient spacings between antennas, the spatial coherence function can be measured. According to Van Cittert-Zernike theorem, the spatial coherence function can be used to produce the radio image of the source using Fourier transform. UV coverage can be obtained by plotting the tracks of the baseline vector as the earth rotates in the Fourier plane and it can vary by array configuration. Figure 2.9 gives an example of *uv* coverage for different configurations of antenna pointing to the same source. In order to obtain the fullest *uv* coverage, the ATCA would require multiple configuration observations for 12 hours per configuration. But many observations can be carried out with less than complete *uv* coverage and with individual configurations. Off-line image processing techniques minimise the effects of reduced uv coverage and could be used to generate good images with single configurations.

§2.3.1. What is CABB?

The Compact Array BroadBand Backend (CABB) upgrade has provided a new broadband backend system where the observing bandwidth was increased from 128 MHz to 2 GHz - a factor of 16 improvement. Each 2 GHz window can be split

Figure 2.8: Five of the ATCA antennas. Credit:CSIRO

into 2048, 512, 128, or 32 primary channels. CABB enabled the computation of all stokes parameters by the new correlator in all available modes. The digitisation level was also improved from 2 bits to 9 bits thereby increasing the correlator efficiency and consequently lowering system temperature. The following improvements were achieved as part of the CABB upgrade (Wilson et al., 2011):

1. Increased bandwidth reduced the integration time required for observations.

2. Narrow band interference can be precisely removed with the help of narrow and independent channels.

3. The splitting of the primary Intermediary Frequency (IF) band into a large number of channels allows for a significant improvement in the *uv* coverage for a single observation.

4. Large fractional bandwidth of CABB at low frequencies (1 - 10 GHz) enables the study of the spectral behaviour of continuum sources without resorting to frequency switching.

5. Large frequency coverage of CABB allows projects to simultaneously observe multiple spectral lines that fall within 8 GHz of each other at high frequencies (16 - 105 GHz).

6. The correlator could be configured to provide the most suitable compromise of

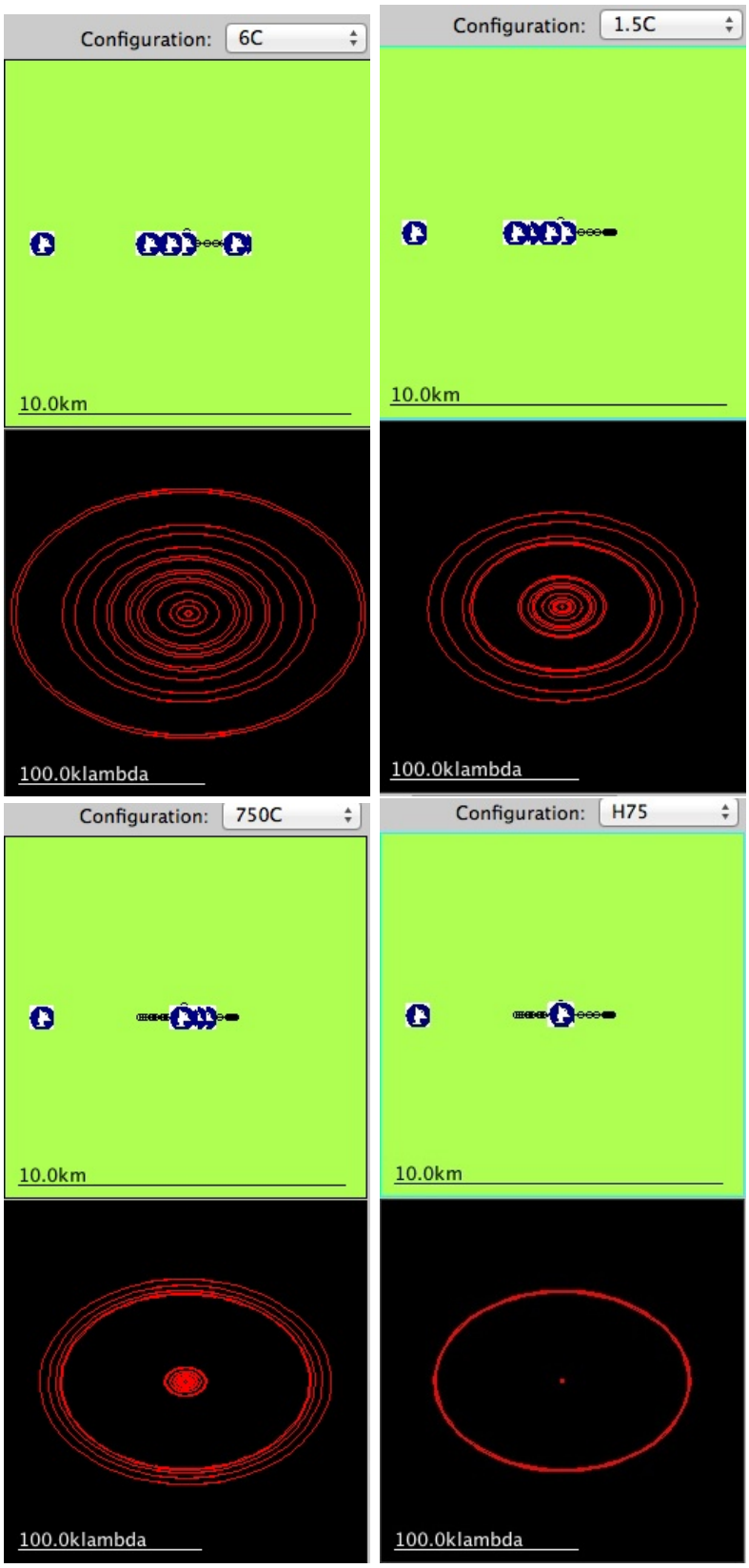

Figure 2.9: The top panel gives the positions for each antenna in the Australia Telescope Compact Array (ATCA). The bottom panel is the corresponding uv-plane coverage for a 12 hour observation, using different combinations of antenna configurations for a source with same latitude -56.54.

sensitivity, speed and resolution for any particular observation by varying the width of each channel in the primary bands.
In this thesis, both CABB and PreCABB data are used for data reduction and flux density measurement.

§2.3.2. Reduction of ATCA data

This section provides a brief introduction on the ATCA data reduction process. We mainly focus our discussion on the steps that were used to reduce data in this thesis. Data reduction is a process of converting the raw telescope data into a radio image. MIRIAD was the data reduction package used for reducing ATCA data in this thesis. MIRIAD supports calibration and analysis of polarimetric data from the ATCA, multi-frequency synthesis imaging, mosaicing, ATCA pulsar bin mode, and specialised spectral line observations (Sault et al., 1995). All MIRIAD tasks have parameters that can be passed when running them and some of them are compulsory while the others are optional where the default value will be used by the package to run the task if there is no parameter specified. There are two approaches to using MIRIAD. One is the command line approach where commands are passed directly at the system prompt and the other approach involves invoking MIRIAD commands using another program. In this thesis all the data reduction tasks were performed using the command line approach. A MIRIAD dataset consists of two parts. One part consists of the calibration tables while other is a stream of variables. The stream of variables consists of parameters known at the time of observation like the observing frequency, the observing centre, the source name, (u, v) coordinates, the baseline number, the polarisation parameter being measured, etc. The calibration table parameters are derived usually using the observations of a calibrator. Calibration tasks in MIRIAD can produce or use items in the calibration tables & parameters are antenna based that are used to derive the response of each antenna.
The process of data reduction using MIRIAD involves the following stages
1. File format conversion and extraction
2. Calibration and Radio Frequency Interference (RFI) flagging
3. Imaging

File format conversion and extraction

ATCA data was downloaded from the ATCA data archives for data reduction and the initial file format of the data is in RPFITS. This file format needs to be converted to MIRIAD format before any further processing can be done. Task atlod converts a *uv* dataset from RPFITS format to MIRIAD format. Task atlod has standard parameters of IN and OUT which represent the path of the input RPFITS file and output in MIRIAD format respectively. OPTIONS parameter in the atlod task provides some processing options when converting the file format. Generally options of xycorr and birdie are used for both CABB and PreCABB data reduction. XYCORR option is generally applied for correcting the phase difference between the channels that occur during online polarimetric measurements. Option BIRDIE is used to flag out the channels that suffer self interference. Option RFIFLAG is used for CABB data which flags the RFI caused at low frequencies as the large bandwidth of the CABB correlator makes it difficult to avoid most of the known RFI. Option NOAUTO was also used for CABB data reduction in this thesis to discard the cross correlation data. After the file format conversion, task UVSPLIT could be used to extract single source, single frequency datasets from the multi-source, multi-band dataset. In the case of CABB datasets, UVFLAG task was used before the UVSPLIT to flag the edge channels (an area of about 32 MHz on each side) that are less sensitive than the central parts.

Calibration and flagging

The calibration parameters are based on the antenna and a model of the response of each antenna can be derived with the calibration data. The response of an antenna is modelled by antenna gains, delay factors, antenna bandpass functions and antenna leakages (Sault and Killeen, 1998). The calibration process calculates the solutions for these factors. Calibration task is performed using a primary calibrator and a secondary calibrator. In the case of ATCA, primary calibrator is always PKS B1934-638 and it is used to calibrate the flux density scale. The secondary calibrator is generally the source near the target and is used for deriving phase solutions. In MIRIAD, tasks MFCAL and GPCAL are generally used for calibration of ATCA data. The task MFCAL solves for antenna gains and bandpass functions. Parameter VIS is used for passing the input dataset which would be the primary or the secondary calibrator dataset. Parameter INTERVAL denotes maximum solution gap and was set to 0.5 (50 seconds) for PreCABB data and 0.1 (10 seconds) for CABB dataset.

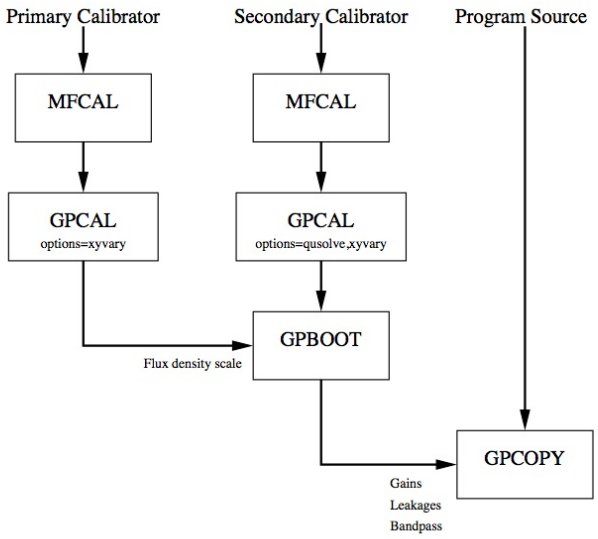

Figure 2.10: A flow chart from the MIRIAD user manual showing the steps involved in standard ATCA calibration process.

Task GPCAL is the one of the main tasks for calibration and it determines calibration corrections (both antenna gains and instrumental polarisation characteristics) for an array with dual feeds, from an observation of a point source. Task GPCAL can handle either dual linear or dual circular feeds. GPCAL can be used to solve instrumental polarisation by calculating the leakage terms with the primary calibrator and to solve for the polarisation of the secondary calibrator. Option QUSOLVE (solves for stokes Q and U) is used for solving polarisation solution of the secondary calibrator. Other option used in GPCAL is XYVARY which solves for the phase difference between the feeds and this is used in both primary and secondary calibrator datasets. To complete the calibration, the flux density scale determined for the primary calibrator is transferred to the secondary calibrator using the task GPBOOT. Task GPCOPY is then used to copy the secondary calibration tables to the target source which will copy both the primary calibrated flux density scale and the secondary phase solutions to the target source. Fig 2.10 shows the flow chart with the steps in standard ATCA calibration process.

Once the initial calibration is complete, both primary and secondary calibrator

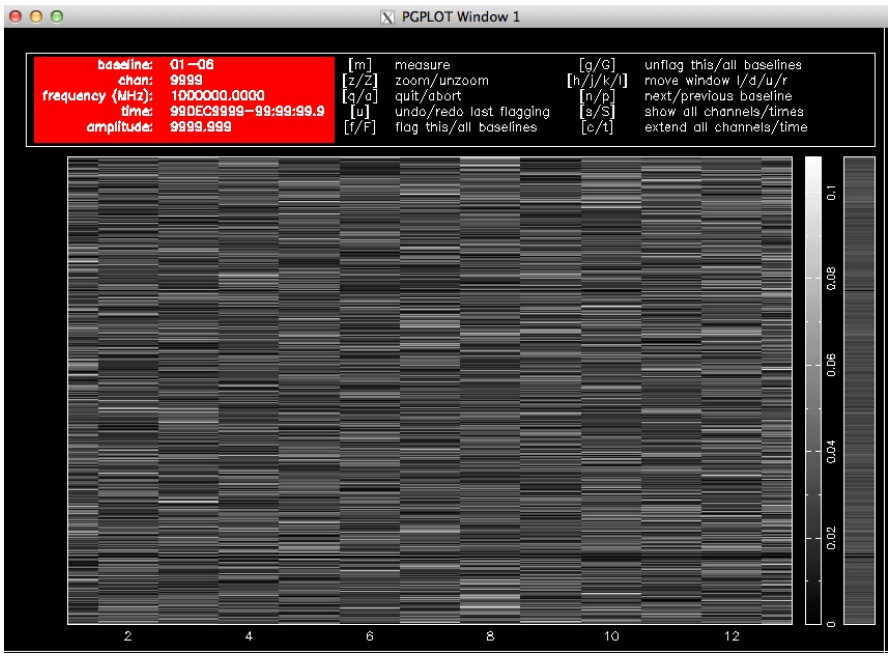

Figure 2.11: Screenshot of a waterfall plot generated for Stokes=V after using PGFLAG for 1-6 baseline. The above plot shows that there is no remaining RFI.

data should be flagged to remove any RFI in the data. Tasks PGFLAG and BLFLAG were used for flagging the datasets in this thesis. Task PGFLAG allows interactive baseline editing of *uv* dataset and it displays a waterfall plot with channel as the x-axis, time as the y-axis and amplitude as the colour of each pixel. Fig 2.11 shows the screenshot of a waterfall plot generated using PGFLAG. Task BLFLAG was used to remove further RFI in the datasets. This task can generate many type of plots (e.g. time vs amplitude), which may allow the user to directly select the outliers representing bad data. Task BLFLAG plots the visibilities either a baseline at a time or all at once and thereby allowing to flag the discrepant points using the plotting cursor. Fig 2.12 shows the screenshot of a BLFLAG plot screen plotted in real and imaginary axis for all baselines. Plot type can be passed in the parameter AXIS in the BLFLAG task. RFI flagging was done for all stokes parameters (I, U, Q and V) across all baselines. Once the flagging is complete for primary and secondary calibrators, recalibration tasks needs to be performed and the calibration solution should be copied to the target source.

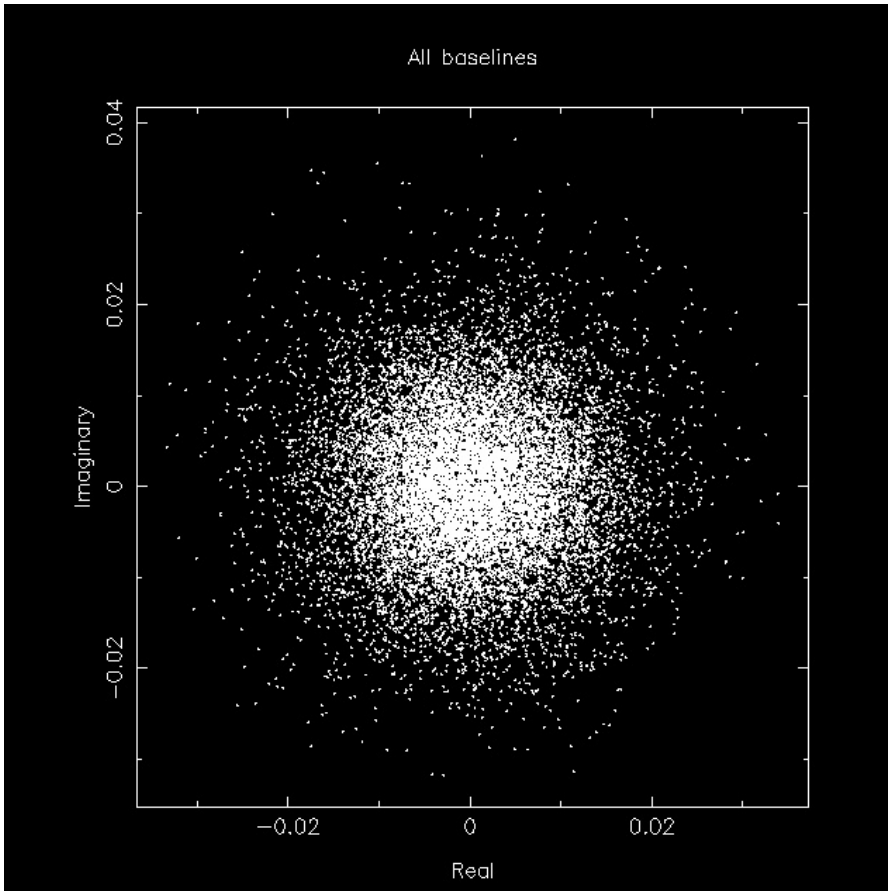

Figure 2.12: Screenshot of real vs imaginary plot generated for Stokes=V using BLFLAG for all baselines. Please note that two-dimensional Gaussian distribution of points suggests that there is no remaining RFI.

Imaging

The process of imaging generally involves three tasks in MIRIAD which are run sequentially starting from INVERT, CLEAN or MFCLEAN and RESTOR. INVERT is a task that forms images from visibilities. It can generate images for different polarisations and can also handle multi-frequency synthesis and mosaicing observations. The process of forming a single continuum image from a variety of frequencies is called 'multi-frequency synthesis' (MFS). It produces an image with a frequency corresponding to an average of the frequencies comprising the input data. OPTION parameter in INVERT can be set to 'mfs, mosaic' to perform multi-frequency synthesis and mosaicing on the image. INVERT can combine several visibilties together to generate a combined image. This task generates a map which is a dirty image from the visibility dataset. Also this generates a dirty beam which is a point spread function corresponding to all image planes and Stokes parameters. The beam is generated to deconvolve the side lobes from the dirty map. Fig 2.13 shows a sample dirty map and dirty beam generated using the INVERT process. The optimum weighting for detecting a Gaussian source is to weight the visibility data by a Gaussian. This is often called 'tapering'. Using a Gaussian weight will significantly increase the detectability of an extended source but it degrades the resolution. FWHM is an optional parameter in INVERT task that could be used to apply a taper on the image. Option IMSIZE can be used to set the size of the output dataset and option CELL can be used to set the image cell size in arcsec. Cell size and image size were calculated using the formula $\theta = \lambda/D$, where θ is the angular resolution of the image, λ is the wavelength of observation D is the distance between the furthest baseline.

The Högbom CLEAN algorithm in MIRIAD was used to iteratively clean the dirty map and produce clean components. Dirty images produced by INVERT (continuum, line, MFS, Stokes) can be deconvolved with CLEAN task in MIRIAD. The Högbom CLEAN algorithm represents the image as a number of point sources in an otherwise empty field of view and the algorithm looks for the brighest pixel in a specified region in the image. It subtracts a fraction of the dirty beam from the dirty image at the location of that brightest pixel. This subtracted image is called the residual image. The search and subtraction loop would be repeated until the sidelobes in the image were reduced to below the noise level. Fig 2.14 shows a sample clean component image generated using the CLEAN task. MFCLEAN task is similar to CLEAN and is used to deconvolve an MFS image. The MOSSDI task was also used to clean some datasets and this task performs a steer CLEAN on a mo-

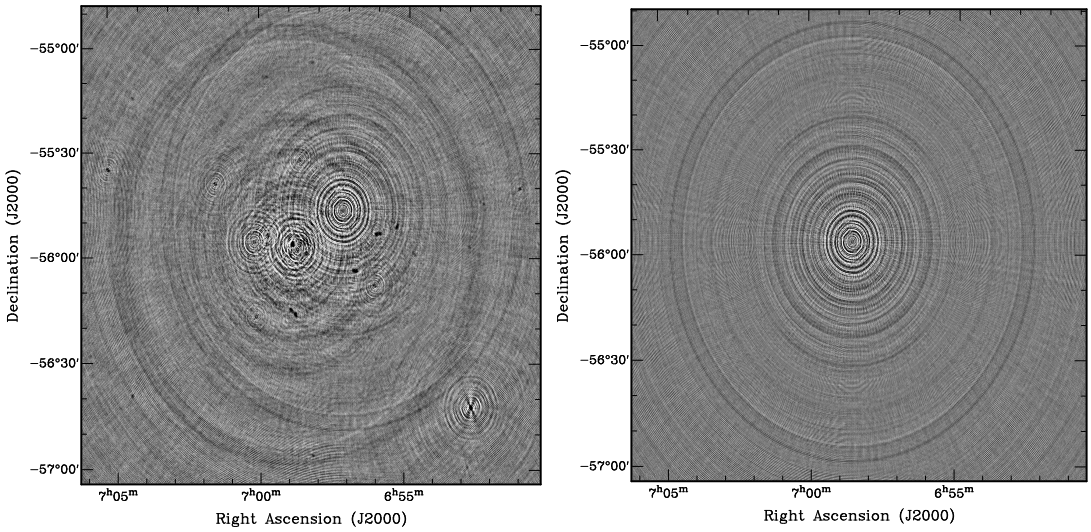

Figure 2.13: Screenshot of a dirty map image on the left and its corresponding dirty beam image on the right.

saiced image. We used MOSSDI for cleaning the dirty maps generated from CABB datasets.

Task RESTOR is performed after the CLEAN task where the final image can be generated by calculating residuals and convolving a model by a 'CLEANED' Gaussian beam. Task RESTOR in MIRIAD fits the dirty beam with the Gaussian CLEAN beam, and produces a restored image. This task is usually the final step in data reduction process for producing images. Task IMPOL is used to generated the polarisation intensity and polarisation position angle images from Stokes I, Q and U images.

§2.4. Murchison Wide Array

The MWA is a low frequency radio telescope that operates at a frequency range of 80 MHz to 300 MHz. MWA is located in Western Australia and is one of the precursor telescopes for SKA (Square Kilometre Array). The MWA consists of 2048 dual-polarization dipole antennas optimised for the 80-300 MHz frequency range, arranged as 128 "tiles", each a 4x4 array of dipoles. Each antenna with its 16 dipoles is known as a "tile". The array does not have moving parts and all telescope functions are performed by electronic manipulation of signals. The core area has 50 antenna tiles uniformly distributed over a 100 metre diameter core, surrounded by 62 tiles which are distributed over a 1.5 km diameter circle (see Fig 2.15). The final 16 tiles

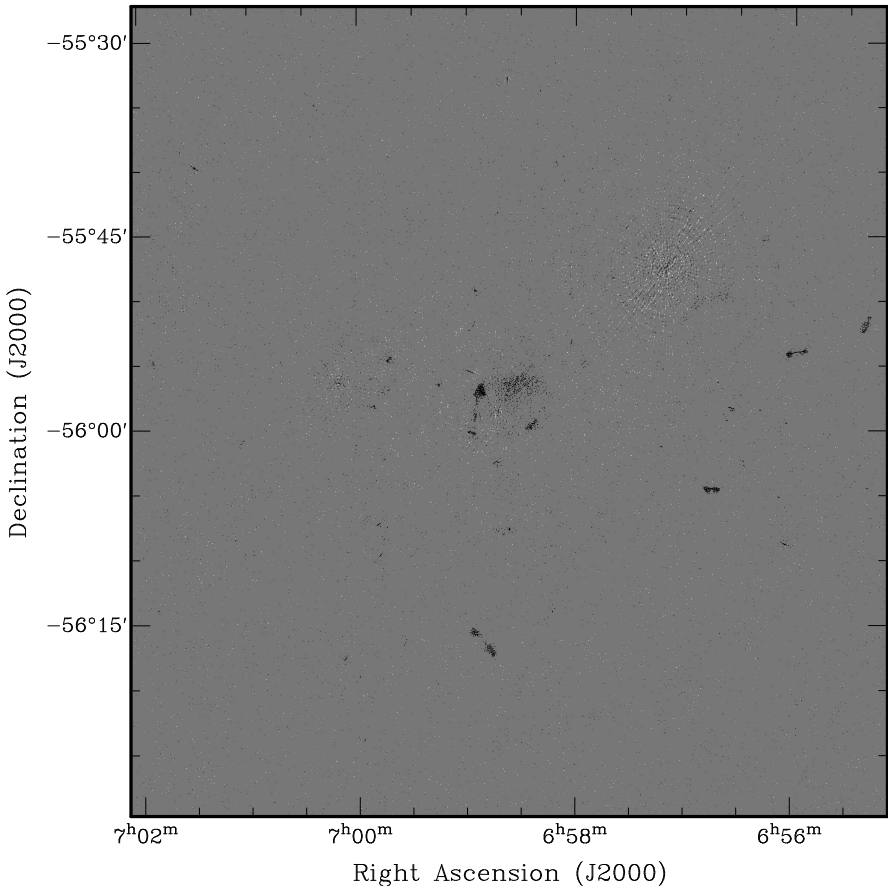

Figure 2.14: Screenshot of a clean component map generated using CLEAN task in MIRIAD. This clean component map is derived from dirty map and dirty beam in Fig 2.13.

have been placed even further out on a 3 km diameter circle to optimise solar imaging performance, and for the highest angular resolution imaging (Tingay et al., 2012). The list below summarises some of the basic properties of the MWA (referenced from MWA website)

Frequency range : 80 - 300 MHz
Number of receptors : 2048 dual polarisation dipoles
Number of antenna tiles :128
Number of baselines : 8128
Collecting area : Approx. 2000 sq. meters
Field of view : Approx. 15 - 50 deg. (200 - 2500 sq. deg.)
Instantaneous bandwidth : 30.72 MHz
Spectral resolution : 40 kHz
Temporal resolution : 0.5 seconds
Polarisation : Full Stokes (I, Q, U, V)
Array configuration : 50 antenna tiles within 100 meters, 62 antenna tiles between 100 and 750 meters, 16 antenna tiles at 1500 meters.

Signals from each dipole passes through a Low Noise Amplifier (LNA) and they are combined in a beamformer to produce the beam of the tile. The signals are then collected by 16 receiver units which are placed in the field, each of which services eight tiles. The receivers perform digitisation and coarse frequency channel selection of the incoming signals and the resulting signals are transmitted to the CSIRO data processing facility for further processing. The correlator subsystem converts the 1.28 MHz coarse frequency channels into channels with 10 kHz frequency resolution. Correlator boards then cross-multiply signals from all tiles to form visibility data and the data from correlator subsystem are sent to the CSIRO data processing facility for calibration and imaging.

In this thesis, we used the data from the Murchison Widefield Array Commissioning Survey (MWACS) to analyse the bullet cluster. The MWACS survey is a low frequency, low resolution survey of 4300 deg^2 taken during the commissioning of the MWA (Hurley-Walker et al., 2014) . The survey was conducted between 104-196 MHz spanning at an angular resolution of 3 arcmin spanning 21h $\leq$ RA $\leq$ 8 h and -55° $\leq$ Dec $\leq$ -10°. The baselines were 8 - 1530m in length and the MWA band encompasses 3072 10 KHz sub channels, derived from 24 1.28 MHz main channels with

[1]http://www.mwatelescope.org/telescope

Figure 2.15: Aerial photo of the central region on of the MWA. Source: MWA website[1].

flagging to the eight edge sub-channels of each main channel to account for aliasing. Observations were taken in two drift scans centred at -27 and -47h and combined to produce an image of the entire 4300 deg^2. A catalogue of approximately 14,000 compact radio sources was produced listing fluxes at 180 MHz for all sources. Further details of the catalogue production can be found in Hurley-Walker et al. (2014). The Bullet cluster falls under the Dec -47 strip and in this case the phase calibration was performed using Pictor-A: PKS 0519 -4546. A postage stamp region around the Bullet cluster was extracted from the Dec -47 drift scan at 180 MHz along with the flux density of the unresolved source which encompasses the entire cluster at 118 MHz.

§3. Bullet cluster

To begin with a number of galaxy clusters potentially hosting diffuse emission were considered as discussed in Appendix 1. However, we quickly narrowed the topic of the thesis to a detailed study of the Bullet cluster (1E 0657 -5558). The Bullet cluster is one of the hottest known galaxy clusters with an X-ray derived kinetic temperature of 17 keV (Tucker et al., 1998). This cluster is undergoing a merger event where a small subcluster is merging with a much larger subcluster. This merger event produces shock waves which can be seen in the X-ray spectrum primarily due to thermal Bremsstrahlung emission. The Chandra X-ray image reveals that the cluster hosts a prominent bow shock exiting the cluster core (see Fig 3.1). ROSAT and subsequent Chandra images Markevitch et al. (2002) confirms a smaller subcluster merging and moving away from the larger one. The remnant core of the smaller subcluster is at the centre of the shock cone and the gas of the smaller subcluster was stripped by ram pressure and the gas lags the subcluster galaxies (Markevitch et al., 2004). The temperature map study by Markevitch et al. (2002) confirms that the western X-ray brightness edge is a shock front. The Bullet cluster hosts a radio halo (Shimwell et al. (2014), Shimwell et al. (2015), Liang et al. (2000)), supporting the theory that the reacceleration of relativistic particles and magnetic field amplication caused by the turbulence of the merging clusters supply the energy to the radio halo. The Bullet cluster hosts one of the largest linear size halo at 1.4 GHz (Giovannini et al., 2009). The power of the radio halo in the Bullet cluster correlates directly to the X-ray luminosity thus relating thermal and non-thermal emissions (Giovannini et al., 2009). In addition to hosting a radio halo, Liang et al. (2000) suggested that a large radio relic is present in the peripheral region of this cluster. This was later confirmed in 1.1-3.1 GHz ATCA observations by Shimwell et al. (2015). Shimwell et al. (2015) suggests that the relic could be powered by the merger event in the cluster through the energy dissipated in shock waves. The bullet cluster is one of the few clusters which hosts both radio relic and halo.

The ATCA has been used to observe the Bullet cluster in the past and several hours of Bullet cluster data are available in the ATCA archive. Whilst some of these observations which span 1.344 to 8.7 GHz have been published in (Liang et al., 2000), comprehensive multiwavelength spectral study at such a wide range of radio

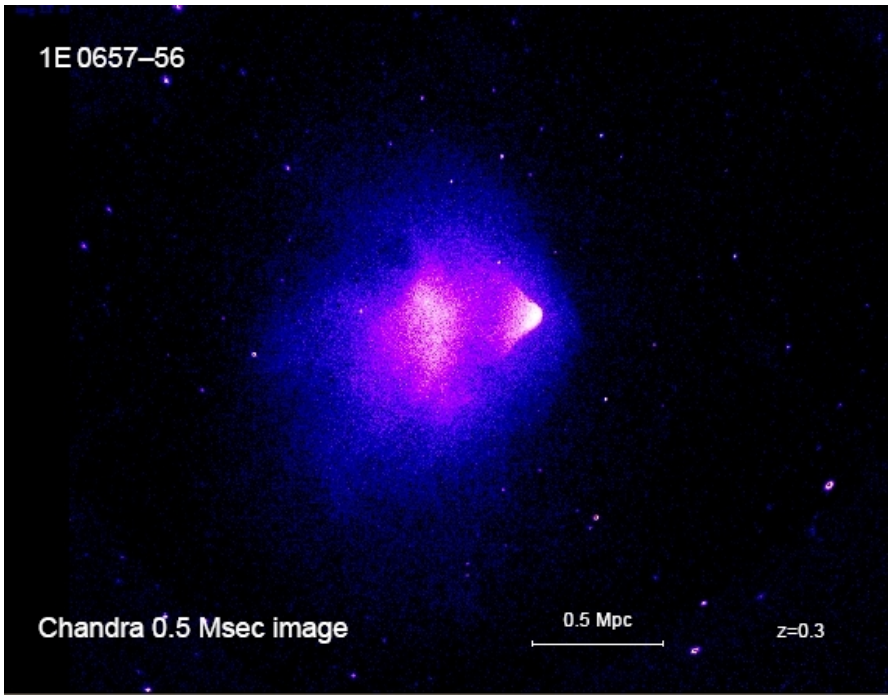

Figure 3.1: Chandra X-ray image of the bullet cluster. (Credit: NASA)

wavelengths was not performed before. These multifrequency datasets were taken from the archive and reduced to investigate the bullet cluster across a wide frequency range to derive flux density values of various sources seen in the region of the cluster. In addition, the Murchison Widefield Array Commissioning Survey (MWACS) data was used to examine the cluster at 118 MHz and 180 MHz (Hurley-Walker et al., 2014).

In this chapter, we discuss the data reduction results of the bullet cluster at different frequencies. In particular, we focus on the detection of diffuse emission at each frequency. This chapter also discusses the results of the radio relic in the Bullet cluster. In this thesis, we have categorised the radio relic into 2 regions - region A and region B. We present the spectral index results for region A and region B. Finally we discuss the polarisation results of the relic across the frequency spectrum from 1.344 GHz to 8.896 GHz.

§3.1. Data reduction for the Bullet cluster

This section covers the data reduction results by frequency. The datasets used for the reduction at all frequencies are listed in Table A.1. The intra-day datasets

Table 3.1: Dataset used for data reduction from the ATCA archive.

Date	Scan time (mins)	Array	Bandwidth (MHz)	Central frequency (MHz)	Project ID
1997-Jun-06	644	750A	128	1344	C649
1997-May-18	203	6B	128	1344	C649
1997-May-17	471	6B	128	1344	C649
1998-Jul-02	336	750E	128	1344	C649
1998-Jul-03	316	750E	128	1344	C649
1999-Nov-13	348.3	210	128	1384	C649
1997-Jun-06	616.5	750A	128	2184	C649
1999-Nov-13	348.6	210	128	2496	C649
1998-Jul-02	336	750E	128	2496	C649
1998-Jul-03	316	750E	128	2496	C649
2001-Jan-22	575.6	6C	128	2496	C923
1997-Nov-14	521.5	6C	128	4800	C649
1998-Jul-06	98.7	750E	128	4800	C649
1998-Jul-03	488	750E	128	4800	C649
2001-Jan-15	706.9	750C	128	4800	C923
2001-Jan-14	255.8	750C	128	4800	C923
2010-Jul-31	833.9	H168	2048	5500	C2037
2010-Jul-30	627.9	H168	2048	5500	C2037
2001-Jan-15	706.9	750C	128	6208	C923
2001-Jan-14	629.7	750C	128	6208	C923
1998-Jul-03	488	750E	128	8768	C649
1998-Jul-06	98.7	750E	128	8768	C649
1997-Nov-14	521.5	6C	128	8768	C649
1997-Nov-13	514	6C	128	8768	C649
1996-Dec-24	612.7	6C	128	8768	C649
1996-Dec-23	568	6C	128	8768	C649
1996-Dec-22	619.6	6C	128	8768	C649
1996-Dec-21	528.7	6C	128	8768	C649
1996-Dec-20	542.7	6C	128	8768	C649
1996-Dec-24	612.7	6C	128	8896	C649
1996-Dec-23	568	6C	128	8896	C649
1996-Dec-22	619.6	6C	128	8896	C649
1996-Dec-21	528.7	6C	128	8896	C649
1996-Dec-20	542.7	6C	128	8896	C649

were combined together before flagging and calibration and this step was done while reducing datasets at all frequencies. All the data sets from each observation day were flagged and calibrated individually. They were then combined together by frequency to produce the final set of images. Flux calibration was performed with respect to the unresolved source PKS B1934-638 and phase calibration was performed relative to PKS 0742-56 for data prior to 2010 and PKS 0537-441 there-after. Prior to the CABB upgrade (PreCABB), the observing bandwidth of the ATCA was 2×128 MHz and after the CABB upgrade, the bandwidth was increased to 2×2048 MHz (Wilson et al., 2011). CABB datasets for the bullet cluster were split into 8 subbands and were imaged separately. Since the central frequency of the CABB datasets used in this thesis was 5.5 GHz, the datasets were split into 4.604 GHz, 4.86 GHz, 5.116 GHz, 5.372 GHz, 5.628 GHz, 5.884 GHz, 6.14 GHz and 6.396 GHz sub-band images. PreCABB datasets were used for all data reduction at 1.344 GHz, 2.1 GHz, 2.4 GHz, 4.8 GHz, 6.2 GHz,8.768 GHz and 8.896 GHz. PreCABB datasets at 8.768 GHz and 8.896 GHz were combined and imaged together to measure the integrated flux density at a central frequency of 8.832 GHz. Overlapping CABB and PreCABB frequency data were kept separate for spectral index measurements.

§3.1.1. Bullet cluster at 1.344/1.384 GHz

The ATCA archival datasets for 1.344/1.384 GHz were taken from six days of observation and the total target scan time was 2318.3 minutes. All the calibrated target datasets for each day at 1.344/1.384 GHz were combined together to generate the final image by following standard ATCA Pre-CABB reduction steps. One image was with a taper FWHM=13 arcsec and the other with no taper (see Fig 3.2). The RMS noise value of the image with no taper was 31 μJy and for the image with a taper was 46 μJy.

§3.1.2. Bullet cluster at 2.1 GHz

The datasets used for reducing the bullet cluster at 2.1 GHz were from the observation done on 06 June 1997 under C649 project. The total scan time was 616.5 minutes. A taper of FWHM=30 arcsec was applied while generating the final image (see Fig 3.3). From this resultant image,only the flux density values for two sources (B and C in Figure 4.1) were used in spectral index measurements. The remaining sources were not fully detected and the flux density values of these sources were underestimated.

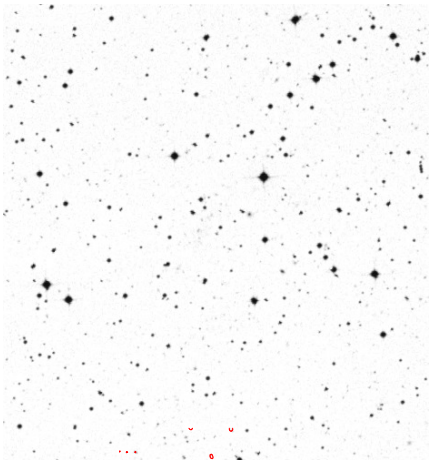

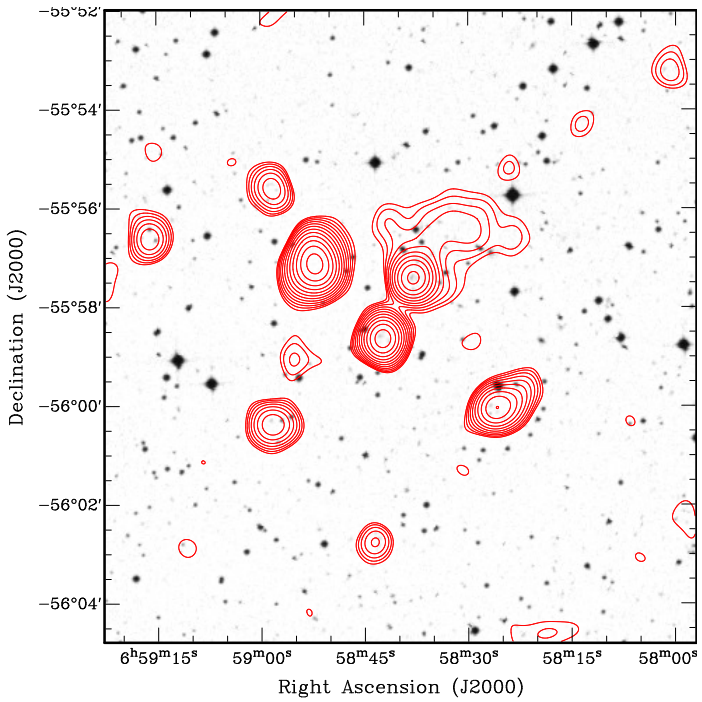

Figure 3.3: 2.1 GHz image with with FWHM=30 arcsec. The beam size for the image on the left is 38.07 × 33.66 arcsec, pa = -3.290 degrees and its RMS noise value is 175 μJy image.

combined together to generate the final image. The total target scan time was 2070.9 minutes. The diffuse emission was revealed more clearly in the tapered image with FWHM=30 arcsec (see Fig 3.5) The image with out a taper has the RMS noise of 57 μJy and the image with a taper has a RMS value of 41 μJy.

§3.1.5. Bullet cluster at 5.5 GHz - CABB

There were 2 days of observational data available for reducing the CABB dataset at the central frequency of 5.5 GHz. The total scan time of the target was 1461.8 minutes. There were 2 pointings for each day of observation and hence 4 datasets were reduced and combined to generate the final set of images. The pointing centres were RA: 06:58:30.00 DEC: -55:57:00.00 and RA: 06:58:20.00 DEC: -55:56:00.00. Since the bandwidth of CABB data is 2048 MHz, the datasets were split into 256 MHz sub-band images of 4.604 GHz, 4.86 GHz, 5.116 GHz, 5.372 GHz, 5.628 GHz, 5.884 GHz, 6.14 GHz and 6.396 GHz (see Fig 3.6 and 3.7).

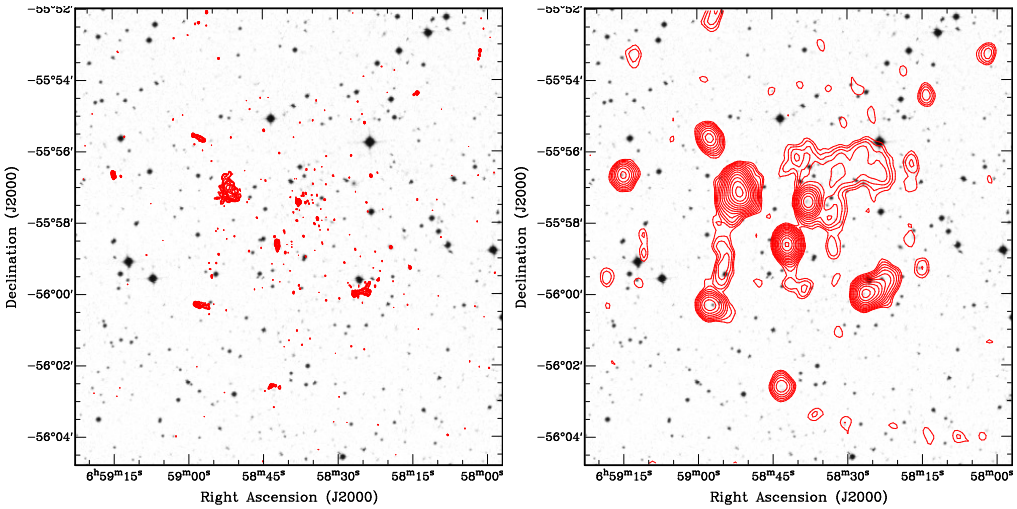

Figure 3.4: The image on the left side is the combined 2.4 GHz image that was generated with no taper and the image on the right is an image with FWHM=15 arcsec. The beam size for the image on the left is 4.396 × 2.828 arcsec, pa = 2.424 degrees and its RMS value is 42 μJy. The image on the right with FWHM=15 arcsec has a beam size of 27.61 × 22.05 arcsec, pa = 2.338 degrees and the RMS value is 66 μJy. Both images revealed the presence of diffuse emission in the cluster at 2.4 GHz. The image with no taper revealed the presence of relic in the periphery. The tapered image revealed the presence of both radio halo and radio relic.

.

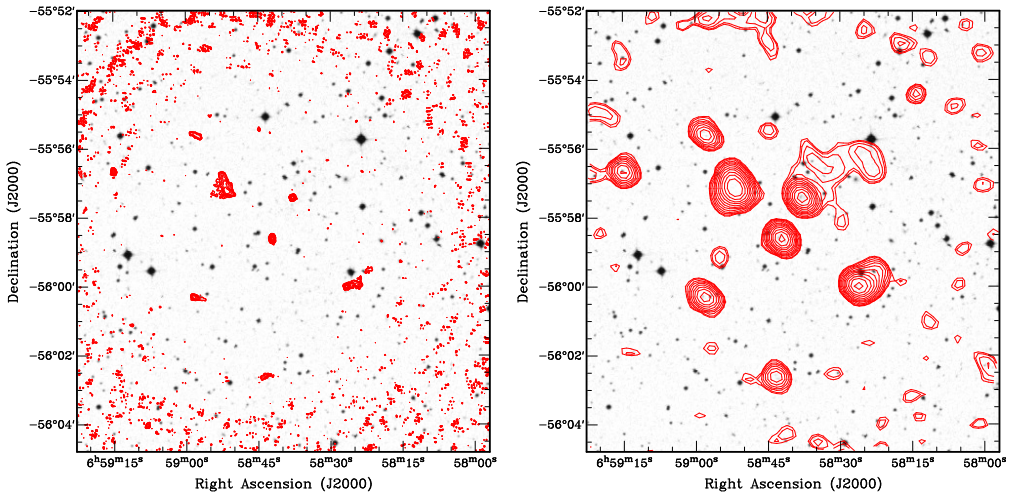

Figure 3.5: The image on the left side is the combined 4.8 GHz image generated with no taper and the image on the right is the combined image with with FWHM=30 arcsec. The beam size for the image on the left is 5.00 × 5.00 arcsec, pa = 0 degrees and its RMS value is 57 μJy. The image on the right with a taper of FWHM=30 arcsec has a beam size of 31.51 × 25.78 arcsec, pa = 42.46 degrees and RMS value is 41 μJy.

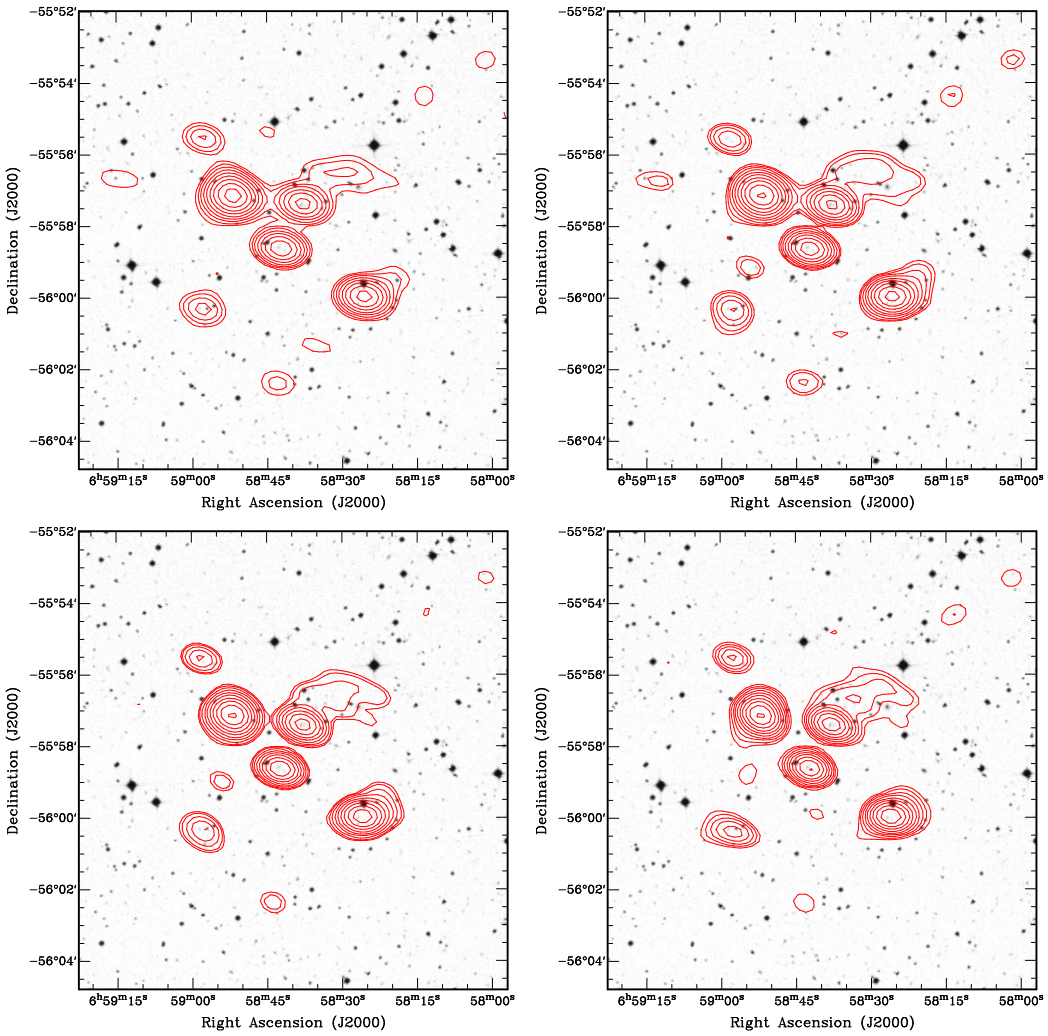

Figure 3.6: The image on top left is the 4.604 GHz image with no taper. The beam size for the image is 54.31 × 37.72 arcsec, pa = 75.64 ± 2 degrees and its RMS value is 203 μJy. The The image on the top right is the 4.86 GHz image with no taper. Beam size is 51.41 × 35.86 arcsec, pa = 75.93 ± 2 degrees and the RMS value is 140 μJy. The image on the bottom left is 5.116 GHz image with no taper. Beam size is 48.48 × 34.07 arcsec, pa=75.53 degrees and its RMS value is 120 μJy. The image on the bottom right is 5.372 GHz image with no taper. Beam size is 45.9 × 32.52 arcsec, pa = 75.23 degrees and its RMS value is 153 μJy.

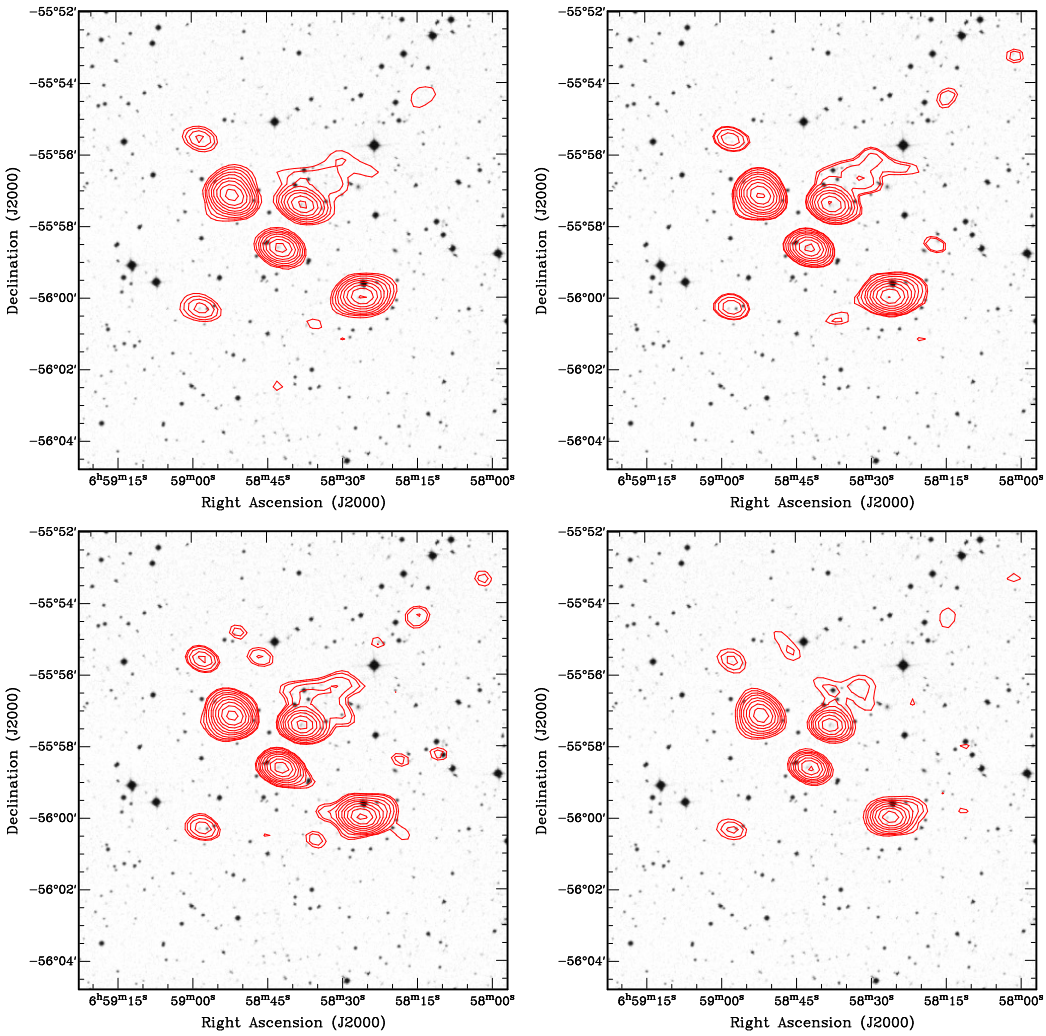

Figure 3.7: The image on top left is the 5.628 GHz image with no taper. The beam size for the image is 43.6 × 31.09 arcsec, pa = 74.78 ± 2 degrees and its RMS value is 126 μJy. The The image on the top right is the 5.884 GHz image with no taper. Beam size is 41.72 × 29.88 arcsec, pa = 74.46 ± 2 degrees and the RMS value is 122 μJy. The image on the bottom left is 6.14 GHz image with no taper. Beam size is 39.81 × 28.51 arcsec, pa=74.61 degrees and its RMS value is 100 μJy. The image on the bottom right is 6.396 GHz image with no taper. Beam size is 38.6 × 27.78 arcsec, pa = 73.98 degrees and its RMS value is 117 μJy.

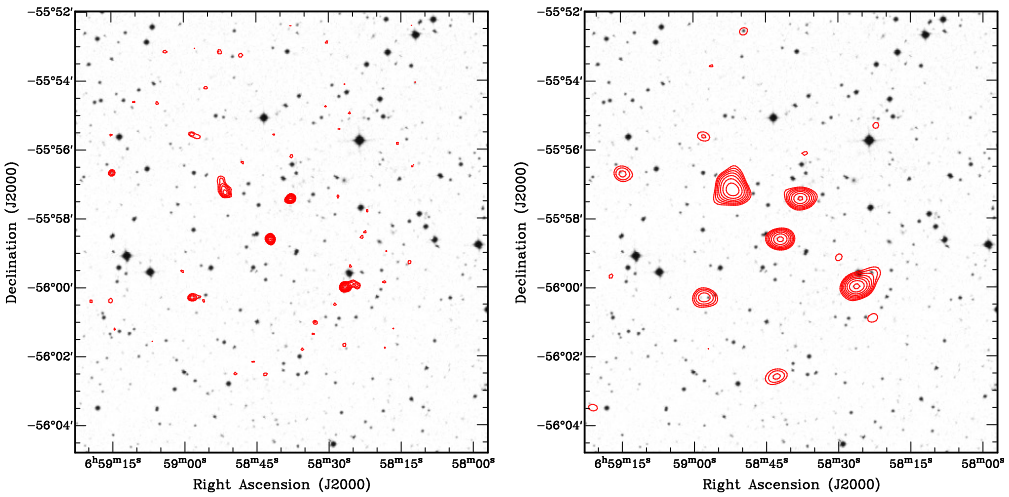

Figure 3.8: Image on the left is 6.208 GHz image with no taper. The beam size for the image is 9.279 × 8.254 arcsec, pa = -76.14 degrees and its RMS value is 127 μJy image. Image on the right is 6.208 GHz image with a taper of FWHM=30 arcsec applied. The beam size is 29.62 × 23.38 arcsec , pa=-84.96 degrees and the RMS value is 269 μJy.

§3.1.6. Bullet cluster at 6.208 GHz - PreCABB

The archive had 2 days of observational data. The total scan time of the target was 1336.6 minutes. The halo component of the diffuse emission was not detected with this dataset (see Fig 3.8). The flux densities for the sources were estimated using tapered and untapered images. The point source values were mainly taken from untapered image and extended source (region A) values were taken from the tapered image of FWHM=30 arcsec. The RMS value for untapered image is 127 μJy and the taper image has a RMS of 269 μJy.

§3.1.7. Bullet cluster at 8.768 GHz - PreCABB

At this frequency, 9 days of observational data was available in the archive. The total scan time was 4493.7 minutes. There were different pointings in these datasets and we faced issues in combining them all into one final image. Therefore, the data observed in Dec 1996 were imaged separately from the rest. In the final combined image of the Dec 1996 observations, diffuse emission was detected when a taper of FWHM=60 arcsec was applied and when data from baselines with antenna 6 were excluded (see Fig 3.9). This is similar to the finding by Liang et al. (2000) using the same dataset at 8.768 GHz. Datasets outside Dec 1996 observations for 8.768 GHz

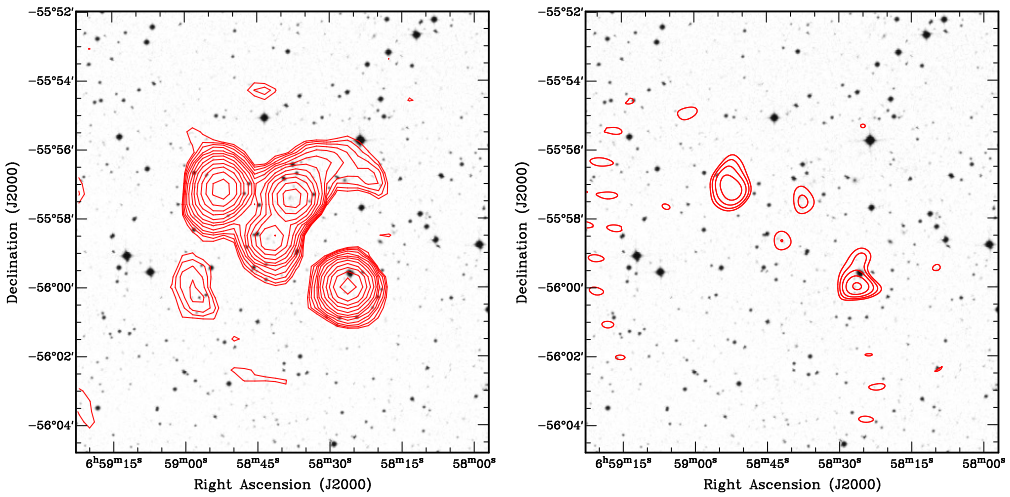

Figure 3.9: The image on the left is the combined 8.768 GHz image generated with a taper of FWHM=60 arcsec applied on the dataset observed from Dec 20,1996 to Dec 24, 1996 and the image on the right is the combined image excluding Dec 1996 datasets with FWHM=60 arcsec applied to it. The beam size for the image on the left is 55.64 × 55.22 arcsec, pa = -10.52 degrees and its RMS value is 17 μJy. The image on the right with a taper of FWHM=60 arcsec has a beam size of 51.94 × 51.01 arcsec, pa = -72.26 degrees and RMS value is 568 μJy. The image on the left reveals the presence of diffuse emission as shown in Liang et al. (2000).

were reduced and combined together with a taper of FWHM=60 arcsec (see Fig 3.9 and the resultant image did not detect any diffuse emission. The pointing center for Dec 1996 dataset was RA: 06:58:32.70 DEC: -56:12:19.00 and for the other datasets was RA: 06:58:42.20 DEC: -55:58:39.00. The RMS value for image generated using Dec 1996 dataset is 17 μJy and the RMS value for the other image is 568 μJy.

§3.1.8. Bullet cluster at 8.896 GHz - PreCABB

The archive had data from 5 days of observation and the total scan time of the target was 2871.7 minutes. Similar to 8.7 GHz data, the datasets were reduced and imaged with a taper of FWHM=60 arcsec (see Fig 3.10). The RMS value of the image is 16 μJy.

§3.2. Radio relic results

This section discusses the measurements made for deriving the integrated flux density and spectral index values for the radio relic. We also discuss the results of polarisation

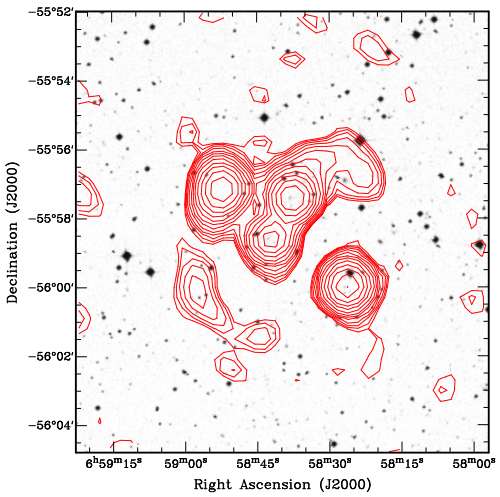

Figure 3.10: Combined 8.896 GHz image generated with a taper of FWHM=60 arcsec applied on the dataset observed from Dec 20,1996 to Dec 24, 1996. The beam size for the image is 56.01 × 55.42 arcsec, pa = -6.299 degrees and its RMS value is 16 μJy. This image revealed the presence of diffuse emission at 8.896 GHz as shown in Liang et al. (2000).

detection across different frequencies for the radio relic. As mentioned in the earlier chapters, radio relics are generally found in the cluster periphery and are polarised. In figure 3.11, diffuse emission was detected at the eastern cluster periphery and also in the cluster center at 1.344 GHz. The diffuse emission at the cluster periphery is connected to a faint linear diffuse structure which extends southwards. In this thesis, the bulb like diffuse emission was classified as region A and the linear diffuse structure as region B. Regions A and B at the cluster periphery were considered to a part of the radio relic (Shimwell et al., 2015). Spectral index measurements for these regions were made and polarisation images were generated at different frequencies. As shown in the images in the previous section, the bulb like diffuse structure was detected at all frequencies starting from 1.344 GHz to 8.896 GHz. In order to calculate the spectral index, the flux density values were calculated for all sources using the DUCHAMP software (Whiting, 2012).

§3.2.1. Flux density values

The integrated flux density for calculating spectral indices was measured with the aid of the software Duchamp. Duchamp (Whiting (2012)) is a source identification software that detects the source boundaries and its statistics. It receives 2 inputs from the user which are, an image to be processed and a parameter file that drives

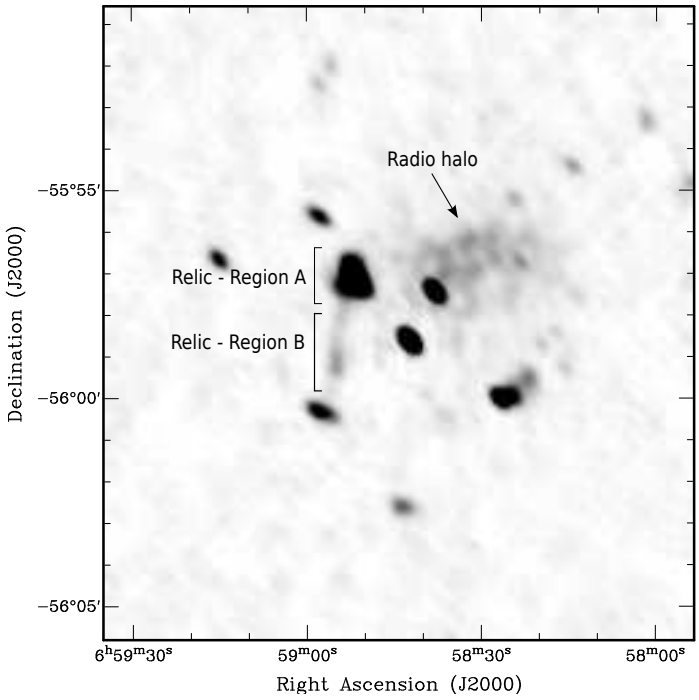

Figure 3.11: Radio relic and halo in 1.344 GHz image. The bulb like diffuse emission in the relic was classified as region A and the tail structure below was classified as region B.

the processing both in choosing different processing algorithms and in tuning many aspects of the searching and output. The output of Duchamp is an annotation file used to graphically identify the sources and a display of output statistics which includes the integrated flux density value for each source. Figure 3.12 shows the flowchart of Duchamp processing. The input parameters that were passed for each run were based on the individual images. The 2 input parameters that were passed for every Duchamp run were SNRCUT and GROWTHCUT. Parameter SNRCUT is the value for signal to noise ratio threshold in multiples of the RMS noise above the mean. Parameter GROWTHCUT is used to detect the emission associated with a source that could be just below the detection threshold. These parameters were used on a trial and error basis to get the matching source boundaries and their flux density values. Manual verification was done to validate the source boundaries. The GROWTHCUT and SNRCUT parameters were decided manually based on the type of the target source, to ensure that Duchamp determines a reasonable source boundary. For all flux density calculations using Duchamp, we have used a minimum threshold of SNRCUT = 3. In some cases, manual measurement of flux density was required because Duchamp could not separate multiple sources. For example,

Duchamp could not separate the relic from other sources at 8.896 GHz in figure 3.10. So the integrated flux density value of the relic was manually measured using kvis at 8.8 GHz.

§3.2.2. Spectral index maps for region A and region B

This sub section discusses the spectral index values calculated from the flux densities across different frequencies for region A and region B. The spectral indices were calculated using the flux values measured in observed frame. We expect the emission to follow a power law $S \propto \nu^{\alpha}$, where S is the flux, ν is the frequency, and α is the spectral index. We have used a non linear fit to determine spectral index values. All the spectral index plots and fits were done by Dr. Siamak Dehghan. The spectral index value is the characteristic that depends on age of the electron population and the underlying mechanism supplying energy to the electrons.

In addition, Sydney University Molonglo Sky Survey (SUMSS) data was used to derive the flux density values for the individual sources at 843 MHz. They were also included in the calculation for spectral index. SUMMS values were derived from the bullet cluster image downloaded from SUMSS Postage Stamp Server. The flux density values were extracted for region A at frequencies 843 MHz (from SUMSS), 1.344 GHz, 2.496 GHz, 4.604 GHz, 4.8 GHz, 4.86 GHz, 5.116 GHz, 5.372 GHz, 5.628 GHz, 5.884 GHz, 6.14 GHz, 6.208 GHz, 6.396 GHz and 8.832 GHz. Region B flux density values were derived from the images at frequencies 843 MHz (from SUMSS), 1.344 GHz, 2.496 GHz and 4.8 GHz. The 8.832 GHz image did not detect region B and hence the flux density value at this frequency was considered a lower limit value. Flux density measurements from Shimwell et al. (2015) were also included for region A and region B in the spectral fit analysis at frequencies at 1.43 GHz, 1.72 GHz, 2.01 GHz, 2.3 GHz, 2.59 GHz, 2.88 GHz. The spectral index value for region A used to extrapolate the MWA flux density, was calculated only using low frequency measurements (0.843 GHz to 2.88 GHz) due to spectral bending at frequencies between 2.88 GHz to 4.6 GHz. The slope for region B was calculated using all points except 8.832 GHz as it was only partially detected and it was assumed to be a lower limit. The values of flux density at each frequency for all the sources including region A and B are listed in the Table 4.1 in next chapter. In this table, source A refers to region A of the relic and source J refers to region B of the relic.

The spectral index plots for region A and region B are given in Fig 3.13. The

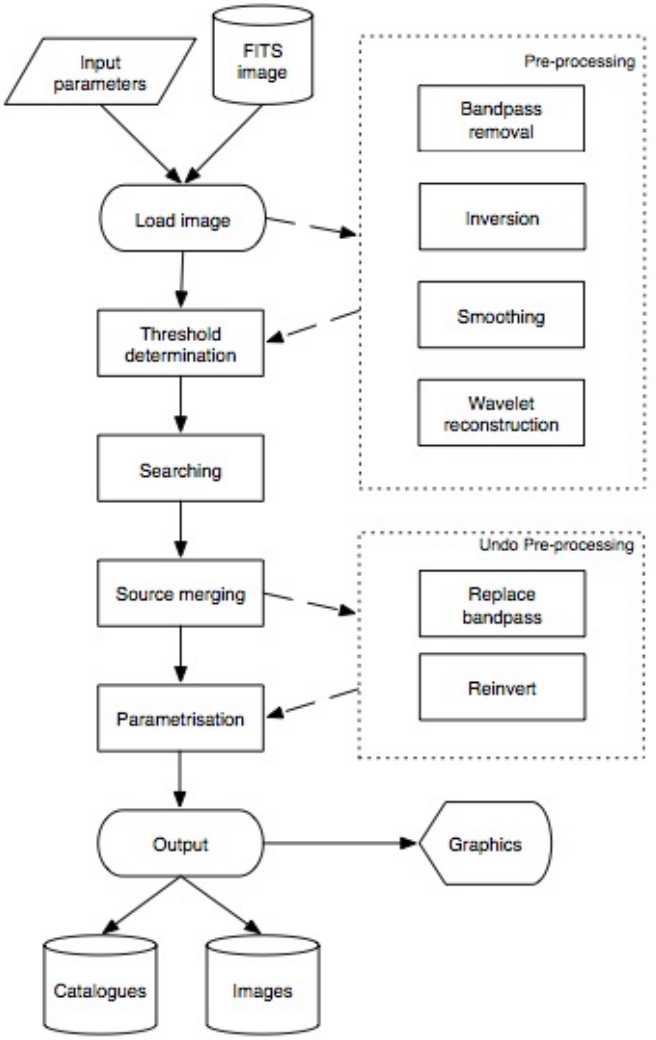

Figure 3.12: Above flowchart indicates the key steps in processing in Duchamp (Whiting, 2012).

spectral index plots in Fig 3.13 also includes the measurements from Shimwell et al. (2015). The spectral index values are calculated using the points marked in blue. The spectral index value for region A was -1.08 ± 0.02 and for Region B was -1.74 ± 0.08. These spectral index values were used to extrapolate the MWA flux density for region A and region B. The details of extrapolation to MWA frequencies are discussed in the forthcoming chapter.

§3.2.3. Polarisation images

The linear polarisation P is defined as $P = Q + iU$. The polarisation angle and intensity can be calculated from $\chi = \frac{1}{2}\arctan\left(\frac{U}{Q}\right)$ and $|P| = \sqrt{Q^2 + U^2}$ respectively. This subsection discusses the polarisation analysis done on region A and region B at different frequencies. Common Astronomy Software Applications package (CASA)(McMullin et al., 2007) was used as the image viewing tool for viewing polarisation angle vectors on polarisation intensity images. We rotated the polarisation angle by 90 degrees to show the magnetic field direction of the source (in the plane of the sky). Polarisation images were generated for 1.344 GHz, 2.496 GHz, 4.8 GHz, 8.768 GHz and 8.896 GHz. All these datasets were PreCABB. Polarisation images were generated for stokes Q and stokes U. Task IMPOL in MIRIAD was used to generate the polarisation intensity and polarisation angle images combining stokes Q and U. The polarisation images were masked at 3 times the RMS noise of the Q and U images.

There was polarisation detection for region A at all frequencies except at 1.344 GHz (see Fig 3.14). A taper of FWHM=13 arcsec was applied to generate 1.344 GHz polarisation intensity image. The generated images showed polarisation for region B only at 2.496 GHz. Figure 3.15 shows polarisation intensity and angle vectors at 2.4 GHz generated with a taper of FWHM=10 arcsec and FWHM=30 arcsec. As can be see in Figures 3.16, 3.17 and 3.18 the polarisation for region A was detected at high frequencies as well except at 6.208 GHz, 6.396 GHz where polarisation was detected only partially. In addition, polarised flux density was also detected at 8.7 GHz and 8.8 GHz frequencies in region A . Figure 3.19 shows the combined 8.7 GHz and 8.8 GHz polarisation intensity and vector maps.

Fractional polarisation for each frequency was calculated by dividing the polarised flux density with its corresponding Stokes I flux density. The polarisation percentage values for region A of the relic are listed in table 3.2. The fractional polarisation increased with frequency for region A except at 6.208 GHz and 6.396 GHz. Also

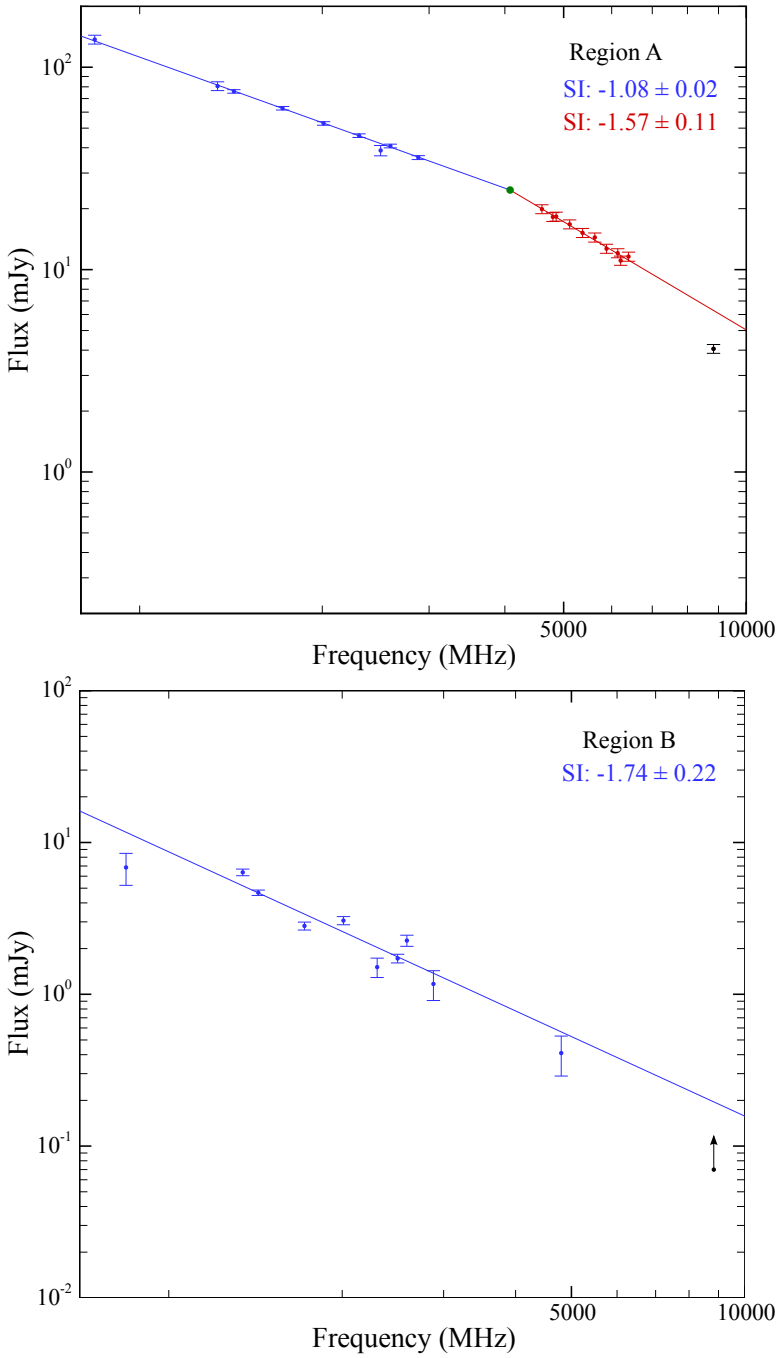

Figure 3.13: Spectral index plots for region A and region B of the relic. Regions A and B are indicated in Fig 3.11. The points marked in blue were used for spectral index calculation and extrapolation to MWA frequencies. The red points in region A plot were high frequency points from 4.604 GHz to 6.396 GHz and they were not used for extrapolation to MWA frequencies. High frequency 8.832 GHz measurement for region A was an outlier and hence was ignored in spectral index measurements. Also please note that 8.8 GHz point was a lower limit value in region B and hence was indicated by the upward facing arrow.

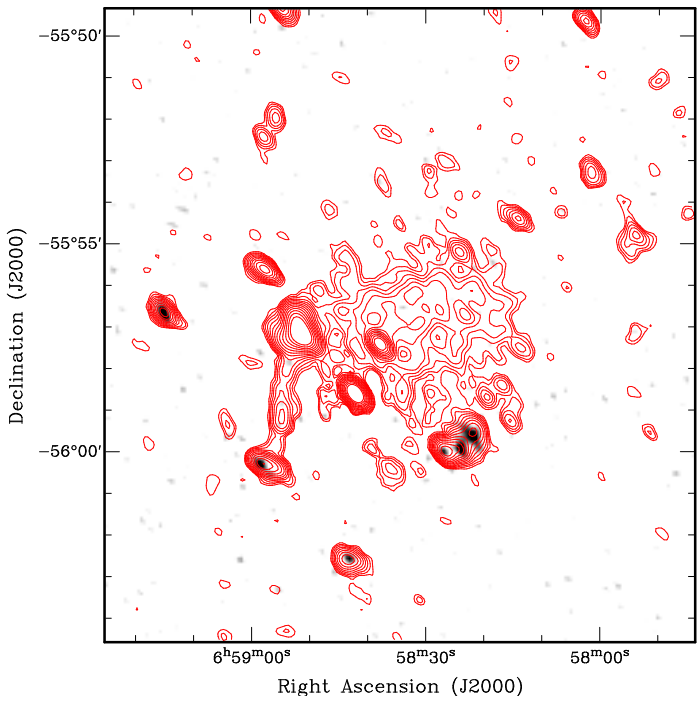

Figure 3.14: Stokes Q and U polarisation intensity map of the bullet cluster at 1.344 GHz with FWHM=13 arcsec overlaid with stokes I contours in red at 1.344 GHz. The image shows no indication of polarisation at region A or region B marked in Figure 3.11. There was polarisation detection only for point sources.

there was a difference in the polarisation percentage of CABB datasets with respect to the equivalent 4.8 GHz Pre-CABB datasets. This could be due to the beam depolarisation of CABB images due to the low angular resolution of its images. Also polarisation was only partially detected at 6.14 GHz and 6.396 GHz thereby making the polarisation percentage lower limit values at these frequencies. In the case of region B, polarisation was detected only at 2.4 GHz and the polarisation flux density was 0.27 mJy and its corresponding stokes I flux density was 1.722 mJy. Fractional polarisation percent for region B at 2.4 GHz was 15.68%.

§3.3. Discussion

In this section, we discuss the spectral index and polarisation results for the radio relic. We also briefly explore the underlying mechanism behind this diffuse emission.

The spectral index for region A from 0.843 GHz to 2.496 GHz was -1.08±0.02 and this agrees with the result from Shimwell et al. (2015). The spectral index of region A from 4.608 GHz to 6.396 GHz was -1.57 ± 0.11. The wide bandwidth measurements

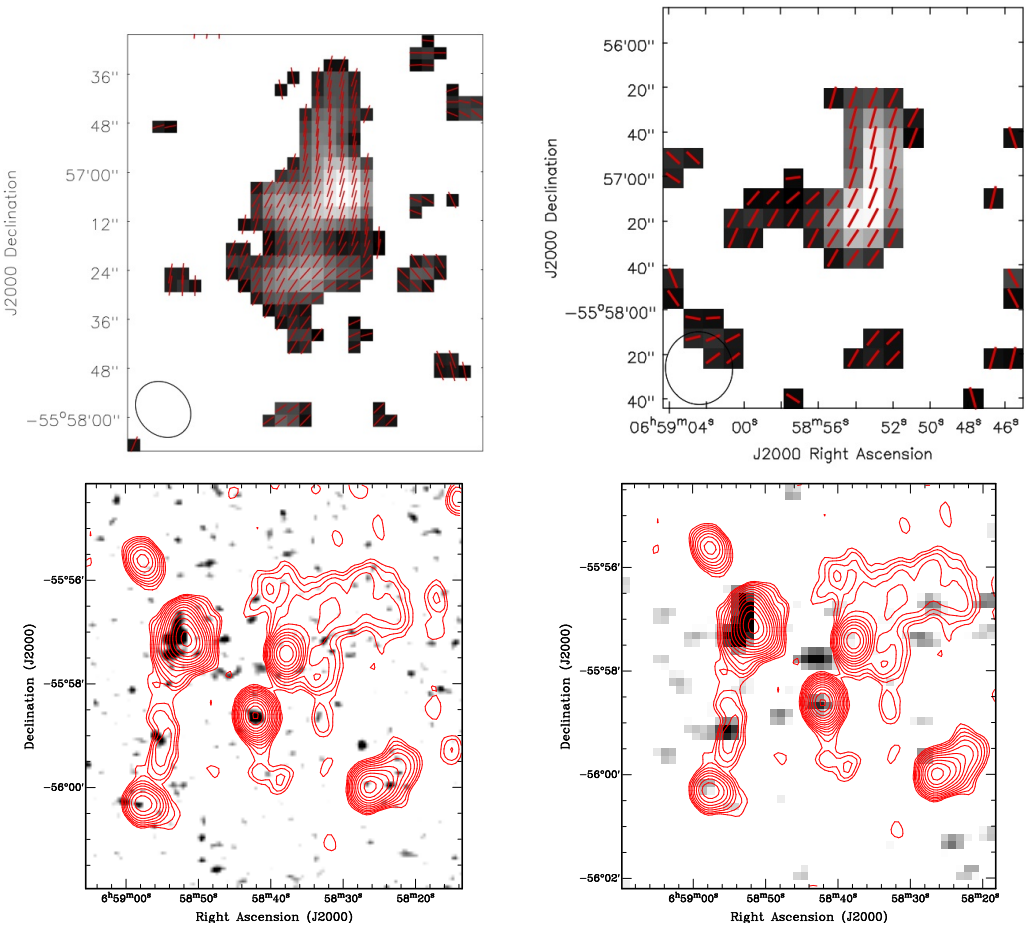

Figure 3.15: The top left image is the zoomed in 2.4 GHz stokes Q and U FWHM=10 arcsec polarisation intensity and vector map of the relic with the polarisation angle rotated by 90 degrees and top right is the zoomed in 2.4 GHz stokes Q and U FWHM=30 arcsec polarisation image of the relic with the rotated polarisation vectors. Bottom images are 2.4 GHz stokes Q and U polarisation images of the cluster with a taper of FWHM=10 arcsec on left and FWHM=30 arcsec on right overlaid with 2.4 GHz Stokes I contours. Please note that the colour scale goes from black to white in the top zoomed in images of the relic. For the images in the bottom row, colour scale goes from white to black.

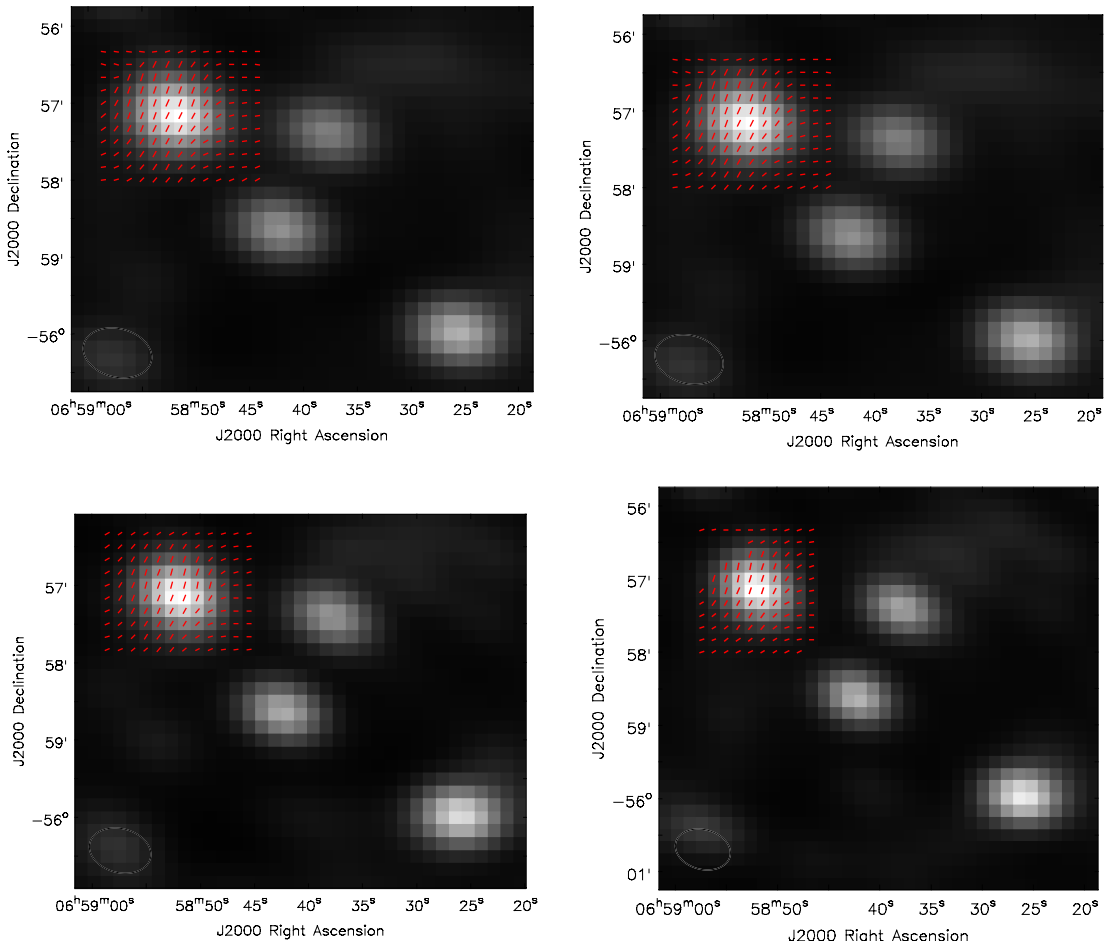

Figure 3.16: Above images are CABB polarisation subband Stokes I images overlaid with rotated polarisation position angle of region A in red. The image in the top left corner is at 4.604 GHz and the image in the top right is at 4.860 GHz. The image in the bottom left is at 5.116 GHz and the image in the bottom right is at 5.372 GHz. Please note that the colour scale goes from black to white for all of these images.

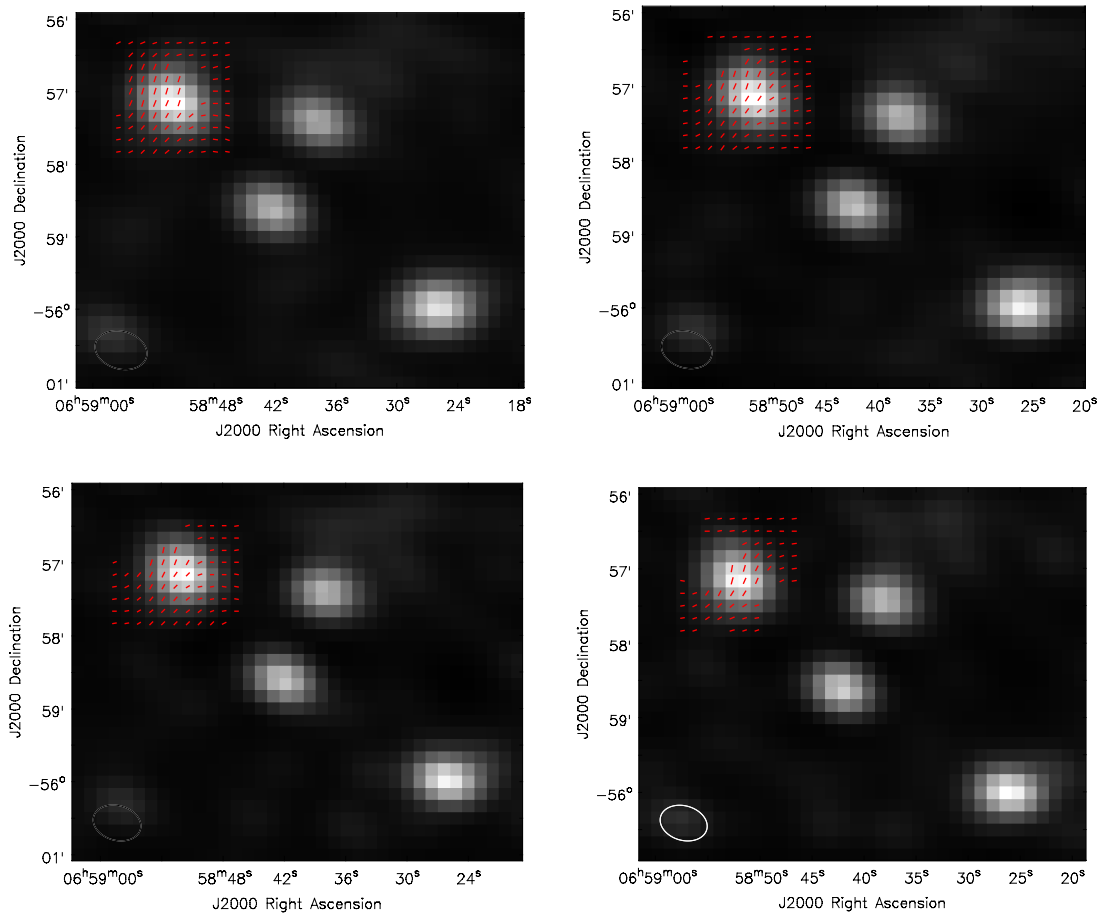

Figure 3.17: Above images are CABB polarisation subband Stokes I images overlaid with rotated polarisation position angle of region A in red. The image in the top left corner is at 5.628 GHz and the image in the top right is at 5.884 GHz. The image in the bottom left is at 6.14 GHz and the image in the bottom right is at 6.396 GHz. Polarisation is only partially detected at 6.14 GHz and 6.396 GHz. Please note that the colour scale goes from black to white for all of these images.

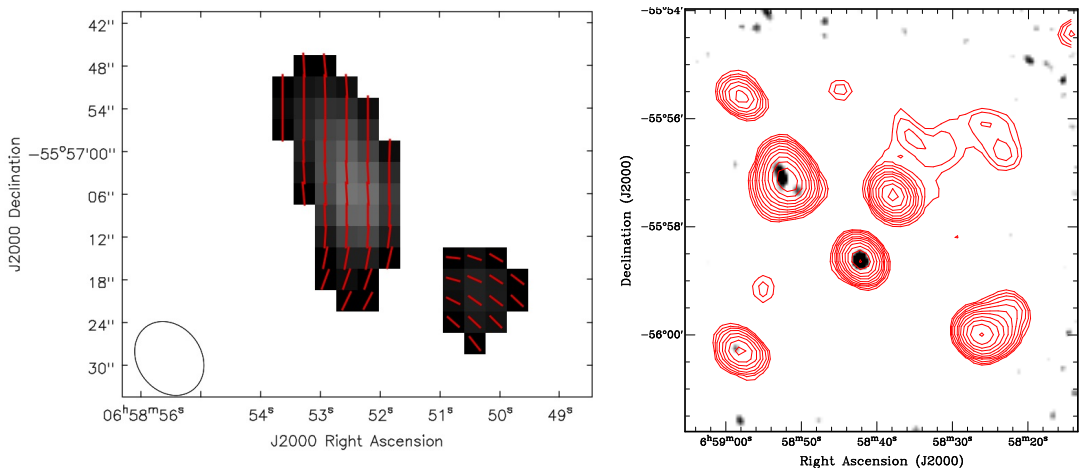

Figure 3.18: The image on the left is 4.8 GHz stokes Q and U polarisation intensity and rotated polarisation angle of the relic with a taper of FWHM=10 arcsec. The image on the right is stokes Q and U polarisation intensity map of the bullet cluster at 4.8 GHz with FWHM=10 arcsec overlaid with stokes I contours in red at 4.8 GHz. Please note that the colour scale goes from black to white in the left side zoomed in image of the relic. For the image in the right side, colour scale goes from white to black.

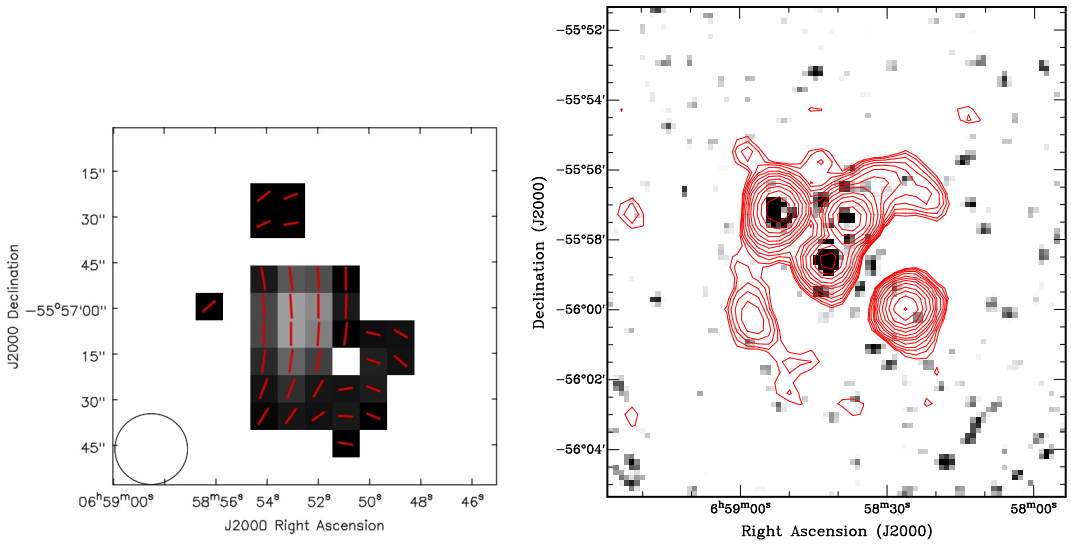

Figure 3.19: The image on the left is combined 8.768 and 8.896 GHz stokes Q and U polarisation intensity and polarisation angle vectors with a taper of FWHM=30 arcsec. The image on the right is stokes Q and U polarisation intensity map of the bullet cluster at 8.768 GHz and 8.896 GHz overlaid with its corresponding stokes I contours in red. Please note that the colour scale goes from black to white in the left side zoomed in image of the relic. For the image in the right side, colour scale goes from white to black.

Table 3.2: Polarisation percentage by frequency for region A of the relic. The values at 6.14 GHz and 6.396 GHz are lower limits because polarisation is only partially detected at these frequency sub-bands.

Frequency (GHz)	Stokes I flux density (mJy)	Polarisation flux density (mJy)	Fractional polarisation (in %)
2.496	38.78	2.48	6.4
4.604	19.9	1.5	7.54
4.8	18.204	2.03	11.15
4.860	18.29	1.37	7.5
5.116	16.75	1.45	8.68
5.372	15.19	1.38	9.1
5.628	14.42	1.42	9.9
5.884	12.69	1.5	11.78
6.14	12.06	1.25	10.4
6.396	11.6	0.838	7.22
8.8	4.061	0.58	14.28

from 0.843 GHz to 6.396 GHz indicates spectral bending between 2.88 GHz and 4.604 GHz. Using the spectral indices of these bands, the break frequency was estimated as 4.532 GHz. In addition, region A was polarised and the polarisation percentage increased with frequency as required for a radio relic. Polarisation was detected at all frequencies from 2.496 GHz to 8.896 GHz (see Table 3.2). The spectral index in region B was -1.74 $\pm$ 0.22 which agreed with Shimwell et al. (2015). In case of region B, polarisation was detected only at 2.4 GHz and its fractional polarisation percent at 2.4 GHz was 15.68 %. Since region B was fainter, there was not enough sensitivity to detect polarised flux density at high frequencies. There was no spectral bending observed for region B.

The diffuse bulb like structure called region A in figure 3.11 could potentially be a radio relic or a dead radio galaxy. The location of region A is consistent with theory that states that relics are generally located in cluster periphery and are powered by the shocks in the region. Region A has high surface brightness and was detected across a wide band of frequencies from 0.843 GHz to 8.896 GHz. The spectral index of radio relics could vary from -0.9 to -2.8 (Feretti et al., 2012), thus our spectral index values are not unusual for a relic. However, the property of spectral bending is a characteristic of a radio galaxy. Since this source is bright, it could be a recently dead radio galaxy. As discussed in Shimwell et al. (2015), pre-existing population of relativistic electrons could be remnants of a dead radio galaxy. These electrons could be reaccelerated by the shock of the merger event causing diffuse

synchrotron emission. As discussed in Shimwell et al. (2015), the region B part of the relic coincides exactly with the X-ray sharp edge as seen in the Chandra X-ray image. The tail of the radio relic (region B) is oriented perpendicular to the X-ray edge indicating that the shock generated due to merger event reaccelerates the seed electrons. There is a possibility that seed electrons for region B could also be supplied by the dead radio galaxy due to the physical connection between region A and region B. The polarisation angle from the images indicated that the electrons could be moving from region A towards region B. This suggests that the remnants of the dead radio galaxy could have polluted both regions in the periphery of the cluster thereby supplying seed electrons for shock acceleration in the relic (Shimwell et al., 2015).

§4. The Radio halo in the Bullet cluster

In this chapter, we focus on the radio halo in the bullet cluster. The Bullet cluster hosts one of the largest linear size halo at 1.4 GHz (Giovannini et al., 2009). The power of the radio halo in the Bullet cluster correlates directly with the X-ray luminosity thus relating thermal and non-thermal emissions (Giovannini et al., 2009). We have used the ATCA archival data to calculate the spectral index of the individual sources in the Bullet cluster across the frequency range of 1.344 GHz to 8.896 GHz. After deriving the spectral indices from the ATCA data, each spectral index was used to extrapolate the flux density of individual sources at lower MWA frequencies (118 MHz and 180 MHz) in order to derive the flux density of the halo at MWA frequencies. The total extrapolated flux density of individual sources was subtracted from the total measured flux density of the cluster at MWA frequencies. This was done due to the lower angular resolution of the MWA image which made the individual sources inseparable from the diffuse relic and halo emission in the cluster.

§4.1. Bullet cluster sources and its spectral indices

Figure 4.1 shows the MWA contours at 180 MHz and 3' resolution overlaid on a 1344 MHz 4" resolution ATCA image. Due to lower resolution, the Bullet cluster was detected as a single unresolved source by MWACS. As can be seen in figure 4.1, the MWA data combines several sources including the halo, relic, several head-tail galaxies and bright point sources. In order to obtain an estimate of the halo flux density in the MWA data, the higher resolution ATCA images were used to derive the spectral index of all contaminating sources marked by red outlines in figure 4.1. These spectral indices were then used to extrapolate the flux density of these contaminating sources at 118 and 180 MHz. The contaminating sources were labeled A to N in figure 4.1.

The reason for not including the points in red for source A was due to spectral bending at higher frequency points and as a result extrapolation was possible only using low frequency points from 0.843 GHz to 2.88 GHz. This also included the measurements from Shimwell et al. (2015). Source B was not fully detected at the points marked in black and as a result these points were not considered for extrapolation. The high

frequency CABB measurements detected only the core of source B and therefore the flux density values were underestimated. Source F was polluted by diffuse emission due to its proximity to the halo. As a result the low resolution images of CABB datasets and the 8.8 GHz dataset were providing an overestimate of the flux density for source F. These points were ignored for spectral index extrapolation to MWA frequencies. Source E undergoes spectral bending between 3 to 4.6 GHz and this agrees with Liang et al. (2001). A polynomial fit was used for sources C,D and L as these were experiencing spectral curving. The measurements for these sources did not fit in a straight power law model. A polynomial fit was used for these sources to avoid overestimating the flux density at MWA frequencies. In addition, images at 8.8 GHz did not fully detect sources B, H and J and therefore flux density values for these sources at 8.8 GHz were taken to be lower limits and were not included in spectral index measurements.

Table 4.1 lists all the flux density values by frequency for sources A to J and these values were used to plot spectral maps for the individual point sources from A to J. Table 4.2 lists the corresponding total error values on the integrated flux density. In addition to the bright sources A to J, Figure 4.1 also contains 4 weak point sources seen inside the MWA contours which are labeled from K to N . The flux density for sources K to N are listed in table 4.3. Since the sources K,L,M,N are weak, they were detected at fewer frequencies when compared to the rest. Since source K was not detected in any frequency except 1.344 GHz and also since there were no available published values for the source, determining the spectral index was impossible for K and hence a standard spectral index of -0.7 was assumed. A set of low frequency values for sources A, E, F, G, J, L, M and N were published in Shimwell et al. (2014) and they were used alongside our values to derive the spectral index and to also compare the results.The spectral index plots for each source from A to N are displayed in figures 4.2 and 4.3. The points marked in blue were used for spectral index calculation and extrapolation to MWA frequencies. The points in black were not used in extrapolation to MWA frequencies. Also please note that the lower limits are indicated by the upward facing arrows in the plots.

§4.2. Results

The spectral indices of each source derived from the frequency versus flux density plots are listed in Table 4.4. The resultant extrapolated flux density values for each source derived by using the spectral index values are listed in Table 4.5. MWA data

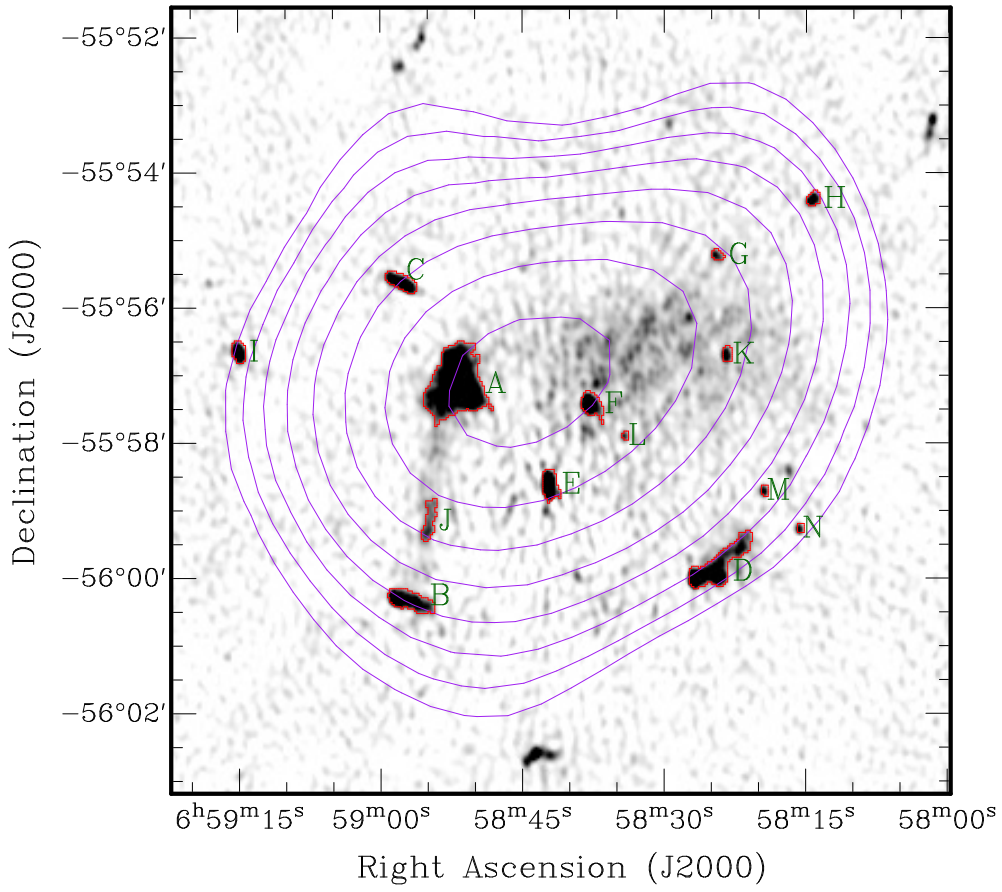

Figure 4.1: MWA contours at 180 MHz overlaid on 1344 MHz ATCA high resolution image. The individual sources of the cluster were labelled A to N.

Table 4.1: Flux density values from 0.844 GHz to 8.896 GHz for sources A to J. At 8.832 GHz the values for sources B, C, H and J are lower limits as these sources were not detected fully for complete flux density calculation.

Frequency	Integrated flux density by source in Jy									
(GHz)	A	B	C	D	E	F	G	H	I	J
0.843	0.13702	0.01613	0.00678	0.03185	0.05904	0.02929	N/A	N/A	0.006481	0.00685
1.344	0.08067	0.01037	0.00631	0.031918	0.038073	0.020571	0.000845	0.001771	0.005788	0.00636
2.184	N/A	0.00601	0.00363	N/A	N/A	N/A	N/A	N/A	N/A	N/A
2.496	0.03878	0.0055	0.003618	0.016357	0.01828	0.01112	0.00028	0.0008575	0.003542	0.001722
4.604	0.0199	0.00259	0.00164	0.0139	0.00873	0.0081	0.000336	N/A	0.00478	N/A
4.8	0.018204	0.00273	0.003042	0.012984	0.00897	0.006751	N/A	0.001042	0.002995	0.00041
4.86	0.01829	0.00234	0.00167	0.0129	0.00829	0.00804	N/A	N/A	N/A	N/A
5.116	0.01675	0.0019	0.0015	0.0126	0.0078	0.007454	N/A	0.00108	N/A	N/A
5.372	0.01519	0.002	0.0014	0.01196	0.0074	0.007704	N/A	N/A	N/A	N/A
5.628	0.01442	0.0018	0.0013	0.0113	0.0071	0.00748	N/A	N/A	N/A	N/A
5.884	0.01269	0.00129	0.0012	0.01064	0.00686	0.006911	N/A	N/A	N/A	N/A
6.14	0.01206	0.00117	0.0012	0.01006	0.00673	0.006877	N/A	N/A	N/A	N/A
6.208	0.01108	0.00217	0.001102	0.00936	0.005278	0.005252	N/A	N/A	0.001514	N/A
6.396	0.0116	0.00095	0.00107	0.0095	0.00617	0.006606	N/A	N/A	N/A	N/A
8.768	N/A	N/A	N/A	N/A	N/A	0.00346	N/A	N/A	N/A	N/A
8.832	0.004061	0.000169	0.00017	0.003648	0.002303	0.003564	N/A	0.00014	N/A	0.00007
8.896	N/A	N/A	N/A	N/A	N/A	0.00334	N/A	N/A	N/A	N/A

Table 4.2: Total error values on flux density from 0.844 GHz to 8.896 GHz for sources A to J.

Frequency	Total error on integrated flux density (Jy)									
(GHz)	A	B	C	D	E	F	G	H	I	J
0.843	0.006914	0.001232	0.000991	0.001838	0.003095	0.001736	N/A	N/A	0.000809	0.001629
1.344	0.004034	0.000521	0.000319	0.001597	0.001904	0.001342	0.000062	0.000100	0.000293	0.000320
2.184	N/A	0.000354	0.000261	N/A	N/A	N/A	N/A	N/A	N/A	N/A
2.496	0.002278	0.000308	0.000228	0.000823	0.000924	0.000699	0.000076	0.000101	0.000199	0.000113
4.604	0.001012	0.000226	0.000203	0.000719	0.000474	0.000445	N/A	N/A	N/A	N/A
4.8	0.000912	0.000151	0.000165	0.000652	0.000453	0.000344	N/A	0.000082	0.000163	0.000121
4.86	0.000931	0.000208	0.000191	0.000668	0.000449	0.000437	N/A	N/A	N/A	N/A
5.116	0.000855	0.000195	0.000186	0.000653	0.000426	0.000410	N/A	N/A	N/A	N/A
5.372	0.000781	0.000208	0.000195	0.000625	0.000412	0.000426	N/A	N/A	N/A	N/A
5.628	0.000744	0.000204	0.000194	0.000594	0.000399	0.000416	N/A	N/A	N/A	N/A
5.884	0.000651	0.000160	0.000158	0.000552	0.000373	0.000375	N/A	N/A	N/A	N/A
6.14	0.000620	0.000156	0.000156	0.000523	0.000366	0.000373	N/A	N/A	N/A	N/A
6.208	0.000578	0.000199	0.000119	0.000497	0.000284	0.000283	N/A	N/A	0.000130	N/A
6.396	0.000599	0.000158	0.000160	0.000498	0.000343	0.000363	N/A	N/A	N/A	N/A
8.768	N/A	N/A	N/A	N/A	N/A	0.000174	N/A	N/A	N/A	N/A
8.832	0.000204	0.000022	0.000022	0.000183	0.000117	0.000179	N/A	0.000022	N/A	0.000020
8.896	N/A	N/A	N/A	N/A	N/A	0.000169	N/A	N/A	N/A	N/A

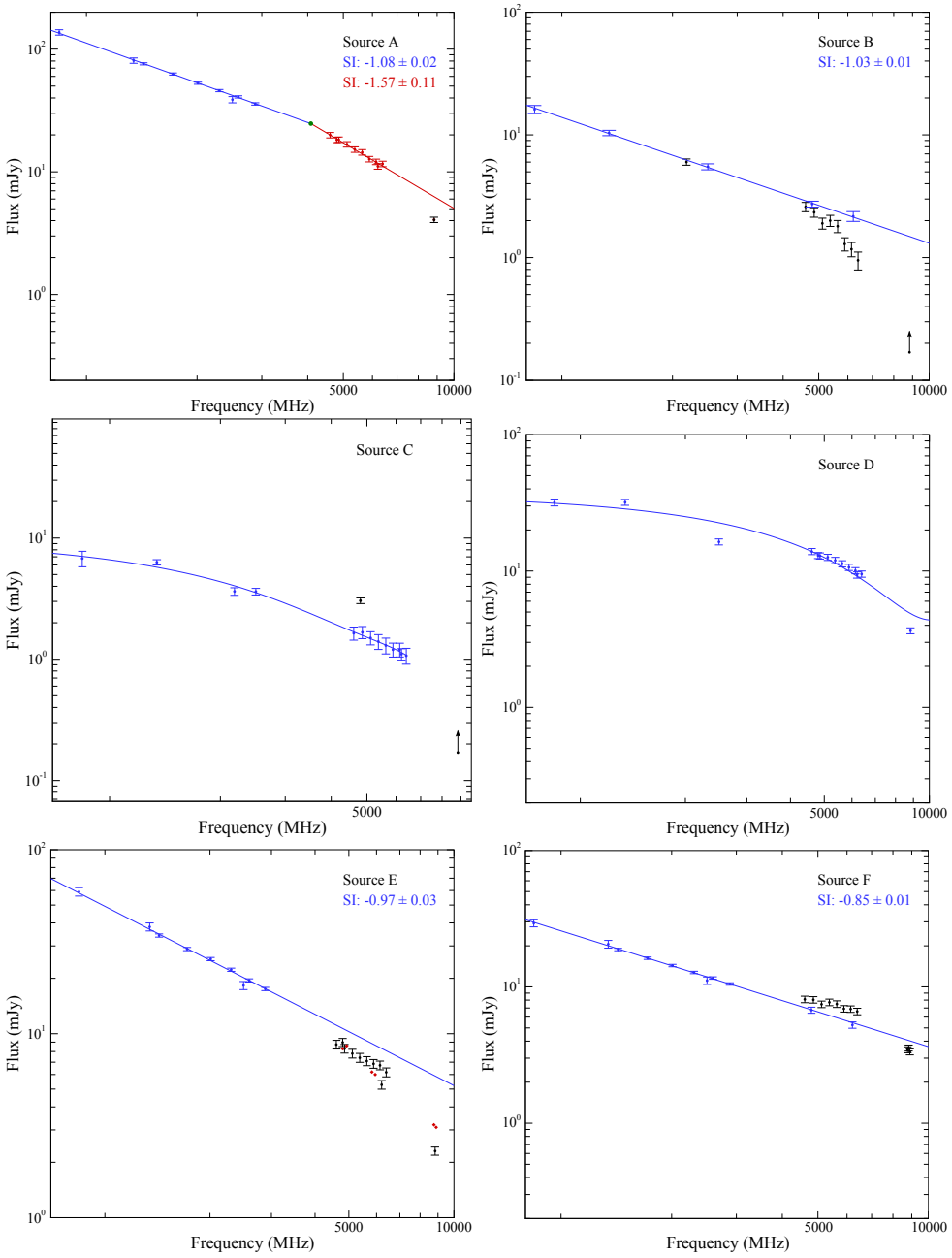

Figure 4.2: Above images are the spectral index plots for source A to F. The plots were generated by Dr Dehghan and the spectral indices were calculated using non linear fit. The points marked in blue were used for spectral index calculation and extrapolation to MWA frequencies. Also please note that the lower limit is indicated by the upward facing arrow. The red points in source E plot were from Liang et al. (2001) and these points were close to our CABB values except at 8.8 GHz.

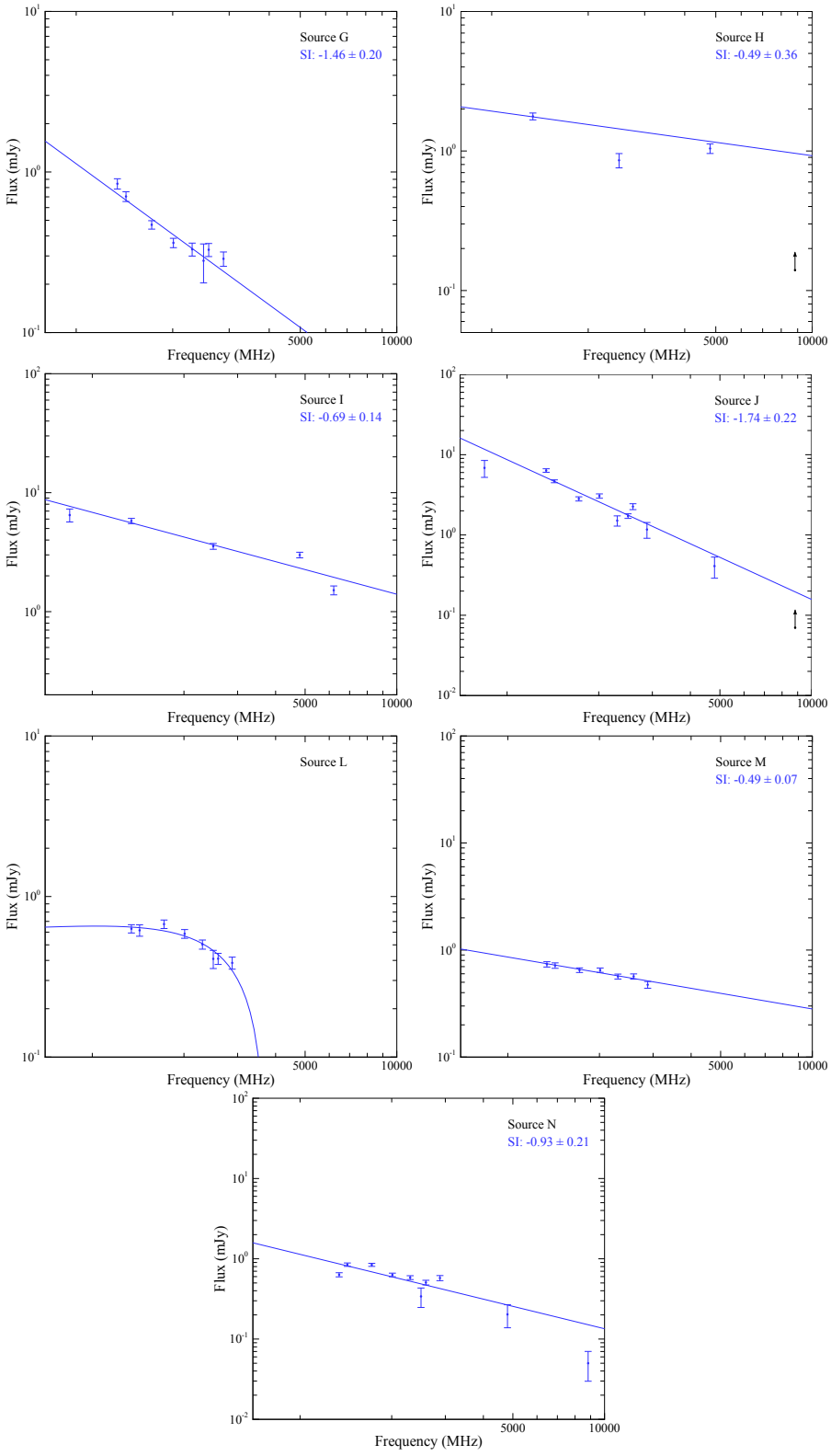

Figure 4.3: Above images are the spectral index plots for sources G to N. The plots were generated by Dr Dehghan and the spectral indices were calculated using non linear fit. The points marked in blue were used for spectral index calculation and extrapolation to MWA frequencies.Also please note that the lower limit is indicated by the upward facing arrow.

Table 4.3: Flux density and error values for sources K,L,M,N

Frequency	Integrated flux density (mJy)				Total error on flux density (mJy)			
(GHz)	K	L	M	N	K	L	M	N
1.344	1.68	0.63	0.736	0.633	0.086	0.0374	0.0418	0.0374
2.496	N/A	0.409	N/A	0.34	N/A	0.05	N/A	0.09
4.8	N/A	N/A	N/A	0.203	N/A	N/A	N/A	0.0647
8.832	N/A	N/A	N/A	0.05	N/A	N/A	N/A	0.0202

Table 4.4: Spectral index values by source. Polynomial fit was used for sources C, D, K, L and hence the slope values are listed as N/A

Source	Coefficient	Slope	Error in slope
A	190359	-1.08	0.02
B	16574.7	-1.03	0.01
C	N/A	N/A	N/A
D	N/A	N/A	N/A
E	41199.4	-0.97	0.03
F	9104.31	-0.85	0.01
G	26788.6	-1.46	0.2
H	54.21	-0.49	0.36
I	792.7	-0.69	0.14
J	1457720	-1.74	0.22
K	N/A	-0.7	-0.07
L	N/A	N/A	N/A
M	24.58	-0.49	0.07
N	686.26	-0.93	0.21

Table 4.5: Extrapolated flux density for each source from 0.118 GHz to 0.18 GHz

Source	Extrapolated flux density by source (Jy)	
	0.180 GHz	0.118 GHz
A	0.710	1.119
B	0.081	0.124
C	0.0092	0.0094
D	0.0353	0.0357
E	0.261	0.394
F	0.110	0.158
G	0.013	0.025
H	0.004	0.005
I	0.022	0.0297
J	0.172	0.358
K	0.0069	0.0092
L	0.00059	0.00058
M	0.00198	0.0024
N	0.0055	0.008
Total	1.432	2.278

at 180 MHz was taken from the commissioning data and the flux density of the entire cluster was measured. The flux density at 180 MHz for the entire system was 1.869 Jy including all the sources and the halo. From the ATCA data, the total flux density of all contaminating sources was calculated to be 1.427 Jy at 180 MHz. Detecting total flux density of all sources with the MWA flux density of the entire cluster gave the resultant flux density of the halo at 180 MHz, to be 0.441 Jy. The spectral index of the bullet cluster from MWA data was -1.196282 using which the total MWA flux density at 118 MHz was derived as 3.0975 Jy. The total flux density of the contaminating sources in the bullet cluster from ATCA data at 118 MHz was extrapolated to be 2.271 Jy. The flux density of the radio halo at 118 MHz can now be derived as 0.825 Jy using the total MWA flux density and the ATCA flux density. The flux density of the halo at 1.344 GHz, 2.496 GHz, 4.8 GHz and 8.832 GHz were derived from our ATCA images and the values are listed in table 4.6. A spectral index fit was made with our flux density values at 1.344 GHz, 2.496 GHz, 4.8 GHz and 8.832 GHz. Flux density for the radio halo at CABB frequencies were not measured due to time constraints and is planned as part of future research. The resultant slope of the spectral index for the halo was calculated to be -2.11$\pm$0.03. The final spectral index plot of the halo is shown in figure 4.4.

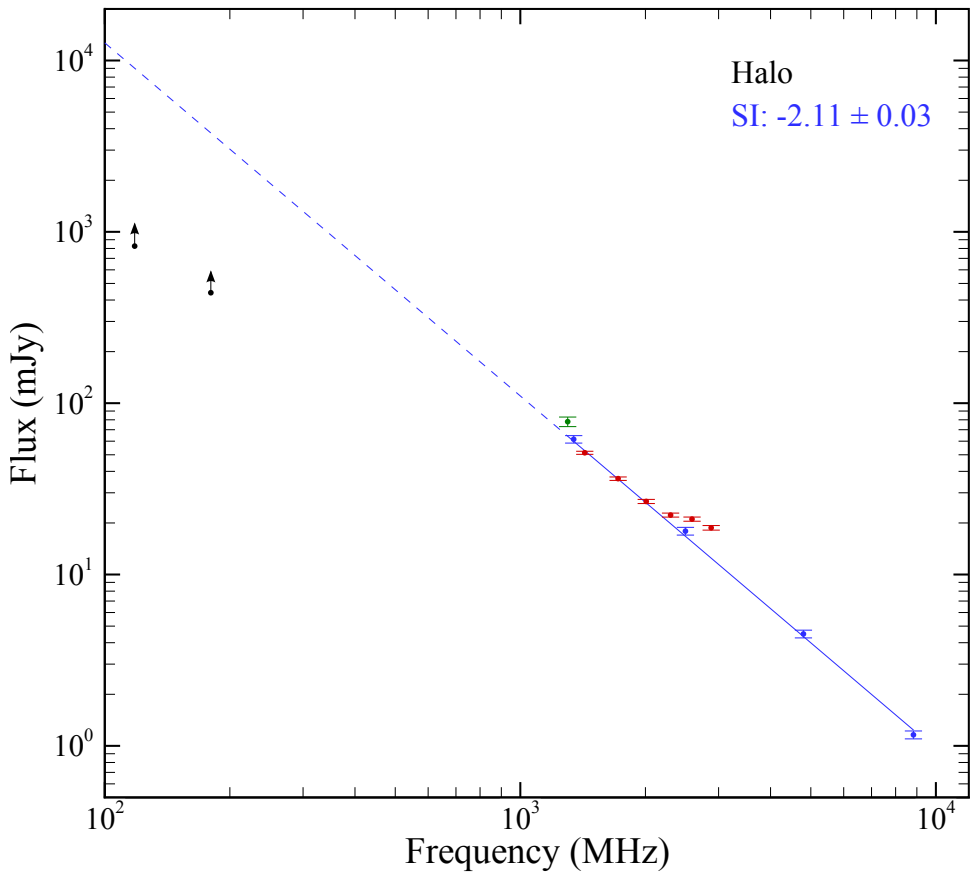

Figure 4.4: Spectral index plot for the radio halo. MWA points are indicated in black with upward arrow suggested as a lower limit value. The points marked in blue were used for spectral index calculation. The points in red were from Shimwell et al. (2014) and green point is from Liang et al. (2000).

Table 4.6: Integrated flux density and associated error of the radio halo by frequency.

Frequency (GHz)	Flux density (Jy)	Error (Jy)	Comments
0.118	0.825	0.289	Extrapolated lower limit value
0.180	0.441	0.144	Extrapolated lower limit value
1.344	0.062	0.0031	Value from this thesis
1.3	0.078	0.005	Value from literature
2.496	0.018	0.00093	Value from this thesis
4.8	0.0045	0.00023	Value from this thesis
8.832	0.0012	0.00006	Value from this thesis
1.429	0.0513	0.0010	Value from literature
1.719	0.0363	0.0008	Value from literature
2.009	0.0267	0.0007	Value from literature
2.299	0.0222	0.0006	Value from literature
2.589	0.0211	0.0006	Value from literature
2.879	0.0187	0.0006	Value from literature

§4.3. Discussion

This section discusses the results of the spectral indices for individual sources of the Bullet cluster. We also discuss and analyse the spectral index results of the radio halo in the cluster.

§4.3.1. Individual sources

The spectral index map of source A (relic) showed spectral bending at 4.532 GHz and it did not follow a straight power law fit for a wider frequency band. Also sources like C, D and L showed characteristics of spectral bending at low frequencies. Further analysis could be performed on these sources to confirm this bending at low frequencies, if a telescope of sufficient resolution were available. For the purpose of this thesis, we assume that our observation of spectral curvature for sources A, C, D and L were real and the spectral index estimates were made accordingly. A third order polynomial fit was used for source C and a second order polynomial was used to fit sources D and L. The spectral indices calculated for sources A, B, E, F, G, J, M and N were in agreement with the values measured by Shimwell et al. (2014).
Source E (06587-5558) is a unique source in the Bullet cluster. This source was discussed in detail by Liang et al. (2001). Our spectral index measurement detected spectral bending between 3 GHz to 4.6 GHz and this agreed with Liang et al. (2001) who showed a spectral break in this region. We measured a flux density of 38 $\pm$ 0.6 mJy at 1.344 GHz and a spectral index of -0.97 between 0.843 GHz and 2.496 GHz for source E. Both these results were in agreement with Liang et al. (2001). The red points in the plot for source E (see Fig 4.2) were from Liang et al. (2001) and these points were close to our CABB values although there were small differences in flux density between our CABB values and the points from this paper. We had used a more recent CABB dataset as compared to the one used by Liang et al. (2001). One possible explanation could be a change in activity in the Active Galactic Nucleus (AGN) of the galaxy over a period of time. Alternatively, this could be due to a change in the lensing effect of the Bullet cluster (Johansson et al., 2012). Similar to the results in Liang et al. (2001), we detected rapid depolarisation from higher to lower frequencies. We observed a 45 % $\pm$ 7% polarisation at 8.8 GHz and we almost detected none at 1.344 GHz. As mentioned in Liang et al. (2001), this property of a steep spectrum which continues to steepen at high frequencies in combination with polarisation suggests the presence of diffuse synchrotron emission in the source.

In trying to understand the nature of source E, Liang et al. (2001) suggested three possible explanations about the nature of this source. They suggest that source E could be a high redshift radio galaxy or a cluster relic due to the presence of a nearby elliptical galaxy or the gravitationally lensed jet fragment of a distant galaxy. Shimwell et al. (2015) discusses the possibility of this source being a bridge between the radio halo and region B of the radio relic, though this seems unlikely from high resolution imaging presented here (see Fig 4.1). But Johansson et al. (2012) has recently concluded that this source is a high redshift galaxy (z >2.8) lensed by the Bullet cluster. Since source E was not the target of this thesis, no further analysis was performed on this investigation. However, we recommend this source as a topic of study for the future.

§4.3.2. Radio halo

The spectral index for the radio halo calculated using our measurements at 1.344 GHz, 2.496 GHz, 4.8 GHz and 8.8 GHz was -2.11±0.03. This slope is steeper than that found in literature. The spectral index values for the halo from Liang et al. (2000) and Shimwell et al. (2014) were -1.3 and -1.5 respectively. However the area chosen for spectral index measurements by Liang et al. (2000) was closer to the center of the source and was a subset of the area chosen in this thesis. As can be seen in 1.344 GHz ATCA images (Fig 3.2), the radio diffuse emission was spread across a larger area compared to the areas discussed in Liang et al. (2000). Also, the measurements from Shimwell et al. (2014) suggest that the spectral index slope for the radio halo was -1.5 for the whole radio halo. This does not agree with our measurement of -2.11. In order to validate the fit, we have included the measurements from Shimwell et al. (2014) and Liang et al. (2000) in our spectral index plot. In figure 4.4, the points in red were from Shimwell et al. (2014) and the green point is from Liang et al. (2000). As can be see in the plot, the first 4 red points fit well with our slope for the spectral index. The last 2 red points deviate from our slope. These points flatten the spectral value and thereby flatten the whole slope. These 2 points could have resulted from an overestimation of the halo flux density due to difference in boundary selection or an under-subtraction of the contaminating sources. We also observed that the 1.3 GHz value from Liang et al. (2000) nearly agreed with our slope. As the next step, high frequency CABB sub-band flux density values from 4.6 GHz to 6.396 GHz could be measured to validate the accuracy of the slope value in our thesis. Future observations might also be necessary to reconcile the difference in

our spectral index value from that in the literature.

We think that we have underestimated the MWA flux density for the radio halo. The model used for fitting most of the individual sources (except C, D, L) was a straight power law fit. Sources A and E had spectral bends between 2.4 GHz and 4.6 GHz frequency points. Sources J and N had some points that did not fall in the straight power law fit line. Sources A, E and J are major flux density contributing sources. For these sources, the power law model would over-estimate the MWA flux density during extrapolation. As a result, the halo flux at MWA frequencies could get over-subtracted. Therefore, we assume that the MWA flux density for the radio halo is a lower limit value.

We observed spectral flattening between 0.180 GHz and 1.344 GHz. We observed the spectral flattening for the radio halo even while assuming that the total flux density of the halo (1.869 Jy) was equal to the total flux density of the cluster from the MWA image. Although this assumption was wrong, this was used as a test case to validate the spectral flattening between 0.180 GHz and 1.344 GHz. Kale and Dwarakanath (2010) and van Weeren et al. (2012) identified spectral steepening in the radio halo of the cluster Abell 2256 using the Giant Meter Radio Telescope (GMRT) and the Low Frequency Array (LOFAR), respectively. But in our case, we observe spectral flattening instead of spectral steepening between 0.180 GHz and 1.344 GHz. This spectral flattening at low frequencies was observed in halos of other clusters as well. Giacintucci et al. (2005) detected spectral flattening of the radio halo in A3256 at frequencies less than 1.4 GHz. The low frequency radio halo investigation of Brunetti et al. (2008) detected spectral flattening for the cluster A521 between 0.25 GHz and 0.630 GHz. Also, Thierbach et al. (2003) detected reduced steepness of spectral index for the radio halo in the Coma cluster at low frequencies. Our result of the spectral index flattening of the radio halo in the Bullet cluster between 0.180 GHz to 1.3 GHz agrees with the results of A3256,A521 and the Coma clusters (Giacintucci et al., 2005),(Brunetti et al., 2008) and (Thierbach et al., 2003).

As expected, we did not detect any polarised emission in the radio halo region in any frequency. As seen in Figure 3.1, there is a point-to-point spatial correlation observed between the radio brightness of the halo and the X-ray brightness. This confirms the connection between the Bremsstrahlung emitting hot plasma and the relativistic plasma in the ICM. Shimwell et al. (2014) found evidence for 2 peaks in the radio halo emission coincident with the X-ray emission. One was in the centroid of the X-ray and the other close to the bullet like structure. As discussed in literature, the presence of X-ray gas and galaxy distribution in the cluster suggests a merger

event occurring the cluster. The shocks produced during this merger process could be a plausible source of energy for the relativistic electrons producing radio halo emission. But if shocks were the source of energy, we should expect a flatter spectral index for the radio halo. Our spectral index value of -2.11 suggests a relatively steep spectral index. This could mean that turbulance could also have played a role in halo formation. The turbulence of the merging clusters could have supplied the energy for the radio halo atleast in some areas. Since the halo diffuse emission is spread across a wider area, the energy could be partly from turbulence and partly from shocks. The colour scaled image from Shimwell et al. (2014) does not suggest many steeper spectral index areas in the halo (see Fig 4.5). But this could be due to the low resolution of this image (FWHM=23.3 arcseconds). So more accurate spectral index measurements across a wider band with more datasets are needed to gain some insight on the nature of diffuse radio halo emission. These new measurements could be used to compare and validate our spectral index value for the radio halo. Also these datasets could be used to plot the spectral index variation across different areas of the radio halo. The variation in steepness could provide some insight into the underlying energy mechanism that drives this diffuse emission.

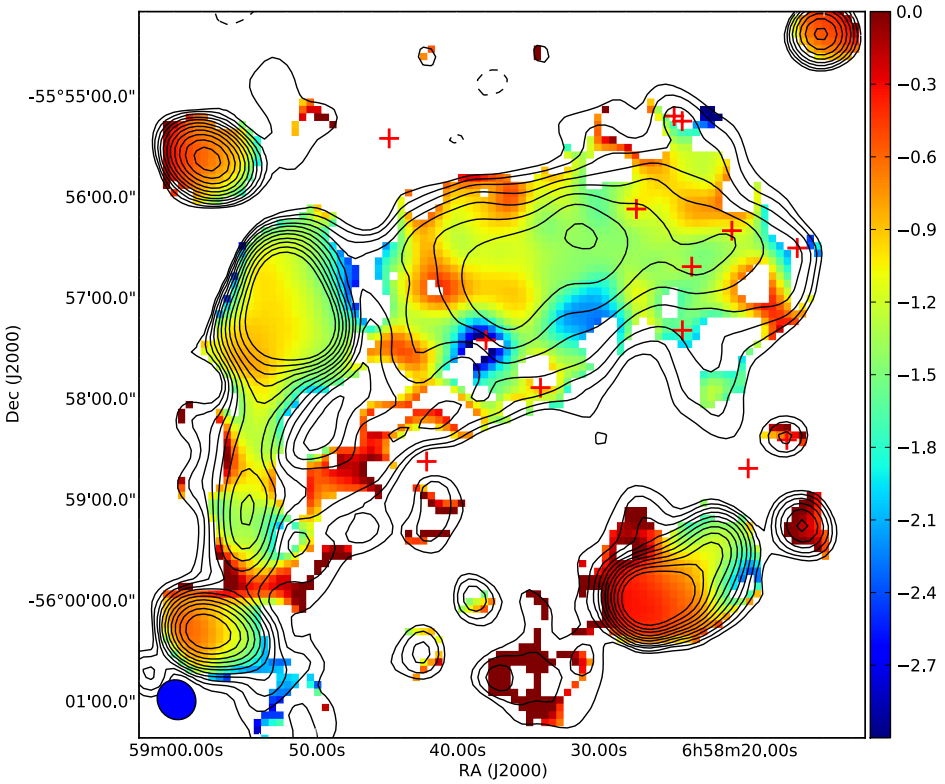

Figure 4.5: Colour scaled spectral index image of the Bullet cluster from Shimwell et al. (2014). This shows that while there is variability in the spectral index of the radio halo. On average it appears to be approximately -1.5.

§5. Conclusion

The objective of this study was to investigate diffuse emission across a wide frequency band ranging from 0.118 GHz to 8.896 GHz using ATCA archival and MWACS data. At the start of this work, we analysed an initial list of 10 SPT clusters and 3 of them were shortlisted for data reduction based on the initial analysis. The shortlisted cluster RXC J0605-3518 did not indicate any diffuse emission. CABB data reduction for SPT-CL J2023-5535 indicated possible diffuse emission in the cluster, but the results were not conclusive with the available datasets. The main focus of this thesis has since then shifted to multi-frequency investigation of diffuse emission in the Bullet cluster. The relevance of studying diffuse emission is to understand the properties of the ICM and the cluster's dynamic nature. The presence of a radio halo and a radio relic indicates the presence of non thermal components. The correlation between diffuse radio emission and X-ray brightness indicates a direct link between thermal and non thermal components in the ICM and their role in cluster formation and evolution (Feretti et al., 2012). Studying the spectral characteristics of the diffuse emission could provide information on the the mechanism involved in accelerating electrons to relativistic energies in the ICM. In pursuing this, we have reduced and imaged the ATCA archival datasets of the Bullet cluster from 1.344 GHz to 8.896 GHz. We have derived the spectral indices of the individual sources and used them for flux density extrapolation to MWA frequencies. We have used MWACS data to derive the flux density of the radio halo at MWA frequencies. The main conclusions of our study are :

1. The radio relic was detected at all frequencies in the cluster periphery. Polarised flux density in region A of the relic was detected at all frequencies except at 1.344 GHz. The fractional polarisation of region A increases with frequency. Our spectral index values for region A and B were -1.08$\pm$0.02 and -1.74 $\pm$ 0.22 respectively, and these values agreed with Shimwell et al. (2015). We detected spectral bending at 4.532 GHz for region A. As expected for the radio relic, the X-ray edge correlates with the location of region B indicating the presence of shock front. We contemplated the argument made by Shimwell et al. (2015) that the source of the electrons in region A of the relic could be supplied by a dead radio galaxy. Our polarisation angle images across the wide frequency bands indicate that the seed electrons

from region A could have polluted region B thereby providing the seed electrons for reaccelaration.

2. During the course of our investigation, we encountered an interesting source (06587-5558), referred to as E in this thesis. Our results for spectral bending of this source agreed with Liang et al. (2001). Our low frequency spectral index value -0.97 and flux density value of the source at 1.344 GHz agreed with Liang et al. (2001). We also detected rapid depolarisation in this source and our 8.8 GHz polarisation percentage of 45%±7% was consistent with the value of 54%±11% calculated by Liang et al. (2001). The steep spectrum and polarised flux density indicated the presence of diffuse emission in the source. Our high frequency CABB results did not exactly align with Liang et al. (2001) and we think that this might be due to changes in the activity of the AGN or lensing effects in the cluster. Johansson et al. (2012) concluded that this source is a high redshift galaxy (z >2.8) lensed by the Bullet cluster. We are planning to further investigate this source in the future.

3. The radio halo was detected at all frequencies from 1.344 GHz to 8.896 GHz. Spectral index measurements were made for all sources in the Bullet cluster and the results were used to extrapolate the flux density of the individual sources at MWA frequencies. Since spectral bending was observed at high frequencies for some sources including the radio relic, only low frequency points were used for extrapolation. The model used for fitting most of the individual sources (except C, D and L) was a straight power law fit. The spectral bending in bright sources A and E would result in overestimation of their flux density values at 0.118 GHz using the power law model. This would have resulted in underestimation of flux density for the radio halo. So the halo flux density values at MWA frequencies were assumed to be lower limit values. The flux density of the radio halo at 0.118 GHz and 0.180 GHz were estimated to be 0.825±0.289 Jy and 0.441±0.144 Jy, respectively.

4. The spectral index of the halo between 1.344 GHz to 8.896 GHz was -2.11±0.03. We identified spectral flattening for the Bullet cluster at low frequencies from 0.180 GHz to 1.344 GHz and the flattened spectral index value between these points was -1.02. This did not agree with the spectral steepening observations made by van Weeren et al. (2012) and Kale and Dwarakanath (2010) for the halo in Abell 2256. However, our result of spectral index flattening of the radio halo between 0.180 GHz to 1.3 GHz for the Bullet cluster agreed with the halo in A3251, A 521 and the Coma clusters (Giacintucci et al., 2005), (Thierbach et al., 2003), (Brunetti et al., 2008).

5. We did not detect any polarised emission in the radio halo region across all frequencies nor did we expect to, radio halos are known to be unpolarised. Shimwell

et al. (2014) discussed about the spatial correlation of X-ray brightness with the radio halo brightness suggesting a cluster merger event powering the emission. This supports the theory that the shocks produced during this merger could be a plausible source of energy for the relativistic electrons producing radio halo emission. We find a discrepancy in the spectral index value. Our spectral index value of -2.11 did not agree with Shimwell et al. (2014) value of -1.5. We think that this could be because of a difference in boundary selection or an under-subtraction of contaminating sources from the halo by Shimwell et al. (2014) in their 2.59 GHz and 2.88 GHz measurements. The flux density values from Shimwell et al. (2014) at 1.4 GHz, 1.7 GHz, 2.01 GHz and 2.3 GHz agreed with our fit. Also the halo flux density value at 1.3 GHz from Liang et al. (2000) agreed with our flux density value. Inclusion of our CABB points in the plot could provide a clearer picture on the accuracy of our spectral index value.

Further to this thesis, future endeavours can involve measurement of the flux density of the radio halo in the Bullet cluster across the 5.5 GHz CABB band and fit them to the spectral index plot of the radio halo.

Bibliography

Abell, G. O. (1958). The Distribution of Rich Clusters of Galaxies. *Astrophysical Journal Supplement*, 3:211.

Bock, D. C.-J., Large, M. I., and Sadler, E. M. (1999). SUMSS: A Wide-Field Radio Imaging Survey of the Southern Sky. I. Science Goals, Survey Design, and Instrumentation. *The Astronomical Journal*, 117:1578–1593.

Böhringer, H., Schuecker, P., Guzzo, L., Collins, C. A., Voges, W., Cruddace, R. G., Ortiz-Gil, A., Chincarini, G., De Grandi, S., Edge, A. C., MacGillivray, H. T., Neumann, D. M., Schindler, S., and Shaver, P. (2004). The ROSAT-ESO Flux Limited X-ray (REFLEX) Galaxy cluster survey. V. The cluster catalogue. *Astronomy and Astrophysics*, 425:367–383.

Bonafede, A., Feretti, L., Giovannini, G., Govoni, F., Murgia, M., Taylor, G. B., Ebeling, H., Allen, S., Gentile, G., and Pihlström, Y. (2009). Revealing the magnetic field in a distant galaxy cluster: discovery of the complex radio emission from MACS J0717.5 +3745. *Astronomy and Astrophysics*, 503:707–720.

Bonafede, A., Intema, H. T., Brüggen, M., Girardi, M., Nonino, M., Kantharia, N., van Weeren, R. J., and Röttgering, H. J. A. (2014). Evidence for Particle Reacceleration in the Radio Relic in the Galaxy Cluster PLCKG287.0+32.9. *The Astrophysical Journal*, 785:1.

Brunetti, G., Giacintucci, S., Cassano, R., Lane, W., Dallacasa, D., Venturi, T., Kassim, N. E., Setti, G., Cotton, W. D., and Markevitch, M. (2008). A low-frequency radio halo associated with a cluster of galaxies. *Nature*, 455:944–947.

Burns, J. O., Rhee, G., Roettiger, K., Pinkney, J., Loken, C., Owen, F. N., and Voges, W. (1994). On the Effects of X-Ray Subclumps and Cluster/Subcluster Mergers on Extended Radio Sources. In Bicknell, G. V., Dopita, M. A., and Quinn, P. J., editors, *The Physics of Active Galaxies*, volume 54 of *Astronomical Society of the Pacific Conference Series*, page 325.

Cassano, R. and Others (2010). On the Connection Between Giant Radio Halos and Cluster Mergers. *The Astrophysical Journal Letter*, 721:L82–L85.

Clarke, T. E., Kronberg, P. P., and Böhringer, H. (2001). A New Radio-X-Ray Probe of Galaxy Cluster Magnetic Fields. *The Astrophysical Journal*, 547:L111–L114.

Condon, J. J., Cotton, W. D., Greisen, E. W., Yin, Q. F., Perley, R. A., Taylor, G. B., and Broderick, J. J. (1998). The NRAO VLA Sky Survey. *The Astronomical Journal*, 115:1693–1716.

Dennison, B. (1980). Formation of radio halos in clusters of galaxies from cosmic-ray protons. *The Astrophysical Journal Letter*, 239:L93–L96.

Dwarakanath, K. S., Malu, S., and Kale, R. (2011). Discovery of a Giant Radio Halo in a Massive Merging Cluster at z = 0.443. *Journal of Astrophysics and Astronomy*, 32:529–532.

Ensslin, T. A., Biermann, P. L., Klein, U., and Kohle, S. (1998). Cluster radio relics as a tracer of shock waves of the large-scale structure formation. *Astronomy and Astrophysics*, 332:395–409.

Fabian, A. C. (1994). Cooling Flows in Clusters of Galaxies. *Annual Review of Astronomy and Astrophysics*, 32:277–318.

Feretti, L. (2008). Radio emission in clusters and connection to X-ray emission . *Memorie della Societa Astronomica Italiana*, 79:176.

Feretti, L., Giovannini, G., Govoni, F., and Murgia, M. (2012). Clusters of galaxies: observational properties of the diffuse radio emission. *The Astronomy and Astrophysics Review*, 20:54.

Feretti, L. and Johnston-Hollitt, M. (2004). Magnetic fields in clusters of galaxies. *New Astronomy Reviews*, 48:1145–1150.

Ferrari, C., Govoni, F., Schindler, S., Bykov, A. M., and Rephaeli, Y. (2008). Observations of Extended Radio Emission in Clusters. *Space Science Reviews*, 134:93–118.

Giacintucci, S., Venturi, T., Brunetti, G., Bardelli, S., Dallacasa, D., Ettori, S., Finoguenov, A., Rao, A. P., and Zucca, E. (2005). Spectral properties and origin of the radio halo in A3562. *Astronomy and Astrophysics*, 440:867–879.

Giacintucci, S., Venturi, T., Macario, G., Dallacasa, D., Brunetti, G., Markevitch, M., Cassano, R., Bardelli, S., and Athreya, R. (2008). Shock acceleration as origin of the radio relic in A 521? *Astronomy and Astrophysics*, 486:347–358.

Giovannini, G., Bonafede, A., Feretti, L., Govoni, F., Murgia, M., Ferrari, F., and Monti, G. (2009). Radio halos in nearby (z = 0.4) clusters of galaxies. *Astronomy and Astrophysics*, 507:1257–1270.

Gitti, M., Ferrari, C., Domainko, W., Feretti, L., and Schindler, S. (2007). Discovery of diffuse radio emission at the center of the most X-ray-luminous cluster RX J1347.5-1145. *Astronomy and Astrophysics*, 470:L25–L28.

Gooch, R. (2006). Karma user manual.

Govoni, F., Murgia, M., Feretti, L., Giovannini, G., Dallacasa, D., and Taylor, G. B. (2005). A2255: The first detection of filamentary polarized emission in a radio halo. *Astronomy and Astrophysics*, 430:L5–L8.

Hurley-Walker, N., Morgan, J., Wayth, R. B., Hancock, P. J., Bell, M. E., Bernardi, G., Bhat, R., Briggs, F., Deshpande, A. A., Ewall-Wice, A., Feng, L., Hazelton, B. J., Hindson, L., Jacobs, D. C., Kaplan Nadia Kudryavtseva, D. L., Lenc, E., McKinley, B., Mitchell, D., Pindor, B., Procopio, P., Oberoi, D., Offringa, A., Ord, S., Riding, J., Bowman, J. D., Cappallo, R., Corey, B., Emrich, D., Gaensler, B. M., Goeke, R., Greenhill, L., Hewitt, J., Johnston-Hollitt, M., Kasper, J., Kratzenberg, E., Lonsdale, C., Lynch, M., McWhirter, R., Morales, M. F., Morgan, E., Prabu, T., Rogers, A., Roshi, A., Shankar, U., Srivani, K., Subrahmanyan, R., Tingay, S., Waterson, M., Webster, R., Whitney, A., Williams, A., and Williams, C. (2014). The Murchison Widefield Array Commissioning Survey: A Low-Frequency Catalogue of 14,110 Compact Radio Sources over 6,100 Square Degrees. *ArXiv e-prints*.

Jackson, N. (2008). Principles of Interferometry. In Bacciotti, F., Testi, L., and Whelan, E., editors, *Jets from Young Stars II*, volume 742 of *Lecture Notes in Physics, Berlin Springer Verlag*, page 193.

Johansson, D., Horellou, C., Lopez-Cruz, O., Muller, S., Birkinshaw, M., Black, J. H., Bremer, M. N., Wall, W. F., Bertoldi, F., Castillo, E., and Ibarra-Medel, H. J. (2012). Molecular gas and dust in the highly magnified z ˜ 2.8 galaxy behind the Bullet Cluster. *The Astrophysical Journal*, 543:A62.

Johnston-Hollitt, M. (2003). *Detection of magnetic fields and diffuse radio emission in Abell 3667 and other rich southern clusters of galaxies*. PhD thesis, University of Adelaide.

Johnston-Hollitt, M. and Ekers, R. D. (2004). Faraday Rotation Measures through the Cores of Southern Galaxy Clusters. *ArXiv Astrophysics e-prints*.

Kale, R. and Dwarakanath, K. S. (2010). Spectral Index Studies of the Diffuse Radio Emission in Abell 2256: Implications for Merger Activity. *The Astrophysical Journal*, 718:939–946.

Kempner, J. C., Blanton, E. L., Clarke, T. E., Enßlin, T. A., Johnston-Hollitt, M., and Rudnick, L. (2004). Conference Note: A Taxonomy of Extended Radio Sources in Clusters of Galaxies. In Reiprich, T., Kempner, J., and Soker, N., editors, *The Riddle of Cooling Flows in Galaxies and Clusters of galaxies*, page 335.

Kravtsov, A. V. and Borgani, S. (2012). Formation of Galaxy Clusters. *ARAA*, 50:353–409.

Large, M. I., Mathewson, D. S., and Haslam, C. G. T. (1959). A High-Resolution Survey of the Coma Cluster of Galaxies at 408 Mc./s. *Nature*, 183:1663–1664.

Liang, H., Ekers, R. D., Hunstead, R. W., Falco, E. E., and Shaver, P. (2001). J06587-5558: a very unusual polarized radio source. *Monthly Notices of the Royal Astronomical Society*, 328:L21–L26.

Liang, H., Hunstead, R. W., Birkinshaw, M., and Andreani, P. (2000). A Powerful Radio Halo in the Hottest Known Cluster of Galaxies 1E 0657-56. *The Astrophysical Journal*, 544:686–701.

Markevitch, M., Gonzalez, A. H., Clowe, D., Vikhlinin, A., Forman, W., Jones, C., Murray, S., and Tucker, W. (2004). Direct Constraints on the Dark Matter Self-Interaction Cross Section from the Merging Galaxy Cluster 1E 0657-56. *The Astrophysical Journal*, 606:819–824.

Markevitch, M., Gonzalez, A. H., David, L., Vikhlinin, A., Murray, S., Forman, W., Jones, C., and Tucker, W. (2002). A Textbook Example of a Bow Shock in the Merging Galaxy Cluster 1E 0657-56. *The Astrophysical Journal*, 567:L27–L31.

Mazzotta, P. and Giacintucci, S. (2008). Do Radio Core-Halos and Cold Fronts in Non-Major-Merging Clusters Originate from the Same Gas Sloshing? *The Astrophysical Journal Letters*, 675:L9–L12.

McMullin, J. P., Waters, B., Schiebel, D., Young, W., and Golap, K. (2007). CASA Architecture and Applications. In Shaw, R. A., Hill, F., and Bell, D. J., editors, *Astronomical Data Analysis Software and Systems XVI*, volume 376 of *Astronomical Society of the Pacific Conference Series*, page 127.

Pizzo, R. F., de Bruyn, A. G., Bernardi, G., and Brentjens, M. A. (2011). Deep multi-frequency rotation measure tomography of the galaxy cluster A2255. *Astronomy and Astrophysics*, 525:A104.

Pratley, L., Johnston-Hollitt, M., Dehghan, S., and Sun, M. (2013). Using head-tail galaxies to constrain the intracluster magnetic field: an in-depth study of PKS J0334-3900. *Monthly Notices of the Royal Astronomical Society*, 432:243–257.

Ricker, P. M. and Sarazin, C. L. (2001). Off-Axis Cluster Mergers: Effects of a Strongly Peaked Dark Matter Profile. *The Astrophysical Journal*, 561:621–644.

Rieger, F. M., Bosch-Ramon, V., and Duffy, P. (2007). Fermi acceleration in astrophysical jets. *Astrophysics and Space Science*, 309:119–125.

Rybicki, G. B. and Lightman, A. P. (1986). *Radiative Processes in Astrophysics*.

Ryu, D., Kang, H., Hallman, E., and Jones, T. W. (2003). Cosmological Shock Waves and Their Role in the Large-Scale Structure of the Universe. *The Astrophysical Journal*, 593:599–610.

Sanders, J. S., Fabian, A. C., and Smith, R. K. (2011). Constraints on turbulent velocity broadening for a sample of clusters, groups and elliptical galaxies using XMM-Newton. *Monthly Notices of the Royal Astronomical Society*, 410:1797–1812.

Sault, R. and Killeen, N. (1998). The miriad user guide, australia telescope national facility, sydney.

Sault, R. J., Teuben, P. J., and Wright, M. C. H. (1995). A Retrospective View of MIRIAD. In Shaw, R. A., Payne, H. E., and Hayes, J. J. E., editors, *Astronomical Data Analysis Software and Systems IV*, volume 77 of *Astronomical Society of the Pacific Conference Series*, page 433.

Shimwell, T. W., Brown, S., Feain, I. J., Feretti, L., Gaensler, B. M., and Lage, C. (2014). Deep radio observations of the radio halo of the bullet cluster 1E 0657-55.8. *Monthly Notices of the Royal Astronomical Society*, 440:2901–2915.

Shimwell, T. W., Markevitch, M., Brown, S., Feretti, L., Gaensler, B. M., Johnston-Hollitt, M., Lage, C., and Srinivasan, R. (2015). Another shock for the Bullet cluster, and the source of seed electrons for radio relics. *Monthly Notices of the Royal Astronomical Society*, 449:1486–1494.

Springel, V., White, S. D. M., Jenkins, A., Frenk, C. S., Yoshida, N., Gao, L., Navarro, J., Thacker, R., Croton, D., Helly, J., Peacock, J. A., Cole, S., Thomas, P., Couchman, H., Evrard, A., Colberg, J., and Pearce, F. (2005). Simulations of the formation, evolution and clustering of galaxies and quasars. *Nature*, 435:629–636.

Thierbach, M., Klein, U., and Wielebinski, R. (2003). The diffuse radio emission from the Coma cluster at 2.675 GHz and 4.85 GHz. *Astronomy and Astrophysics*, 397:53–61.

Tingay, S., Goeke, R., Hewitt, J. N., Morgan, E., Remillard, R. A., Williams, C. L., Bowman, J. D., Emrich, E., Ord, S. M., Booler, T., Crosse, B., Pallot, D., Arcus, W., Colegate, T., Hall, P. J., Herne, D., Lynch, M. J., Schlagenhaufer, F., Tremblay, S., Wayth, R. B., Waterson, M., Mitchell, D. A., Sault, R. J., Webster, R. L., Wyithe, J. S. B., Morales, M. F., Hazelton, B. J., Wicenec, A., Williams, A., Barnes, D., Bernardi, G., Greenhill, L. J., Kasper, J. C., Briggs, F., McKinley, B., Bunton, J. D., deSouza, L., Koenig, R., Pathikulangara, J., Stevens, J., Cappallo, R. J., Corey, B. E., Kincaid, B. B., Kratzenberg, E., Lonsdale, C. J., McWhirter, S. R., Rogers, A. E. E., Salah, J. E., Whitney, A. R., Deshpande, A., Prabu, T., Roshi, A., Udaya-Shankar, N., Srivani, K. S., Subrahmanyan, R., Gaensler, B. M., Johnston-Hollitt, M., Kaplan, D. L., and Oberoi, D. (2012). Realisation of a low frequency SKA Precursor: The Murchison Widefield Array. In *Resolving The Sky - Radio Interferometry: Past, Present and Future*, page 36.

Tucker, W., Blanco, P., Rappoport, S., David, L., Fabricant, D., Falco, E. E., Forman, W., Dressler, A., and Ramella, M. (1998). 1E 0657-56: A Contender for the Hottest Known Cluster of Galaxies. *The Astrophysical Journal*, 496:L5–L8.

van Weeren, R. J., Intema, H. T., Lal, D. V., Andrade-Santos, F., Brüggen, M., de Gasperin, F., Forman, W. R., Hoeft, M., Jones, C., Nuza, S. E., Röttgering, H. J. A., and Stroe, A. (2014). A Distant Radio Mini-halo in the Phoenix Galaxy Cluster. *The Astrophysical Journal Letters*, 786:L17.

van Weeren, R. J., Röttgering, H. J. A., Rafferty, D. A., Pizzo, R., Bonafede, A., Brüggen, M., Brunetti, G., Ferrari, C., Orrù, E., Heald, G., McKean, J. P., Tasse, C., de Gasperin, F., Bîrzan, L., van Zwieten, J. E., van der Tol, S., Shulevski, A., Jackson, N., Offringa, A. R., Conway, J., Intema, H. T., Clarke, T. E., van Bemmel, I., Miley, G. K., White, G. J., Hoeft, M., Cassano, R., Macario, G., Morganti, R., Wise, M. W., Horellou, C., Valentijn, E. A., Wucknitz, O., Kuijken, K., Enßlin, T. A., Anderson, J., Asgekar, A., Avruch, I. M., Beck, R., Bell, M. E., Bell, M. R., Bentum, M. J., Bernardi, G., Best, P., Boonstra, A.-J., Brentjens, M., van de Brink, R. H., Broderick, J., Brouw, W. N., Butcher, H. R., van Cappellen, W., Ciardi, B., Eislöffel, J., Falcke, H., Fender, R., Garrett, M. A., Gerbers, M., Gunst, A., van Haarlem, M. P., Hamaker, J. P., Hassall, T., Hessels, J. W. T., Koopmans, L. V. E., Kuper, G., van Leeuwen, J., Maat, P., Millenaar, R., Munk, H., Nijboer, R., Noordam, J. E., Pandey, V. N., Pandey-Pommier, M., Polatidis, A., Reich, W., Scaife, A. M. M., Schoenmakers, A., Sluman, J., Stappers, B. W., Steinmetz, M., Swinbank, J., Tagger, M., Tang, Y., Vermeulen, R., de Vos, M., and van Haarlem, M. P. (2012). First LOFAR observations at very low frequencies of cluster-scale non-thermal emission: the case of Abell 2256. *Astronomy and Astrophysics*, 543:A43.

Vogt, C. and Enßlin, T. A. (2003). Measuring the cluster magnetic field power spectra from Faraday rotation maps of Abell 400, Abell 2634 and Hydra A. *Astronomy and Astrophysics*, 412:373–385.

Whiting, M. T. (2012). DUCHAMP: a 3D source finder for spectral-line data. *Monthly Notices of the Royal Astronomical Society*, 421:3242–3256.

Willson, M. A. G. (1970). Radio observations of the cluster of galaxies in Coma Berenices - the 5C4 survey. *Monthly Notices of the Royal Astronomical Society*, 151:1–44.

Wilson, W. E., Ferris, R. H., Axtens, P., Brown, A., Davis, E., Hampson, G., Leach, M., Roberts, P., Saunders, S., Koribalski, B. S., Caswell, J. L., Lenc, E., Stevens, J., Voronkov, M. A., Wieringa, M. H., Brooks, K., Edwards, P. G., Ekers, R. D., Emonts, B., Hindson, L., Johnston, S., Maddison, S. T., Mahony, E. K., Malu, S. S., Massardi, M., Mao, M. Y., McConnell, D., Norris, R. P., Schnitzeler, D., Subrahmanyan, R., Urquhart, J. S., Thompson, M. A., and Wark, R. M. (2011). The Australia Telescope Compact Array Broad-band Backend: description and first results. *Monthly Notices of the Royal Astronomical Society*, 416:832–856.

ZuHone, J. A., Markevitch, M., Brunetti, G., and Giacintucci, S. (2013). Turbulence and Radio Mini-halos in the Sloshing Cores of Galaxy Clusters. *Astrophysical Journal*, 762:78.

§A. Shortlisting galaxy clusters

This chapter presents an investigation of 10 galaxy clusters using radio and optical surveys. From this investigation, 3 galaxy clusters were shortlisted for further data reduction from the ATCA archive. The clusters in the shortlist were RXC J0605-3518, SPT-CL J2023-5535 and SPT-CL J0658-5556. RXC J0605-3518 did not indicate any diffuse emission and SPT-CL J2023-5535 indicated possible diffuse emission but required more data to be conclusive. The detailed study of RXC J0605-3518 (bullet cluster) was the topic of chapters 3, 4 and 5.

§A.1. Initial list

We chose a sample of 10 massive galaxy clusters to investigate the presence of any diffuse emission. They were drawn from a sample of clusters observed with the South Pole Telescope (SPT) shown to have high Sunyaev-Zeldovich (SZ) signals. The SZ effect is produced by the distortion of the cosmic microwave background radiation produced by inverse Compton scattering of high energy electrons in the galaxy clusters. The aim of the initial analysis was to identify sources with possible extended emission using the existing image datasets from NASA *SkyView* archive. The shortlisted candidates were followed up for in-depth analysis using ATCA and MWA data. *SkyView*[1] is a web based archive of images that stores survey data across the band starting from radio to Gamma ray surveys. Images from Digitized Sky Survey, Sydney University Molonglo Sky Survey, Green Bank 6-cm survey and NRAO VLA Sky Survey were downloaded for analysing the initial 10 galaxy clusters listed below

1. SPT-CL J0658-5556 - Bullet cluster
2. RXC J0645-5413
3. RXC J1236-3354
4. RXC J0605-3518
5. RXC J0616-4748
6. SPT-CL J0628-4143
7. SPT-CL J0638-5358
8. SPT-CL J2023-5535

[1] http://skyview.gsfc.nasa.gov

9. SPT-CL J2031-4037
10. SPT-CL J0615-5746

The Digitized Sky Survey (DSS) is a digital version of several optical images of the night sky. The National Geographic Society - Palomar Observatory Sky Survey provided most source data for the northern sky. DSS also includes the digititized Southern Sky Survey conducted at the UK Southern Schmidt Survey Group by the Royal Observatory, Edinburgh and the Anglo-Australian Observatory. Sydney University Molonglo Sky Survey (SUMSS) is a radio survey of the southern sky at declination -30° at 843 MHz using the Molonglo Observatory Synthesis Telescope (MOST). The final data products of SUMSS are 4 × 4 degree mosaiced images and source catalogue (Bock et al., 1999). The Green Bank 6-cm (GB6) is a 4.85 GHz sky survey was made using a 91 m telescope during November 1986 and October 1987. The final set of images covering the declination band from 0 to +75 deg was constructed with data from both time periods. The NRAO VLA Sky Survey (NVSS) is a radio continuum survey covering the sky north of -40 deg declination. The full NRAO VLA Sky Survey (NVSS) is based on 217446 snapshot observations of partially overlapping primary beam areas, each of which were imaged separately. The small snapshot images were weighted, corrected, and combined to yield a set of 2326 large 4° × 4° image cubes (Condon et al., 1998).

§A.2. Analysis

This section discusses the analysis done on clusters listed above and the corresponding results inferred from the images. The Karma toolkit was used for image visualisation and image analysis in this thesis. Karma has a number of modules to manipulate data files, convert file formats and to perform other tasks. *kvis* is a module of karma which is an image/movie viewer that can load multiple datasets, display multiple windows, overlay contours, annotations, show multiple overlaid profiles and so forth (Gooch, 2006). Images from *SkyView* were loaded into kvis and analysed for potential extended emission. Following subsections discuss each galaxy cluster chosen for analysis and selection of potential candidates. Please note that all radio contours in this thesis start at 3 times the noise level of the image and increase in multiples of $\sqrt{2}$.

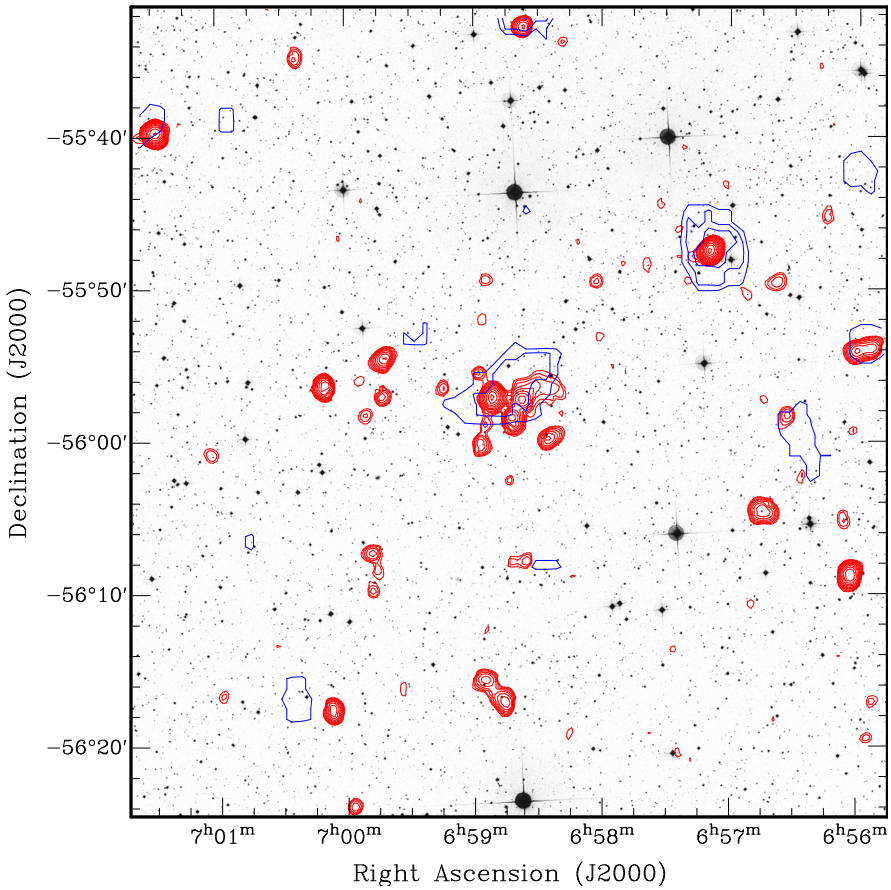

Figure A.1: DSS optical image of Bullet cluster overlaid with red contours of SUMMS at 843 MHz and blue contours of GB6 at 4.8 GHz

§A.2.1. SPT-CL J0658-5556

The Bullet cluster is one of the hottest known galaxy clusters consisting of bullet a like shock wave located on the right side of the cluster. The redshift for the cluster is 0.296 and the scale of the cluster is 4.452 kpc (Tucker et al., 1998). DSS, SUMSS and GB6 images were available for this cluster. Fig A.1 shows the DSS image of SPT-CL J0658-5556 (Bullet cluster) overlaid with SUMSS (red contours) and GB6 (blue contours). The SUMSS contours present in regions of no visible galaxy showed evidence of potential diffuse emission in the cluster centre.

§A.2.2. RXC J0605-3518 and SPT-CL J2023-5535

The cluster RXC J0605-3518 has a redshift value of z=0.141100 ± 0.000780 (Sanders et al., 2011). The cluster SPT-CL J2023-5535 has a redshift value of z=0.232000 (Böhringer et al., 2004). DSS, SUMSS and NVSS images were downloaded for the

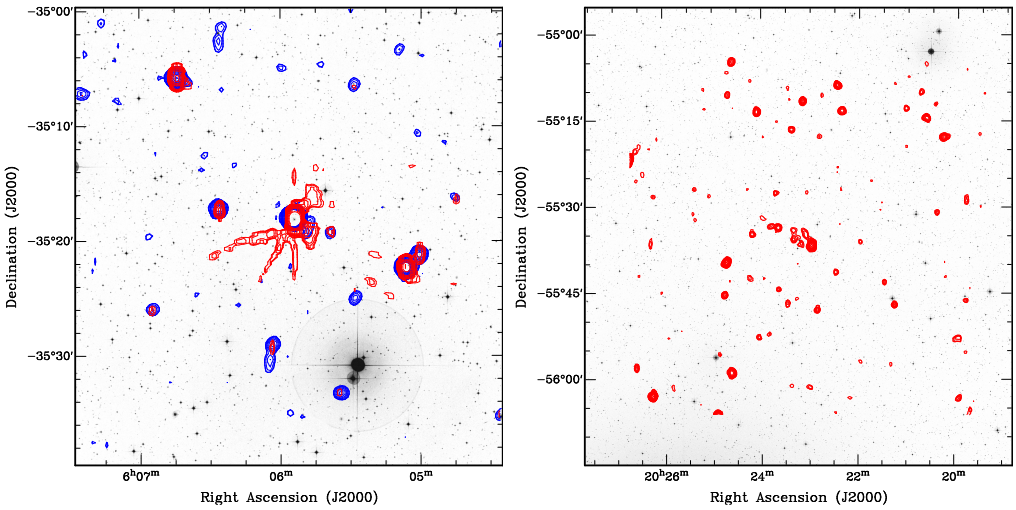

Figure A.2: DSS optical image of RXC J0605-3518(left) overlaid with red contours of SUMMS at 843 MHz and blue contours of NVSS at 1.4 GHz and DSS image of SPT-CL J2023-5535 (right) overlaid with red SUMMS contours

cluster RXC J0605-3518. Fig A.2 shows the DSS image of this cluster overlaid with SUMSS red contours and NVSS blue contours. For SPT-CL J2023-5535 cluster only DSS and SUMSS images (red contours) were available (see Fig A.2). These images hinted that there could be diffuse emission at the cluster centre in both these clusters and they were hence shortlisted for further investigation.

§A.2.3. RXC J0645-5413, RXC J1236-3354, RXC J0616-4748 and SPT-CL J0628-4143

The RXC J0645-5413, RXC J1236-3354, RXC J0616-4748 and SPT-CL J0628-4143 clusters‘ DSS and SUMMS data were available. Fig A.3 shows the DSS image of these clusters overlaid with SUMSS contours in red and they showed no evidence of any potential diffuse emission. These clusters were hence not shortlisted for further investigation.

§A.2.4. SPT-CL J2031-4037, SPT-CL J0615-5746 and SPT-CL J0638-5358

DSS and SUMMS data were available for SPT-CL J2031-4037, SPT-CL J0615-5746 and SPT-CL J0638-5358. Fig A.4 shows the DSS image of these clusters overlaid with SUMSS contours in red. They indicate no potential diffuse emission in the

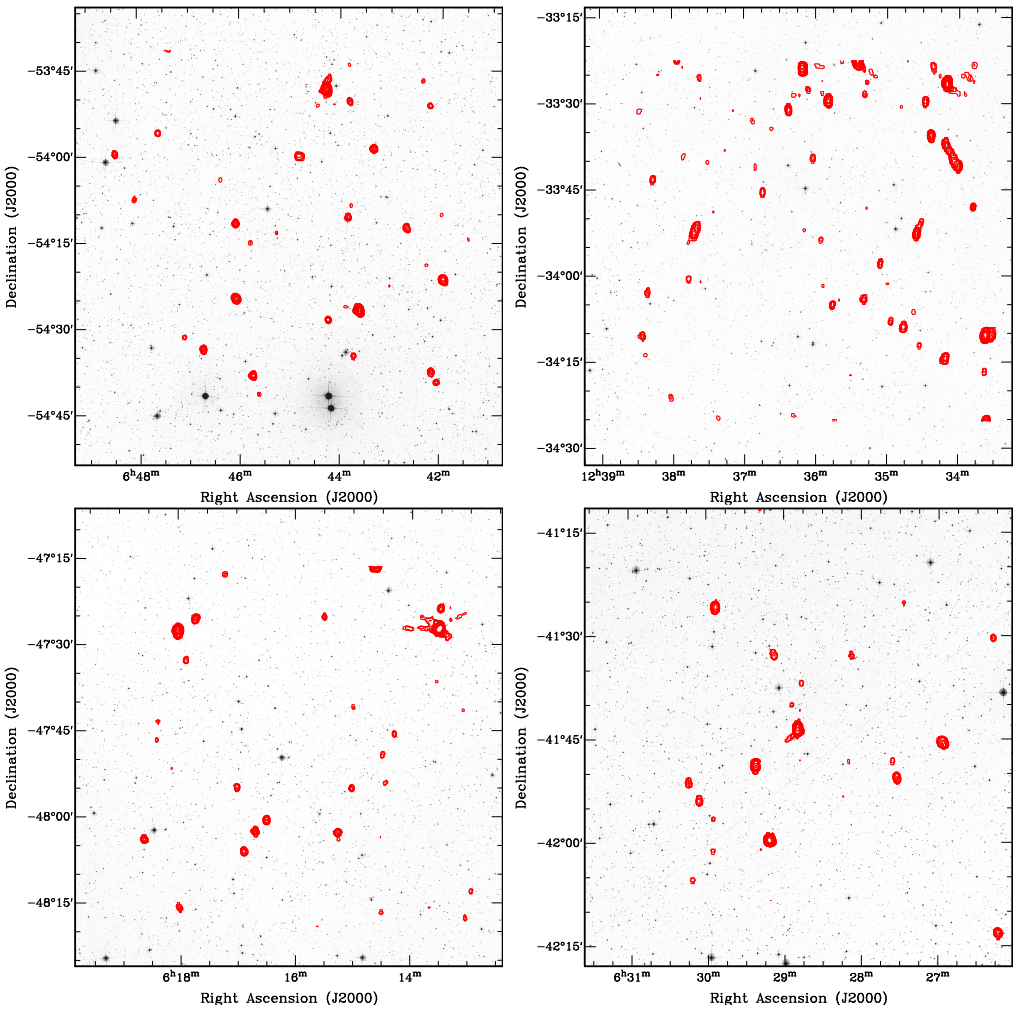

Figure A.3: DSS optical images of RXC J0645-5413(top left), RXC J1236-3354(top right), RXC J0616-4748 (bottom left) and SPT-CL J0628-4143(bottom right) overlaid with red contours of SUMMS at 843 MHz

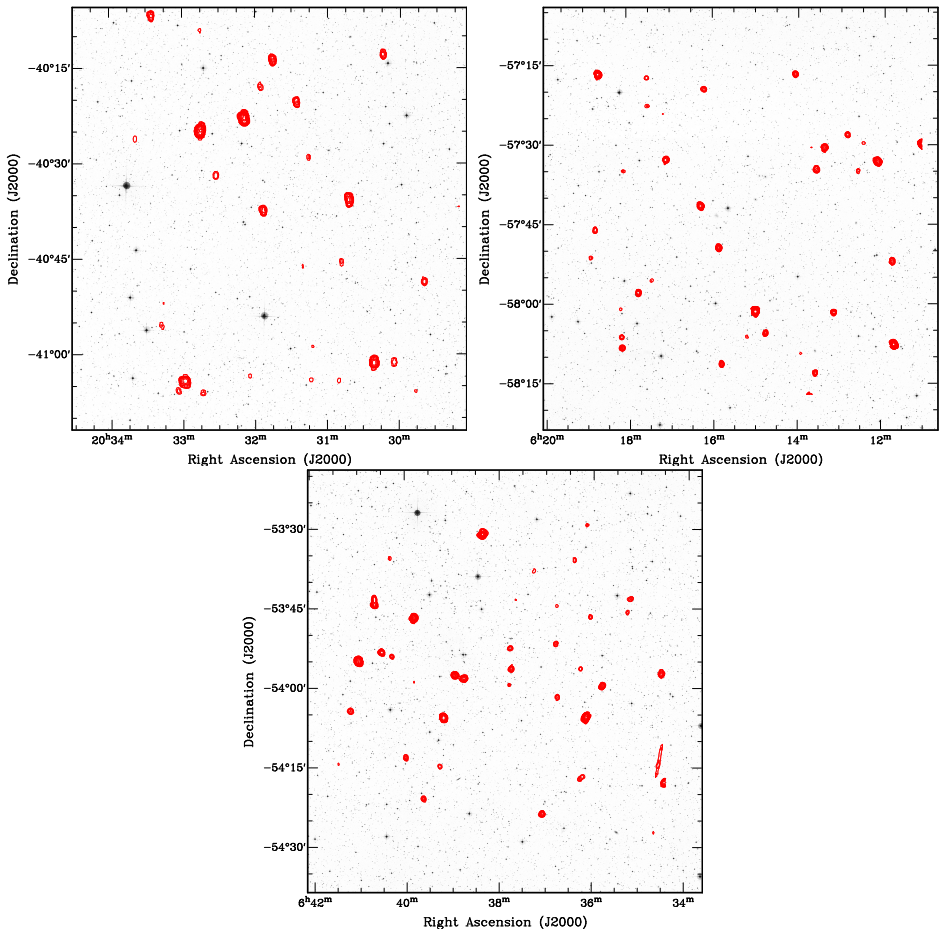

Figure A.4: DSS optical images of SPT-CL J2031-4037 (top left), SPT-CL J0615-5746 (top right), SPT-CL J0638-5358 (bottom centre) overlaid with red contours of SUMMS at 843 MHz

cluster centre.

From the above analysis of images, following galaxy clusters were shortlisted for further investigation

RXC J0605-3518

SPT-CL J0658-5556

SPT-CL J2023-5535

§A.3. RXC J0605-3518

This section discusses the data reduction results for the cluster RXC J0605-3518. The datasets for RXC J0605-3518 was downloaded from Australia Telescope Online

Table A.1: Dataset downloaded from ATOA for data reduction of RXC J0605-3518

Date	Scan time (mins)	Array	Bandwidth (MHz)	Frequency (MHz)	Project ID
1995-Jan-05	142.2	6A	128	1344	C416
1995-Jan-05	142.2	6A	128	2378	C416

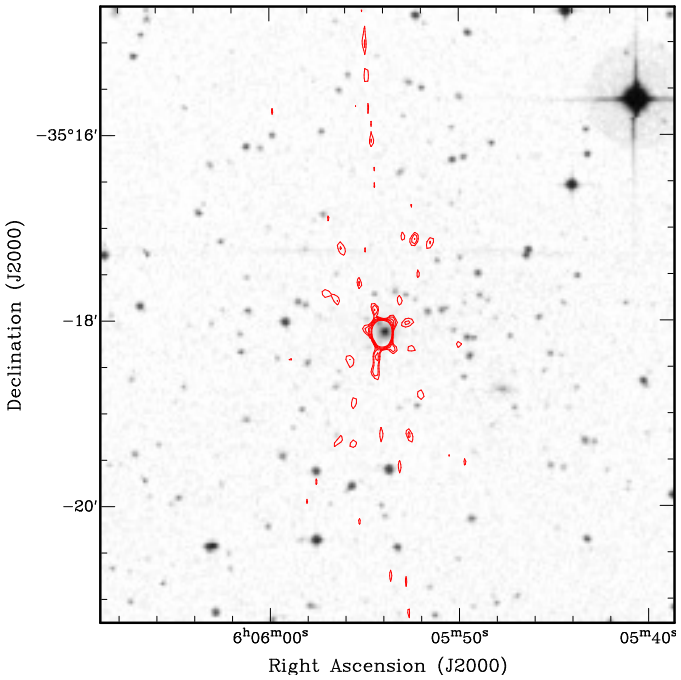

Figure A.5: DSS optical image of 0605-3518 overlaid with red contours of ATCA at 1.4 GHz. Beam size is 8.654 arcsec × 6.022 arcsec, pa = 1.595 degrees

Archive (ATOA) (Table A.1).

The primary source used for amplitude calibration was 1934-638 and secondary source used for phase calibration was 0614-349. The calibration of primary and secondary sources was performed in MIRIAD using MFCAL and GPCAL tasks. RFI flagging of Stokes U,V,Q,I for the primary and secondary were done using the BLFLAG and PGFLAG tasks. The GPBOOT and GPCOPY tasks were used to copy the calibration into the target dataset. Task INVERT was used to generate Stokes I dirty map and dirty beam using Imsize - 1024 × 1024 pixels and cell size 2 arcsec × 2 arcsec. The final image was generated using the standard PreCABB data reduction process discussed in Chapter 2 (see Fig A.5).

Figure A.5 indicates that the radio emission was from a point source and not a diffuse emission and hence does not indicate the existence of a halo or a relic in this cluster. Since low frequency investigation did not give enough proof for diffuse

Table A.2: Dataset downloaded from ATOA for data reduction of SPT-CL J2023-5535

Date	Scan time (mins)	Array	Bandwidth (MHz)	Frequency (MHz)	Project ID
2009-Oct-03	50.2	H75	2048	5500	C1563

emission, higher frequency analysis was not performed as sensitivity reduces with increase in frequency. Therefore the remaining high frequency datasets were ignored for further data reduction.

§A.4. SPT-CL J2023-5535

Datasets from ATOA were downloaded to analyse the SPT-CL J2023-5535 cluster. Table A.2 lists the datasets used for imaging the cluster to probe for diffuse emission.

The primary source used for amplitude calibration was 1934-638 and secondary source used for phase calibration was 2117-61. The calibration of primary and secondary sources was performed in MIRIAD using MFCAL and GPCAL tasks. RFI flagging of Stokes U,V,Q,I for primary and secondary was done using BLFLAG and PGFLAG tasks. GPBOOT and GPCOPY tasks were used to copy the calibration into the target dataset. INVERT task was used to generate dirty map and dirty beam. Since the dataset used was CABB, the bandwidth of the dataset is 2048 MHz. As a result, CABB data reduction needed additional steps of averaging the *uv* dataset and splitting the dataset into sub-bands of 4.732 GHz, 5.244 GHz, 5.756 GHz and 6.268 GHz. Averaging of *uv* dataset was done using UVAVER task in MIRIAD and splitting of datasets by sub-bands was done using UVSPLIT task in MIRIAD with MAXWIDTH option of 512 MHz. The final image was generated by following the standard data reduction process for CABB with the imsize 2048 $\times$ 2048 and cell size 5 arcsec $\times$ 5 arcsec (see Fig A.6).

The figure A.6 suggests the possibility of radio diffuse emission since the contours provide some evidence of extended diffuse emission like structure in the cluster. But there are some potential optical objects that could explain this emission and hence the image does not provide conclusive evidence for diffuse emission. This requires more analysis with new datasets and hence it was handed over for further investigation to a different team member.

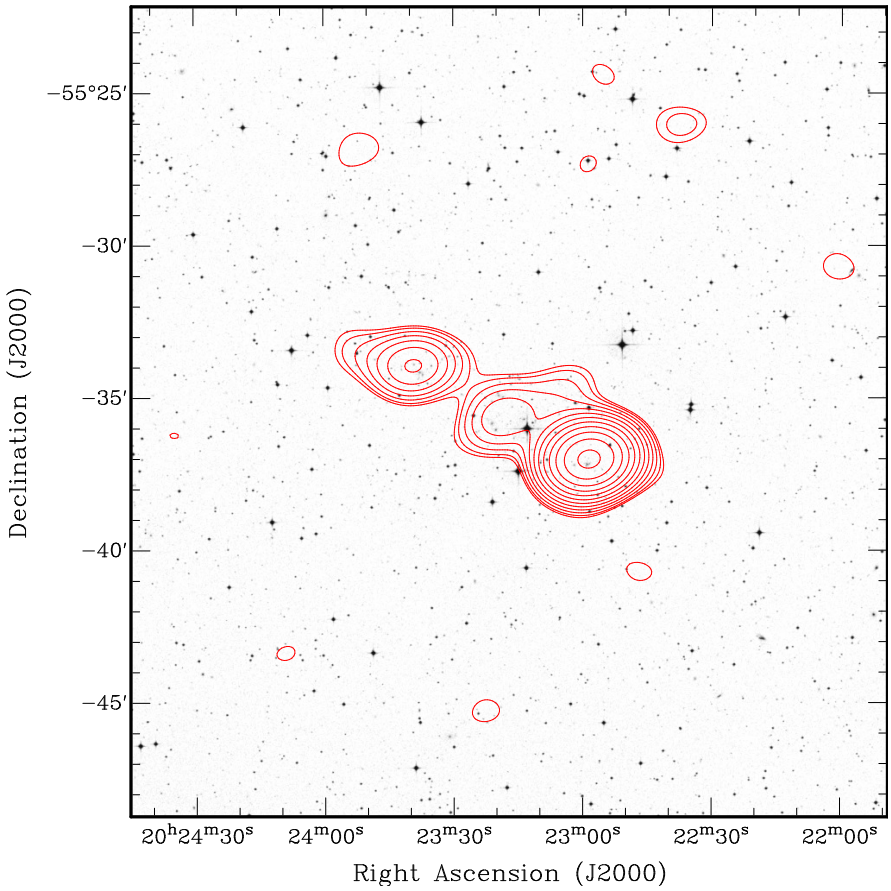

Figure A.6: DSS optical image of 2023-5535 overlaid with red contours of ATCA at 4.732 GHz. Beam size is 123.8 arcsec × 98.38 arcsec, pa = -79.48